

Functional characterization of the retinogeniculate pathway

Dissertation

zur Erlangung des Grades eines
Doktors der Naturwissenschaften

der Mathematisch-Naturwissenschaftlichen Fakultät
und
der medizinischen Fakultät
der Eberhard-Karls-Universität Tübingen

vorgelegt
von

Miroslav Román Rosón
aus Frýdlant, Tschechische Republik

Dezember 2017

Tag der mündlichen Prüfung: 19.06.2018

Dekan der Math.-Nat. Fakultät:

Prof. Dr. W. Rosenstiel

Dekan der Medizinischen Fakultät:

Prof. Dr. I. B. Autenrieth

1. Berichterstatter:

Prof. Dr. Laura Busse

2. Berichterstatter:

Prof. Dr. Thomas Euler

Prüfungskommission:

Prof. Dr. Laura Busse

Prof. Dr. Thomas Euler

PD. Dr. Philipp Berens

Prof. Dr. Cornelius Schwarz

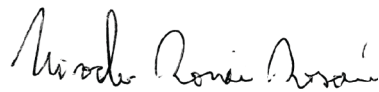
Erklärung / Declaration:

Ich erkläre, dass ich die zur Promotion eingereichte Arbeit mit dem Titel: "*Functional characterization of the retinogeniculate pathway*" selbständig verfasst, nur die angegebenen Quellen und Hilfsmittel benutzt und wörtlich oder inhaltlich übernommene Stellen als solche gekennzeichnet habe. Ich versichere an Eides statt, dass diese Angaben wahr sind und dass ich nichts verschwiegen habe. Mir ist bekannt, dass die falsche Abgabe einer Versicherung an Eides statt mit Freiheitsstrafe bis zu drei Jahren oder mit Geldstrafe bestraft wird.

I hereby declare that I have produced the work entitled "Functional characterization of the retinogeniculate pathway", submitted for the award of a doctorate, on my own (without external help), have used only the sources and aids indicated and have marked passages included from other works, whether verbatim or in content, as such. I swear upon oath that these statements are true and that I have not concealed anything. I am aware that making a false declaration under oath is punishable by a term of imprisonment of up to three years or by a fine.

Rülzheim, den 04.07.2018

Datum / Date



.....
Unterschrift /Signature

Table of Contents

1 Abstract	1
2 Introduction	3
2.1 The functional role of a visual system	3
2.2 The retinal circuitry	5
2.2.1 Signal transduction in the retina	5
2.2.2 Building blocks of the excitatory pathway	6
2.3 The retinogeniculate pathway	11
2.3.1 The classical model systems	11
2.3.2 Anatomical connectivity in the mouse model system	12
2.4 Organization of the mouse dLGN	13
2.4.1 Eye-specific segregation of RGC axons in dLGN	13
2.4.2 Cell-type-specific segregation of RGC axons in dLGN	13
2.4.3 Neuronal cell types of dLGN	14
2.4.4 Functional properties of dLGN neurons	15
2.5 Implications for dedicated visual circuits in dLGN	17
2.6 The purpose of this study	19
3 Materials & Methods	21
3.1 Functional characterization of dLGN-projecting RGCs	21
3.1.1 Animals and virus injection	21
3.1.2 Perfusion and retinal tissue preparation	22
3.1.3 Histological reconstruction of injection sites	22
3.1.4 Two-photon Ca ²⁺ imaging and light stimulation	22
3.1.5 Data analysis	23
3.1.6 Pre-processing	24
3.1.7 Receptive field mapping	24
3.1.8 Direction and orientation selectivity	25
3.1.9 Other response measures	26
3.1.10 Signal deconvolution	27
3.1.11 Assigning dLGN-projecting RGCs to previously characterized RGC types	27
3.1.12 Statistical significance of RGC clusters	29
3.1.13 Linear feed-forward model	29
3.2 Functional characterization of dLGN responses	31
3.2.1 Animals and surgical procedures	31
3.2.2 In-vivo multisite extracellular recordings	31
3.2.3 Visual Stimulation	32

3.2.4	Data analysis	33
3.2.5	Unit extraction and spike sorting	33
3.2.6	Receptive field mapping	33
3.2.7	Contrast response function	34
3.2.8	Tuning	34
3.2.9	Other response measurements	35
3.2.10	Non-negative matrix factorization	35
3.2.11	Correlating dLGN response components with RGC clusters	36
3.2.12	Dendrogram	36
3.2.13	Locomotion and speed Tuning	36
3.2.14	Histological reconstruction of recording sites	37
4	Results	39
4.1	Functional characterization of dLGN-projecting RGCs via retrograde viral tracing	39
4.2	dLGN-p RGCs represent the majority of functional RGC groups	43
4.3	dLGN neurons encode diverse visual features	51
4.4	Decomposing dLGN responses into diverse functional components	55
4.5	dLGN responses can be modelled as a sparse linear combination of inputs from RGC types	59
5	Discussion	63
5.1	Functional classification of dLGN-projecting RGCs	63
5.2	Components of the dLGN population response	66
5.3	Functional connectivity of dLGN projections	67
5.4	Towards the development of a functional model of visual processing	71
6	References	73
7	Acknowledgements	87
8	Appendix	88
8.1.1	Appendix 1	89
8.1.2	Appendix 2	90
8.1.3	Appendix 3	91
8.1.4	Appendix 4	92
8.1.5	Appendix 5	93

Publications, manuscripts and contributions

During my time as a PhD student I contributed to the 5 studies listed below. Three have already been published, while one is available as a preprint at bioRxiv and the last one is to be submitted soon. Four out of six studies are covered by the present work, with a focus on Roman Roson et al., which represents the main part of my PhD work. The contributions to each publication are listed below in detail and summarized in section 8 (Appendix).

Published

Appendix 1

Tom Baden*, Philipp Berens*, Katrin Franke*, Miroslav Román Rosón, Matthias Bethge & Thomas Euler (2016). The functional diversity of retinal ganglion cells in the mouse. *Nature*, 529(7586), 345–350. <https://doi.org/10.1038/nature16468>

Contributions

In this study, we used two-photon calcium imaging to obtain dense retinal recordings and unsupervised clustering of more than 11,000 cells to determine how many parallel output channels, the retinal ganglion cells (RGCs), exist in the mouse retina and what type of information they encode. The results were supplemented by genetic and immunohistochemical labels, as well as electrical measurements to extend the domain knowledge of each RGC type. In a fraction of cells, the morphology the respected cell was reconstructed in order to link the functional RGC types to anatomically defined types.

In this study, I established electrical single-cell recordings of RGC spikes triggered by light stimuli and filling of RGCs for morphological reconstruction. Further, I performed pre-processing and reconstructed the morphologies of recorded cells with anatomical data. The results of this study, were used as a basis for my PhD project and thus for the manuscript Roman Roson et al. (Appendix 5).

Appendix 2

Aman B. Saleem,* Anthony D. Lien, Michael Krumin, Bilal Haider, Miroslav Román Rosón, Asli Ayaz, Kimberly Reinhold, Laura Busse, Matteo Carandini,* and Kenneth D. Harris*, (2017). Subcortical Source and Modulation of the Narrowband Gamma Oscillation in Mouse Visual Cortex. *Neuron*, 93(2), 315–322. <https://doi.org/10.1016/j.neuron.2016.12.028>

Contributions

In this study we characterized the narrowband gamma oscillations in awake mouse primary visual cortex and explored its synaptic basis and its dependence on visual contrast and

locomotion. Furthermore, we used optogenetics for silencing the cortex, and extracellular recordings from dorsolateral geniculate nucleus (dLGN) to investigate the source of these narrowband gamma oscillations.

I performed the in-vivo extracellular multi-electrode recordings in the dLGN of awake, head-fixed mice. Further, I provided input for the manuscript. The results of this study are not part of this thesis, and thus will not be further discussed.

Appendix 3

Lucas Theis, Philipp Berens*, Emmanouil Froudarakis, Jacob Reimer, Miroslav Román Rosón, Tom Baden, Thomas Euler, Andreas S. Tolias, and Matthias Bethge* (2016). Benchmarking Spike Rate Inference in Population Calcium Imaging. *Neuron*, 90(3), 471–482. <https://doi.org/10.1016/j.neuron.2016.04.014>

Contributions (together with Berens et al., Appendix 4)

Recently, I contributed to two studies, which provided valuable insights regarding this issue: Berens et al., (2017) and Theis et al., (2016) systematically evaluated a range of spike inference algorithms. In addition, Theis et al., (2016) introduced a new data-driven approach based on supervised learning in flexible probabilistic models to infer spikes from Ca^{2+} fluorescence traces, and showed that this new method outperformed all previously published techniques.

In the study Roman Roson et al., we used two-photon Ca^{2+} imaging to measure activity from dLGN-p RGCs and performed extracellular recordings to measure spikes from dLGN neurons. A direct comparison of these two datasets is a non-trivial task, which requires a conversion of the two datasets to the same “currency”, i.e. spikes have to be converted to Ca^{2+} signal or Ca^{2+} signal has to be converted to spikes. This can be achieved by several strategies, using (de-) convolution or spike inference from the Ca^{2+} data.

To both studies (Berens et al.; Theis et al., 2016), I provided simultaneously recorded data using two-photon Ca^{2+} imaging and extracellular electrophysiological recordings from retinal ganglion cells.

Manuscripts

Appendix 4

Philipp Berens, Jeremy Freeman, Thomas Deneux, Nicolay Chenkov, Thomas McColgan, Artur Speiser, Jakob H. Macke, Srinivas C. Turaga, Patrick Mineault, Peter Rupprecht, Stephan Gerhard, Rainer W. Friedrich, Johannes Friedrich, Liam Paninski, Marius Pachitariu, Kenneth D. Harris, Ben Bolte, Timothy A. Machado, Dario Ringach, Jasmine Stone, Nicolas J. Sofroniew, Jacob Reimer, Emmanouilis Froudarakis, Thomas Euler,

Miroslav Román Rosón, Lucas Theis, Andreas S. Tolias, & Matthias Bethge. (2017). Community-based benchmarking improves spike inference from two-photon calcium imaging data. 171818192017223(16). <https://doi.org/10.1101/177956>. This article is available as preprint; it is currently under revision at PLoS Comp Biol.

Appendix 5

Miroslav Román Rosón, Yannik Bauer, Philipp Berens, Thomas Euler and Laura Busse. Sparse linear recombination using most retinal output channels yields highly diverse visual representations in mouse dLGN

Contributions:

In this study, we functionally characterized the population of dLGN-projecting RGCs and geniculate neurons, and linked the results via computational modelling to provide a quantitative account of the transformations in visual representation between RGCs and dLGN neurons.

This study represents the main part of my PhD thesis. For this purpose I performed following experimental procedures and methods:

Performed surgical procedures

- Performed multisite extracellular recordings from dorsolateral geniculate nucleus (dLGN)
- Established the viral approach and performed two-photon Ca^{2+} imaging of dLGN-projecting (dLGN-p) retinal ganglion cells (RGCs).
- Performed pre-processing of both datasets.
- Performed the dLGN analysis
- Established the linear feed-forward model
- Wrote the original draft of the manuscript

1 Abstract

More than 30 functional types of retinal ganglion cells (RGCs) compute in parallel distinct features of the visual world and send this information to the brain. Little is known, however, about which RGC types project to the dorsolateral geniculate nucleus (dLGN) of the thalamus, and how the different RGC channels recombine there. Interest in these questions has been fuelled by recent estimates of retinogeniculate convergence obtained by anatomical work, which far exceeded those obtained in electrophysiological recordings.

To get insights into the nature of retinal input to the dLGN, we conditionally expressed the genetically encoded Ca^{2+} indicator GCaMP6f in dLGN-projecting (dLGN-p) RGCs, followed by *in vitro* retinal two-photon Ca^{2+} imaging of light-evoked responses. Visual stimuli matched those in a previously published survey of mouse functional RGC types (Baden et al., 2016). We then assigned each dLGN-p RGC to the best-matching RGC type with the best-matching response properties. We found that most functional RGC types seem to innervate dLGN, with certain types, such as ON- and OFF alpha cells or OFF suppressed cells, showing clear overrepresentations.

In a separate set of experiments, we characterized the responses of dLGN neurons to the same visual stimuli using *in-vivo* extracellular multi-electrode recordings in the dLGN of awake, head-fixed mice. We quantitatively assessed the degree of diversity in the dLGN responses by using sparse non-negative matrix factorization (NNMF), which decomposed the dLGN population response into a rich and highly diverse set of components.

Finally, we linked the functionally characterized population of dLGN-projecting RGCs and geniculate neurons, via computational modelling to provide a quantitative account of the transformations in visual representation between RGCs and dLGN neurons. We found that responses of dLGN neurons could be best predicted as a sparse linear combination of responses from 3-7 different RGC types.

In conclusion, this study provides fundamental insights into how the representation of visual information changes along the first stages of the retino-geniculo-cortical pathway, suggesting that the precortical basis of vision displays an unexpectedly rich functional diversity of retino-geniculate projections and thalamic features that can be modelled by a sparse feed-forward model.

2 Introduction

2.1 The functional role of a visual system

Vision is the most fundamental of our senses and plays a crucial role in the survival of many animals. The visual system extracts and interprets relevant features from the environment to build an internal representation of the outside world. For example, an eagle has the ability to recognize small animals, like mice, in their natural environment and distinguish them from their surroundings from far above in the sky. This is only possible, because the eagle's visual system features a high spatial resolution and the ability to interpret small objects as its prey. In contrast, a mouse does not need high resolution to identify the eagle as its predator, but instead its visual system appears to provide mechanisms for detecting fast, approaching objects from above (Münch et al., 2009).

The only visual input available to the brain is provided by the eyes. There, the information from our surroundings is projected through the optics of the eyeball onto a light-sensitive neural tissue, called the retina (Masland, 2012). The machinery of the retina decomposes visual information into multiple parallel processing channels, thereby providing a compact and efficient input to higher visual centres. Understanding how visual information is encoded by the outputs of these channels will thus provide a complete representation of visual information available to the brain. (Fig. 1) (Azeredo da Silveira & Roska, 2011; Euler et al., 2014; Huberman & Niell, 2011).

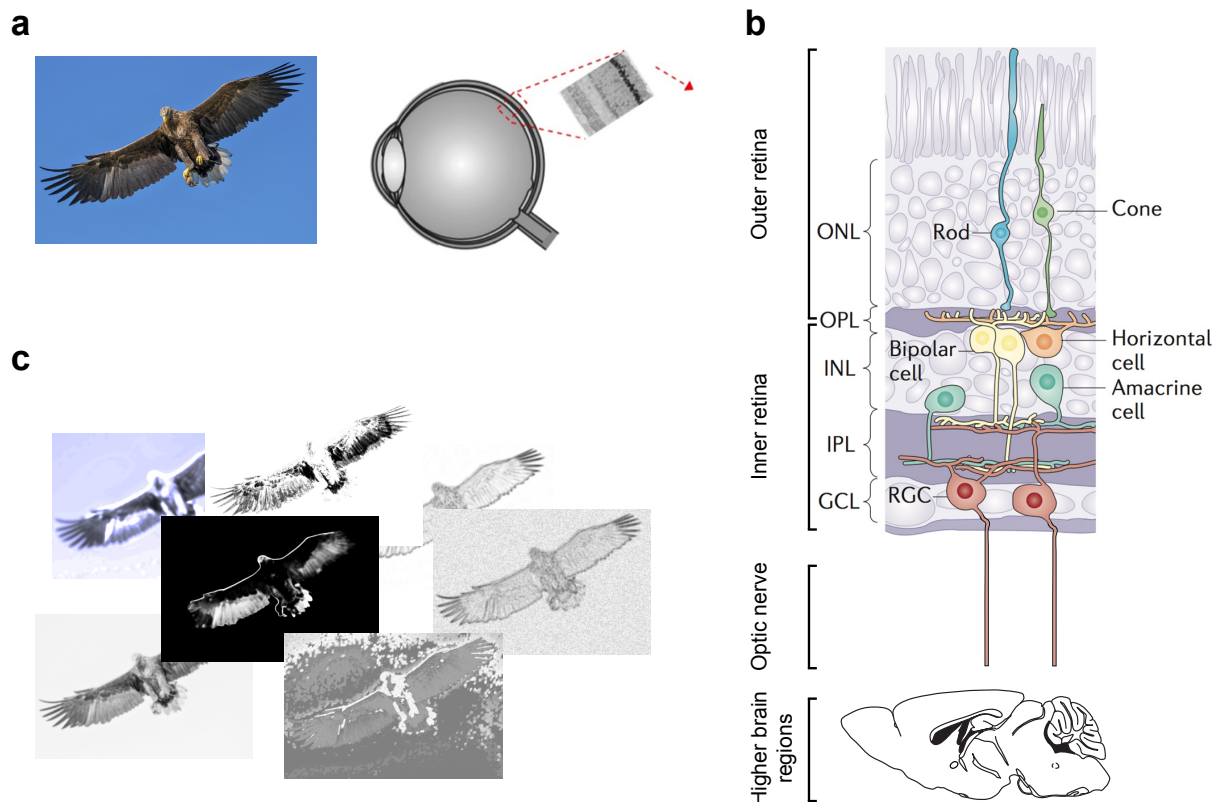


Figure 1 | Retina as a model system for parallel processing of sensory information. **a.** An inverted image of the outside world is projected onto a light-sensitive neural tissue, the retina, located in the back of the eyeball. **b.** The retina is a layered structure consisting of five neural cell types. The rod and cone photoreceptors transduce light into electrical signals and distribute these at the first synaptic layer, the outer plexiform layer (OPL) onto the dendrites of ≥ 14 types of bipolar cell. Bipolar cells decompose the photoreceptor signal into multiple parallel information channels and relay it into the inner plexiform layer (IPL), where the bipolar cell axon terminals synapse onto amacrine cells and retinal ganglion cells (RGCs). RGCs are the output neurons of the retina. They encode different aspects of visual information in parallel and relay it as spike trains through the optic nerve to higher visual areas in the brain. Along this excitatory feed-forward pathway, the visual signal is modulated by inhibitory interneurons, the horizontal and amacrine cells, in OPL and IPL, respectively. **c.** The retina extracts different visual features, such as luminance, contrast, edges, motion, or chromatic information from the light pattern projected into the eye. These specific features are encoded by RGCs and send to the brain in parallel. Abbreviations: ONL, outer nuclear layer; INL, inner nuclear layer; GCL, ganglion cell layer. The photo was taken from free image gallery pixabay: <https://pixabay.com/en/eagle-bird-bird-of-prey-expensive-1753002/>; Panel (b) modified with permission from Euler et al., (2014).

2.2 The retinal circuitry

The mammalian retina is a highly sophisticated light-sensitive neural network that transforms visual information into a rich array of electrical signals. This process is performed by five cardinal cell classes, which are organized in a layered structure, with each layer containing either cell bodies (nuclear layers) or synaptic neuropil (plexiform layers) (reviewed in Wässle, 2004). Photoreceptors, bipolar cells (BCs) and retinal ganglion cells (RGCs) are glutamatergic neurons and form the excitatory pathway of the retina. Horizontal cells and amacrine cells (ACs) belong to the group of (mostly) inhibitory interneurons. They extensively modulate the excitatory pathway and thus shape visual information mainly by lateral inhibition in the outer and inner retina, respectively (Fig. 1b).

2.2.1 Signal transduction in the retina

In the outer retina, photoreceptors - rods and cones - absorb photons in their outer segments, and by using opsin transduction cascades (reviewed in Korenbrot, 2012), they transform the spatio-temporal light pattern projected on the retina into graded electrical signals that provide the basis for downstream visual processing. Photoreceptors continuously release glutamate as their neurotransmitter in the dark, thereby exciting bipolar cells that express ionotropic glutamate receptors (so-called OFF bipolar cells). Upon light stimulation, photoreceptors reduce their glutamate release, which leads to the excitation of bipolar cells expressing metabotropic, sign-inverting glutamate receptors (so-called ON bipolar cells) (reviewed in Demb & Singer, 2015). Glutamate released by photoreceptors is further modulated via feedback and feed-forward inhibition from horizontal cells, for example, to adjust the photoreceptor's output gain depending on the illumination level (Xin & Bloomfield, 1999). Already at the level of the BCs, the photoreceptor input is distributed into multiple parallel channels, which transmit the signal from the outer to the inner retina (Euler et al., 2014; Franke et al., 2017; Wässle, 2004). In the inner plexiform layer (IPL), bipolar cells relay visual information onto a complex network of RGC and amacrine cell dendrites. Similar to horizontal cells, amacrine cells modulate the response of bipolar cells at the level of their synaptic terminals (Eggers & Lukasiewicz, 2010; Zhang et al., 1997), and ganglion cells via lateral inhibition, thereby adjusting diverse spatio-temporal properties of the visual signal (Eggers & Lukasiewicz, 2011). There are approximately 30-40 different types of amacrine cells in the retina, which vary widely in morphology and function (MacNeil & Masland, 1998; Strettoi & Masland, 1996). Most of the amacrine cells are inhibitory and release GABA or glycine as their neurotransmitter. However, many amacrine cell types co-release neuromodulators such as acetylcholine or dopamine (Demb & Singer, 2015).

Ganglion cells are the only output neurons of the retina. They encode diverse visual features (Baden et al., 2016; Gollisch & Meister, 2010) and transmit the information through the optic nerve to more than 50 retino-recipient areas in the brain (Martersteck et al., 2017).

2.2.2 Building blocks of the excitatory pathway

Photoreceptors

Photoreceptors can be divided into two sub-classes. Rods are highly sensitive to light and operate under low-light levels (scotopic conditions), whereas cones absorb photons only at brighter light levels (photopic conditions), when rod photoreceptors are thought to be already saturated. Under mesopic light conditions, both sub-classes of photoreceptors contribute to vision (reviewed in Purves et al., 2001). In the following, the focus will be on the cone pathways in the retina.

Cone photoreceptors can be divided into different types based on their spectral sensitivity, thereby providing the basis for parallel chromatic pathways in the retina. The spectral sensitivity of cone photoreceptors varies across species and is adapted to their respective environment (Peichl, 2005). For instance, humans and old-world primates have three cone types expressing specific opsins with sensitivities in the short (S, “blue”), medium (M, “green”), and long (L, “red”) wavelength range with maximal absorptions at approximately 425 nm, 530 nm, and 560 nm, respectively (Riggs, 1967). In comparison, most non-primate mammals contain two cone types: S- and M-cones. Mice express S- and M-opsins with their maximal absorption at approximately 360 nm and 510 nm, respectively (Haverkamp, 2005).

In addition to different spectral sensitivities, different types of cone photoreceptors were shown to have distinct functional properties. The distribution of chromatic and achromatic features differs in natural scenes above and below the horizon. Therefore, it was proposed that in the mouse, the asymmetric retinal arrangement of S- and M-cones (Röhlich et al., 1994; Szél et al., 1992) is used to sample light in the sky and on the ground differentially. This idea was tested by Baden et al., (2013), who showed that in the mouse functional S-cones mainly encode the visual scenes above the horizon and prefer dark over bright stimuli, which is in agreement with the predominance of dark contrasts in the sky, but not on the ground. In contrast, functional M-cones encode both bright and dark stimuli similarly well and encode the visual scenes mainly below the horizon.

Bipolar cells

Bipolar cells form the first stage of parallel processing channels in the retina. They integrate

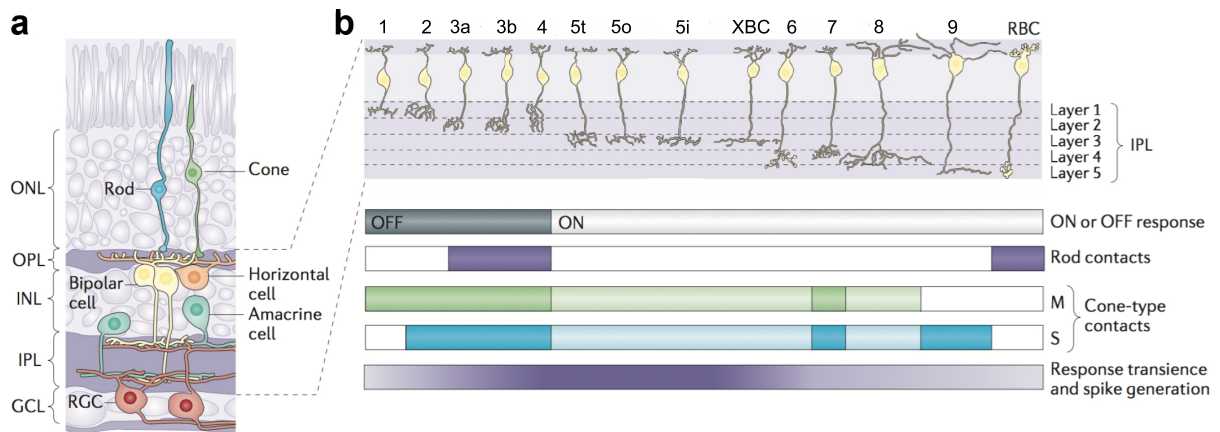


Figure 2 | Bipolar cell types of the mouse retina. **a.** Same as in Fig. 1b. **b.** Top: The mouse retina contains 14 anatomically defined types of bipolar cell, which can be distinguished based on shape and stratification depth of their axon terminals. Bottom: Different bipolar cell types can be separated into ON vs. OFF and transient vs. sustained types, according to their light responses, which vary depending on the stratification level. Moreover, some bipolar cell types can be further differentiated on the basis of their input from rod or cone photoreceptors, or from short or medium wavelength-sensitive cone photoreceptors. Figure modified with permission from Euler et al., (2014).

visual information across multiple photoreceptor inputs along their dendrites and relay the signal to the IPL, where most of the computations underlying the extraction of visual features take place (Fig. 2) (Euler et al., 2014).

In the mouse, a set of 14 types of bipolar cell has recently been anatomically described by serial-sectioning electron microscopy (Fig. 2b, top) (Greene et al., 2016; Helmstaedter et al., 2013; Kim et al., 2014). Different types of bipolar cell can be identified based on the shape and IPL stratification level of their axon terminals (Euler et al., 2014). In mammals, the IPL is traditionally subdivided into five strata of equal thickness (Kolb, 1979); these strata can be grouped into an OFF and an ON sublamina, comprised of IPL strata 1-2 and 3-5, respectively. Following this division, bipolar cells responding to light decrements (OFF BCs) stratify in the OFF part of the IPL, whereas bipolar cells depolarizing to light increments (ON BCs) stratify in the ON part of the IPL (Euler et al., 1996). In addition, the stratification level of the bipolar cells reflects their temporal properties, with sustained bipolar cells typically stratifying at the borders of the IPL, and transient and spiking bipolar cells ramifying closer to its centre (Fig. 2b) (Awatramani, 2000; Roska & Werblin, 2001).

Furthermore, bipolar cells can be differentiated on the basis of their input. The classical view is that 13 out of the 14 types of bipolar cell receive their glutamatergic input mainly from

cone photoreceptors, whereas a single type of rod bipolar cell samples rod inputs (Euler et al., 2014). Recently, it has been shown that different bipolar cell types can also receive mixed input, as several cone bipolar cell types form additional connections to rods (Fyk-Kolodziej et al., 2003; Hack et al., 1999) and rod bipolar cells receive input from both rod and cone photoreceptors (Behrens et al., 2016; Pang et al., 2010). Furthermore, some bipolar cell types receive selective input from short or medium wavelength-sensitive cones, thereby providing the basis for spectrally distinct channels (Puller & Haverkamp, 2011).

Different bipolar cell types split the photoreceptor signal into separate parallel channels and relay this information to the IPL, where excitatory and inhibitory inputs, originating from bipolar and amacrine cells, respectively, converge onto RGC dendrites. By integrating multiple excitatory and inhibitory inputs, RGCs inherit a highly specific combination of functional properties (Sanes & Masland, 2015). Some of the functional RGC properties, such as polarity, transience or chromaticity can be predicted by their stratification level in the IPL, since they receive their excitatory glutamatergic input from different bipolar cell types, whose axon terminals ramify in different strata of the IPL (Awatramani, 2000; Breuninger et al., 2011; Franke et al., 2017).

Retinal ganglion cells

Retinal ganglion cells are the output neurons of the retina and represent parallel feature channels that provide the only available source of visual information to the brain (reviewed in Sanes & Masland, 2015). These feature channels are formed by different bipolar and ganglion cell types, where each type of ganglion cell is believed to exhibit a unique physiological function. Understanding the retinal signal processing thus requires the knowledge of how different RGCs types encode visual information (Fig 3).

The modern anatomical taxonomy of RGC dendritic morphologies was established in early studies using Golgi, Nissl, and neurofibrillar stains (Stone, 1984), and was based on different morphometric parameters, including dendritic morphology, size of the cell body and the dendritic tree, and the stratification depth of the axon terminals in the IPL. The classification of RGCs advanced rapidly with the introduction of methods for intracellular dye filling, initially achieved through sharp electrodes in fixed or living tissue (e.g. Buhl & Peichl, 1986; Pu & Amthor, 1990). The breakthrough came with the arrival of modern molecular techniques using large-scale chemical mutagenesis or targeted genetic manipulation (McGavern & Kang, 2011; Salinas et al., 2010), in particular, transgenic mouse strains, in which marker proteins are expressed under the control of cell-type-specific promoters, have been used

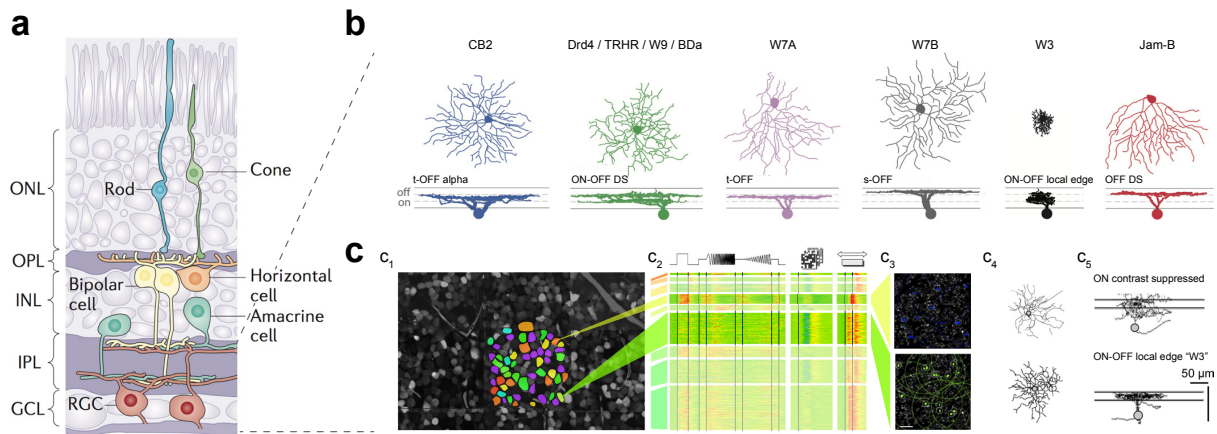


Figure 3 | Anatomical and functional classification of mouse retinal ganglion cell types. **a.** Same as in Fig. 1b. **b.** Representative morphologies and IPL stratification depths of genetically labelled ganglion cells in the retinas of transgenic mouse lines. The respective transgenic mouse line is listed above each cell type. **c.** Functional classification of RGC types by Baden et al., (2016). (c_1) Whole-mount view of a Ca^{2+} indicator-stained mouse retina, with different functional cell types colour-coded in the central patch. (c_2) RGC responses to different visual stimuli sorted by functional RGC clusters from exemplary cells in (c_1); warm colours indicate an increase, cold colours a decrease in activity; block height represents number of cells in the respective cluster. (c_3) Distribution (c_3) and morphology with a top (c_4) and a side (c_5) view of the two example RGCs highlighted in (c_2). Abbreviations: DS, direction-selective; t-OFF, OFF-transient; s-OFF, OFF-sustained. Scale bars: c, 50 μ m. Panel (a) modified with permission from Euler et al., (2014). Panel (b) modified from Dhande et al., (2015). Panel (c) modified from Baden et al., (2016) and <http://www.eye-tuebingen.de/eulerlab/projects/the-retinal-code/>.

with great success to systematically characterize retinal cell types (Fig. 3b) (reviewed in Dhande et al., 2015).

The first physiological classifications of RGCs were based on single cells studies, with recordings made in-vivo either intraocularly directly from their cell bodies (Barlow et al., 1964) or intra-cranially from their axons in the optic tract (Enroth-Cugell & Robson, 1966). These early studies functionally grouped the RGCs into broad categories, based on their cardinal response properties (ON vs. OFF, transient vs. sustained) (Dowling & Werblin, 1969; Lettvin et al., 1959). With the development of optical and electrophysiological population recordings, such as Ca^{2+} imaging (Briggman & Euler, 2011) or microelectrode arrays (Farrow & Masland, 2011), functional classifications shifted from single-cell to population-based approaches, and greatly increased the rate at which in particular relatively rare RGC types were functionally classified (Amthor & Oyster, 1995). The most complete survey of RGCs in the mouse retina so far identified a minimum of 32 functional RGC types,

by combining the advantages of two-photon Ca^{2+} imaging and unsupervised clustering of more than 11,000 cells (Fig. 3c) (Baden et al., 2016).

2.3 The retinogeniculate pathway

The main central target areas for RGCs are the superior colliculus and the dorsal lateral geniculate nucleus (dLGN). Both structures receive highly correlated and retinotopically organized input from different RGC types (reviewed in Dhande et al., 2015). The dLGN as a part of the retino-geniculo-cortical pathway, represents the main station on the route for visual information to reach the primary visual cortex for visual perception (Huberman & Niell, 2011). While it has long been known that this pathway is not homogenous but consists of parallel channels each carrying specific information (e.g. Cruz-Martín et al., 2014), it is still debated which RGC types project to the dLGN and how their functional output is transformed at the level of the dLGN.

The retinal afferents provide the primary excitatory drive for the dLGN neurons and comprise about 10% of the total number of synapses in dLGN, with roughly 90% arising from a variety of other sources including visual cortex (V1), superior colliculus (SC) or the thalamic reticular nucleus (TRN) (Bickford et al., 2015; Guillery & Sherman, 2002). Studies using *in vitro* slice recordings to estimate retinal convergence have shown that during early postnatal age, dLGN neurons receive relatively weak synaptic input from several RGCs. During the first few weeks of postnatal life, they then undergo a substantial anatomical refinement followed by a sensory-dependent plasticity, where significant axon pruning occurs (Guido, 2008; Hong et al., 2014). Even though precise connectivity between RGCs and dLGN neurons is thought to be essential for the transmission of visual information, it is still not well understood, and the degree and nature of retinal convergence onto dLGN neurons has been a topic of intense investigations.

2.3.1 The classical model systems

Retino-geniculate information transmission has been studied extensively in cats and monkeys, where the vast majority of dLGN neurons seems to be driven by only few (1-3) dominant RGCs, thereby acting as relays for retinally defined visual channels (Cleland et al., 1971; Usrey et al., 1999). This dominant input can evoke such strong excitatory postsynaptic potentials (EPSPs) – so-called “S-potentials” (for synaptic) - that they can be picked up by extracellular recordings during single neuron activity in dLGN. Consistent with a low degree of convergence, a dLGN neuron’s “S-potentials” and its spiking output have closely matching receptive fields (RFs) in terms of location, center-surround organization and size (Hubel & Wiesel, 1961; Kaplan et al., 1987; Sincich et al., 2007). Next to the dominant inputs, electron microscopy (Hamos et al., 1987) and *in vivo* electrophysiological studies (Cleland et al.,

1971; Mastronarde, 1987, 1992; Usrey et al., 1999) have shown that cat dLGN cells can receive additional weaker input from multiple RGCs.

Besides the number of RGC inputs converging on single dLGN neurons, it has been another long-standing question whether converging RGC inputs to dLGN neurons arise from the same RGC type. In the cat, probability of monosynaptic connections between individual RGCs and dLGN neurons, as well as their strength have been found to increase with RF similarity (Usrey et al., 1999), but connectivity between dissimilar retinal and geniculate RFs has been observed as well (Usrey et al., 1999). In cats and monkeys, the increase in connection probability between RGCs and dLGN neurons with similar RFs might not be surprising, given the pronounced stream specificity and strict spatial layering of LGN relay cells. Hence, despite the fact that in monkeys, a heterogeneous set of at least 13 types of dLGN-projecting RGC has been identified (Dacey et al., 2003), this highly organized functional mapping at the level of dLGN makes opportunities for mixing of inputs from several RGC types, at least within the classical pathways, rare (Chen et al., 2016; Nassi & Callaway, 2009; Sur et al., 1987).

2.3.2 Anatomical connectivity in the mouse model system

Recent anatomical studies in the mouse started to challenge the retino-geniculate connectivity, where a detailed and complex picture emerges. Rabies virus tracing of monosynaptic inputs received by individual neurons in dLGN has revealed that mouse dLGN neurons can be divided in two groups based on the pattern of their retinal inputs (Rompani et al., 2017): while some dLGN cells received inputs from mostly a single RGC type (“relay input mode”), others showed a high degree of convergence, with inputs being composed of up to 91 RGCs of different types (“combination input mode”). A high degree of retinogeniculate convergence and mixing of inputs is further supported by recent ultrastructural studies of retinal afferents and their thalamic relay cell targets (Hammer et al., 2015; Morgan et al., 2016).

2.4 Organization of the mouse dLGN

The mouse dLGN is located in the dorsal-lateral part of the thalamus (reviewed in Kerschensteiner & Guido, 2017; Litvina & Chen, 2017a; Monavarfeshani et al., 2017). In contrast to the iconic six-layered primate dLGN, mouse dLGN lacks the overall cytoarchitectural lamination (Reese, 1988). Instead, it can be organized based on (i) eye-specific and (ii) cell-type-specific segregation of RGC axons, and (iii) regional distribution of neuronal cell types.

2.4.1 Eye-specific segregation of RGC axons in dLGN

Anterograde tracing studies have revealed that the retinal projections from each eye are segregated into non-overlapping eye-specific domains within the mouse dLGN (Jaubert-Miazza et al., 2005; Muir-Robinson et al., 2002). In adult mice, axons from the contralateral eye extend across 85–90% of total dLGN area, whereas the input from the ipsilateral eye covers 10-12% of the dLGN (Guido, 2008). The small size of the ipsilateral domain and the comparatively large dendritic arbour of dLGN neurons suggest that visual information from both eyes is combined. Evidence for such binocular integration in the dLGN comes from a recent single-cell trans-synaptic tracing study, showing that a subset of dLGN neurons indeed receive converging input from both eyes (Rompani et al., 2017). However, it is still not clear to what extent and which stimulus conditions can drive the binocular responses (Howarth et al., 2014; Zhao et al., 2013b; Ziburkus & Guido, 2006).

2.4.2 Cell-type-specific segregation of RGC axons in dLGN

Morphological and functional classifications (Baden et al., 2016; Helmstaedter et al., 2013; Sanes & Masland, 2015; Sümbül et al., 2014), supported by an increasing number of transgenic mouse lines labelling individual RGC types (Huberman et al., 2008; Kay et al., 2011; Kim et al., 2010; Rivlin-Etzion et al., 2011), revealed a rich diversity among RGCs comprising more than 30 distinct cell types in the mouse retina. As confirmed by retrograde labelling (Ellis et al., 2016), dLGN receives input from a heterogeneous set of RGC types, indicating that a large number of parallel information channels feeds the dLGN. To what extent the incoming information remains separate, or how it can be combined by dLGN neurons depends in part on the cell-type-specific segregation of RGC axons in dLGN.

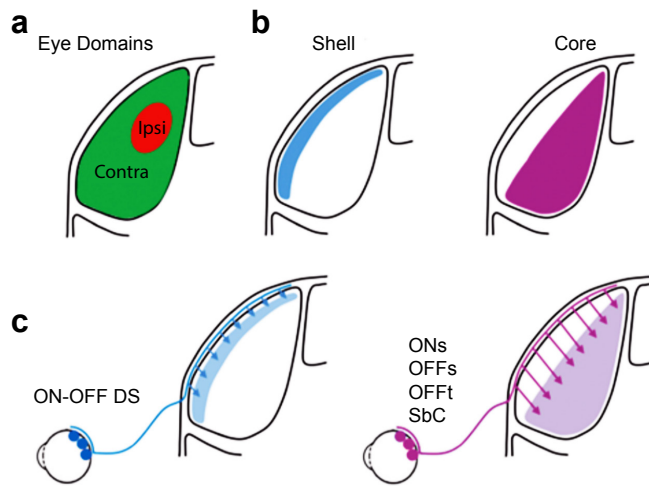


Figure 4 | Organization of the mouse dLGN.

a. Eye-specific segregation of RGC axon terminals from contralateral (green) or ipsilateral eye (red). **b.** Functional separation of the dLGN into shell and core. The shell receives convergent input from direction-selective (DS) RGCs and from the SC. The core is innervated, for instance, by alpha RGCs and melanopsin-expressing RGCs. **c.** Projection patterns of different functional RGC types. Abbreviations: ONs, ON-sustained; OFFs, OFF-sustained; OFFt, OFF-transient; SbC, suppressed-by-contrast. Figure adapted with permission from Kerschensteiner & Guido, (2017).

In the mouse, experiments with genetically labelled axons of functionally defined RGC types confirmed that the mouse dLGN contains at least two spatially distinct and retinotopically organized functional regions (Dhande et al., 2015; Huberman & Dhande, 2014; Martersteck et al., 2017). The superficial layers of the dLGN, also called the shell, are innervated by axons from various direction-selective RGCs, with each subtype tuned to one of the four cardinal directions (Huberman et al., 2009; Kay et al., 2011; Kim et al., 2008, 2010; Rivlin-Etzion et al., 2011). In contrast, neurons in the deeper layers of the dLGN, also called the core, are not directionally tuned and receive input, for instance, from alpha (Huberman et al., 2008) and melanopsin-expressing RGCs (ipRGCs) (Brown et al., 2010; Ecker et al., 2010). These results are also supported by physiological (Piscopo et al., 2013) and imaging studies (Marshel et al., 2012), confirming, that direction- and orientation-selective dLGN neurons are enriched in regions that match the termination zone of direction selective ganglion cells (DSRGC) from the retina.

2.4.3 Neuronal cell types of dLGN

Recent studies using single-cell intracellular fills performed during *in vitro* recordings to study the postsynaptic organization of dLGN neurons, demonstrated that the mouse dLGN contains at least four distinct neuronal cell types (Krahe et al., 2011; Seabrook et al., 2013). Morphologically, these neurons resemble the X (bi-conical), Y (symmetrical), and W (hemispheric) neurons described in the dLGN of a cat (Krahe et al., 2011; Sherman, 1985), as well as the local inhibitory neurons. Furthermore, each cell type exhibits strong regional preference within the dLGN (Krahe et al., 2011). X cells reside in the monocularly innervated

ventral part of dLGN. Y cells are more evenly dispersed and show a strong preference of the binocular region of dLGN. W cells are found predominantly in the shell, which receives retinal input from DSRGCs (Cruz-Martín et al., 2014). Finally, inhibitory interneurons are dispersed throughout the entire dLGN. Interestingly, the X and Y versus W type show a strong distribution bias for the core and the shell region of dLGN, respectively (Krahe et al., 2011).

2.4.4 Functional properties of dLGN neurons

In terms of physiology, mouse dLGN neurons have complex and diverse visual response properties. Similar to results in primates (De Monasterio & Gouras, 1975), the majority of mouse dLGN neurons exhibit circularly symmetric RFs and perform linear spatial summation (Denman & Contreras, 2016; Grubb, 2003). In addition, also contains neurons with more complex and diverse response properties: Orientation-selective (OS) and direction-selective (DS) cells tuned to objects that move or are oriented along one of four cardinal axes (Marshel et al., 2012; Piscopo et al., 2013; Zhao et al., 2013a), as well as a significant number of “suppressed-by-contrast” cells signalling uniformity of the visual field (Piscopo et al., 2013). Finally, a heterogeneous population of cells with long latencies and responses to both the on- and offset of light has been reported (Piscopo et al., 2013). It is currently unknown whether these response properties are inherited from the innervating retinal afferents or emerge *de-novo* in the dLGN by a combination of converging retinal inputs and dLGN-intrinsic computations.

2.5 Implications for dedicated visual circuits in dLGN

Parallel processing of sensory information is a commonly used strategy in the mammalian brain (Gasser & Erlanger, 1929; Nassi & Callaway, 2009). It is generally accepted that in mammals, processing of visual information is carried out along dedicated parallel pathways, where different types of visual information remain segregated to be combined later in cortex for different visual processing tasks. However, whether the mouse visual system uses similar processing strategies is still not well understood (Denman & Contreras, 2016).

Evidence for such parallel processing pathways has been shown in the mouse retina and V1. Recent study has estimated that the mouse retina harbours substantially more than 30 functional output channels (Baden et al., 2016), whereas Gao et al. (2010) suggested that mouse V1 contains distinct neuronal sub-population with highly correlated response properties, thereby supporting the idea of parallel processing strategies. Despite little physiological evidence for parallel information channels in the mouse dLGN, the functional subdivision into shell and core (discussed in 1.4.2.; Dhande et al., 2015; Dhande & Huberman, 2014; Martersteck et al., 2017) and multiple morphological populations preferring one of the two functional regions (discussed in 1.4.3; Krahe et al., 2011), indicate a possibility of parallel organization.

Recent genetic–anatomical tracing studies revealed that within the core X and Y cells project to layer IV of V1, whereas W cells in the shell project to layer I (Bickford et al., 2015; Cruz-Martín et al., 2014; Krahe et al., 2011). Moreover, all dLGN neurons, irrespective of their location, receive cortical input on their distal dendrites, but differ in innervations of their proximal dendrites (Bickford et al., 2015). The proximal dendrites of X and Y cells receive afferent input from non-direction-selective RGCs (Ecker et al., 2010; Huberman et al., 2008; Kay et al., 2011; Kim et al., 2010). In contrast, the proximal dendrites of W cells, located within the dLGN shell, combine input from both direction-selective RGCs (Cruz-Martín et al., 2014; Huberman et al., 2009; Kay et al., 2011; Kim et al., 2008; Rivlin-Etzion et al., 2011; Rousso et al., 2016) and the SC (Bickford et al., 2015). As suggested by Bickford et al. (2015), the integration of these two inputs may explain the emergence of direction-selectivity in geniculate shell neurons. Taken together, these results imply that visual information may be processed by separate visual streams along the retino-geniculo-cortical pathway.

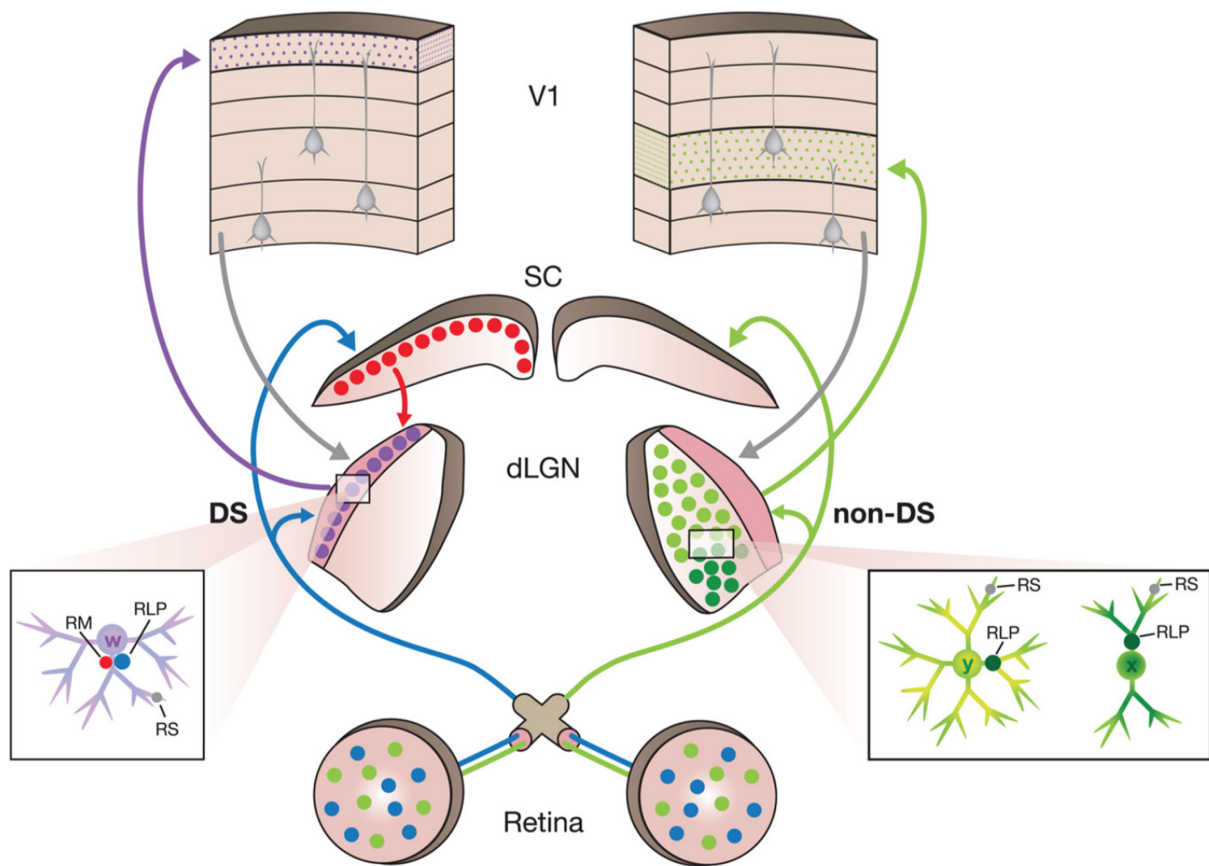


Figure 5 | Distinct functional circuits in the dLGN core and shell. X and Y cells in the core receive feedback from layer VI of V1 (grey, RS) on their distal dendrites and input from non-DSRGCs (green, RLP) on their proximal dendrites, and project predominantly to layer IV of V1. In contrast, W cells in the shell receive feedback from layer VI as well, but their proximal dendrites are innervated by convergent input from DS RGCs (blue, RLP), as well as from the SC (red, RM). Furthermore, in contrast to the core neurons, W cells in the shell project to superficial layer I of V1. Figure adapted with permission from Bickford et al., (2015).

2.6 The purpose of this study

In this study, we investigated the transformation of the visual signal along the retinogeniculate pathway. We sought to (i) functionally characterize the population of dLGN-projecting RGCs and (ii) dLGN neurons, and to link the results via (iii) computational modeling to determine how the visual representation in the dLGN arises from retinal inputs.

- (i) It has been shown that the mouse retina harbours more 30 different functional RGC types (Baden et al., 2016). How many of these types are a part of the retinogeniculate pathway is a matter of current debate. To answer this question, we selectively labeled and physiologically characterized dLGN-projecting RGCs.
- (ii) Recent studies in a mouse provide evidence for complex and diverse visual representations in the dLGN, going beyond the classical cat X/Y/W channels (reviewed in Kerschensteiner & Guido, 2017). We recorded the responses of dLGN neurons and quantitatively assessed the degree of diversity by decomposing the dLGN population response into a rich and highly diverse set of components.
- (iii) To address the dichotomy between functional and structural characterizations of retinogeniculate convergence (Chen & Regehr, 2000; Rompani et al., 2017), we investigated how the representation of visual information by neuronal populations changes between the retina and the dLGN.

In conclusion, this study provides fundamental insights into how the representation of visual information changes along the first stages of the mouse early visual system and represents a first step towards the development of a functional model of visual processing in the mammalian brain.

3 Materials & Methods

All procedures complied with the European Communities Council Directive 2010/63/EC and the German Law for Protection of Animals, and were approved by local authorities, following appropriate ethics review.

3.1 Functional characterization of dLGN-projecting RGCs

3.1.1 Animals and virus injection

For all experiments, we used 8 to 12 week-old animals (either sex) of the Ai95D reporter line (B6; 129S-Gt(ROSA)26Sor^{tm95.1(CAG-GCaMP6f)Hze}/J; JAX 024105). Ai95D features a floxed-STOP cassette preventing transcription of the genetically-encoded Ca²⁺ indicator GCaMP6f (Chen et al., 2013). Stereotaxic injection of a Cre-encoding Herpes-Simplex-Virus 1 (hEFlα-cre, MIT Vector Core, Cambridge, USA) into the dLGN resulted in retrograde Cre-recombinase expression in dLGN-projecting (dLGN-p) RGCs, where Cre-recombinase, in turn, removed the LoxP sites and activated GCaMP6f expression (Bouabe & Okkenhaug, 2013).

The surgical procedures have been described previously (Erisken et al., 2014; Vaiceliunaite et al., 2013). Here, in brief: Mice were fixed in a stereotactic frame (Neurostar, Tübingen, DE) and anesthetized using an isoflurane-mixture (4.0% induction, 1.2% maintenance) throughout the entire surgery. At the beginning of the surgical procedure, atropine (Atropine sulphate, 0.3 mg/kg, sc, Braun, Melsungen, DE) and analgesics (Buprenorphine, 0.1 mg/kg, sc, Bayer, Leverkusen, DE) were administered, and the eyes were protected continuously with an eye ointment (Bepanthen, Bayer, Leverkusen, DE). The animal's temperature was kept constant at 37°C via a closed loop temperature control system for small rodents (HD, Hugo Sachs Elektronik-Harvard Apparatus GmbH, March-Hugstetten, DE).

After a midline scalp incision, a small hole was made with a dental drill (Sinco, Jengen, DE) over the LGN located in the left hemisphere, 2.5 mm posterior to the bregma and 2.3 mm lateral from the midline. The virus was loaded in a sharp micropipette (GB150F-8P, Science Products, inner tip diameter 20-25 µm, Hofheim, DE) connected through a 10 µl Hamilton syringe (Hamilton Robotics, Reno, USA) to an Aladdin syringe pump (AL-1000, WPI Germany, Berlin, DE). A volume of 20-40 nl of virus was injected at a depth of 2.7 mm. The pipette was left in place for an additional 5 min to allow for viral diffusion. Antibiotics (Baytril, 5 mg/kg, sc, Bayer, Leverkusen, DE) and a longer lasting analgesic (Carprofen, 5 mg/kg, sc, Rimadyl, Zoetis, Berlin, DE) were administered continuously for 3 days post-surgery. Two-

photon Ca^{2+} imaging was carried out 3 weeks after viral injection.

3.1.2 Perfusion and retinal tissue preparation

Animals were housed under a standard 12 h day/night rhythm. Before perfusion and two-photon imaging, animals were dark-adapted for ≥ 1 h, and then deeply anaesthetized with sodium pentobarbital (Narcoren, 400 mg/kg, injected intraperitoneally, Böhringer Ingelheim, Ingelheim, DE). When the animal reached the asphyxia stage and complete paralysis, the eyes were enucleated, and the mouse was transcardially perfused with 0.2 M sodium phosphate buffered saline (PBS), followed by 4% paraformaldehyde (PFA) solution in PBS. The brains were post-fixed in PFA for 24 hours at 4° and then stored in PBS.

The eyes were dissected in carboxygenated (95% O_2 , 5% CO_2) extracellular solution containing (in mM): 125 NaCl, 2.5 KCl, 2 CaCl_2 , 1 MgCl_2 , 1.25 NaH_2PO_4 , 26 NaHCO_3 , 20 glucose, and 0.5 L-glutamine (pH 7.4). The retina was extracted from the eyecup and flat-mounted onto a ceramic filter (Anodisc #13, 0.2 μm pore size, GE Healthcare, Buckinghamshire, UK) with the ganglion cell layer (GCL) facing up and transferred to the recording chamber of the microscope, where it was continuously perfused with carboxygenated solution at $\sim 36^\circ\text{C}$. In all experiments, $\sim 0.1 \mu\text{M}$ Sulforhodamine-101 (SR101, Sigma, Steinheim, DE) was added to the extracellular solution to reveal blood vessels and any damaged cells in the red fluorescence channel of the microscope (Euler et al., 2009). All procedures were carried out under dim red ($> 650 \text{ nm}$) illumination.

3.1.3 Histological reconstruction of injection sites

To verify the injection site within the dLGN, we used histological reconstructions. Brains were sliced for coronal sections (50 μm) using a vibratome (Microm HM 650 V, Thermo Fisher Scientific, Waltham, Massachusetts, USA) and mounted on glass slides with DAPI-containing mounting medium (Vectashield DAPI, Vector Laboratories Ltd, Peterborough, UK), which labels the cell nuclei, and cover-slipped. Brain slices were inspected using a Zeiss Imager.Z1m epi-fluorescent microscope (Zeiss, Oberkochen, DE) for the baseline fluorescence of the GCaMP6f.

3.1.4 Two-photon Ca^{2+} imaging and light stimulation

We used a MOM-type two-photon microscope (designed by W. Denk, MPI, Martinsried; purchased from Sutter Instruments/Science Products, Hofheim, Germany). Design and procedures were described previously (Baden et al., 2016; Euler et al., 2009). In brief, the system was equipped with a mode-locked Ti:Sapphire laser (MaiTai-HP DeepSee, Newport

Spectra-Physics, Darmstadt, Germany) tuned to 927 nm, two fluorescence detection channels for GCaMP6f (HQ 510/84, AHF/Chroma Tübingen, Germany) and SR101 (HQ 630/60, AHF), and a water immersion objective (W Plan-Apochromat 20x/1.0 DIC M27, Zeiss, Oberkochen, Germany). For image acquisition, we used custom-made software (ScanM, by M. Müller, MPI, Martinsried, and T. Euler) running under IGOR Pro 6.37 for Windows (Wavemetrics, Lake Oswego, OR, USA), taking 64×64 pixel image sequences (7.8 frames per s) for activity scans or 512×512 pixel images for high-resolution morphology scans.

For light stimulation, we focused a DLP beamer (K11, Acer) through the objective. The beamer was fitted with band-pass-filtered light-emitting diodes (LEDs) (“green”, 578 BP 10; and “blue”, HC 405 BP 10, AHF/Chroma) to match the spectral sensitivity of mouse M- and S-opsins (Baden et al., 2013; Peichl, 2005). LEDs were synchronized with the microscope’s scan retrace. Stimulator intensity (as photoisomerisation rate, 10^3 P*/s/cone) was calibrated as described previously (Euler et al., 2009) to range from 0.6 and 0.7 (black image) to 18.8 and 20.3 for M- and S-opsins, respectively. An additional, steady illumination component of $\sim 10^4$ P*/s/cone was present during the recordings because of two-photon excitation of photopigments (for detailed discussion, see Euler et al., 2008, Baden et al., 2013). For all experiments, the tissue was kept at a constant mean stimulator intensity level for at least 15 s after the laser scanning started and before light stimuli were presented.

Four types of light stimuli were used (Fig. 8d, top) (Baden et al., 2016): (i) a full-field ($800 \times 600 \mu\text{m}$) “chirp” stimuli consisting of a bright step and two sinusoidal intensity modulations, one with increasing frequency (0.5-8 Hz) and one with increasing contrast; (ii) a 0.3×1 mm bright bar moving at 1 mm s^{-1} in eight directions; (iii) alternating blue and green 3-s flashes; and (iv) binary dense noise (20×15 matrix with $40 \mu\text{m}$ pixel-side length; each pixel displayed an independent, balanced random sequence at 5 Hz for 5 minutes) for space-time receptive field mapping. All stimuli, except (iii), were achromatic, with matched photo-isomerisation rates for mouse M- and S-opsins.

3.1.5 Data analysis

The data analysis was performed using IGOR Pro (Wavemetrics, Lake Oswego, OR, USA), MATLAB (The Mathworks, Natick, Massachusetts, USA) and iPython / Jupyter Notebooks (distribution by Anaconda Inc., Austin, TX).

3.1.6 Pre-processing

Regions of interest (ROIs) were manually drawn around the GCaMP6f-expressing somata in the recording fields. The Ca^{2+} traces for each ROI were extracted (as $\Delta F/F$) using the image analysis toolbox SARFIA for IGOR Pro (Dorostkar et al., 2010). A stimulus time marker embedded in the recorded data served to align the Ca^{2+} traces relative to the visual stimulus with a temporal precision of 2 ms. For this, the timing for each ROI was corrected for sub-frame time-offsets related to the scanning. The Ca^{2+} traces were up-sampled to 500 Hz, then de-trended using a high-pass filtering above ~ 0.1 Hz, and resampled to 7.8 Hz. For all stimuli except the dense noise (for RF mapping), the baseline was subtracted (median of first eight samples), median activity $r(t)$ across stimulus repetitions computed (typically three to five repetitions) and normalized such that $\max_t(|r(t)|) = 1$. HDF5 files containing the pre-processed Ca^{2+} traces for each ROI were further analysed using Python and Jupyter notebooks.

3.1.7 Receptive field mapping

The linear RFs of the neurons were mapped by computing the Ca^{2+} transient-triggered average. To this end, the temporal derivative of the Ca^{2+} response was resampled at 10-times the stimulus frequency and the Matlab's *findpeaks* function was used to detect the times t_i at which Ca^{2+} transients occurred. The minimum peak height was set to 1 s.d., where the s.d. was robustly estimated using:

$$\bar{\sigma} = \frac{\text{median}(|\dot{r}(t)|)}{0.6745}$$

We then computed the Ca^{2+} transient-triggered average stimulus, weighting each sample by the steepness of the transient:

$$F(x, y, \tau) = \frac{1}{M} \sum_{i=1}^M \dot{c}(t_i) S(x, y, t_i + \tau)$$

Here, $S(x, y, t)$ is the stimulus, τ is the time lag (ranging from approximately -320 to $1,380$ ms) and M is the number of Ca^{2+} events. We smoothed this raw RF estimate using a 5×5 pixel Gaussian window for each time lag separately. We used singular value decomposition (SVD) to extract temporal and spatial RF kernels.

To extract the RF's position and scale, we fitted it with a 2D Gaussian function using Matlab's *lsqcurvefit*. The time course of the receptive field $F_{tc}(\tau)$ was estimated by the average of the eight pixels closest to the fitted RF centre (according to the Mahalanobis distance) weighted by a Gaussian profile. RF quality (Qi_{RF}) was measured as one minus the fraction of variance explained by the Gaussian fit \bar{F}_{map} .

$$Qi_{RF} = \frac{Var[F_{map} - \bar{F}_{map}]}{Var[F_{map}]}$$

3.1.8 Direction and orientation selectivity

To extract time course and directional tuning of the Ca^{2+} response to the moving bar stimulus, we performed a singular value decomposition (SVD) on the T by D normalized mean response matrix M (times samples by number of directions; $T = 32$; $D = 8$):

$$[U, S, V] = svd(M)$$

This procedure decomposes the response into a temporal component in the first column of U and a direction dependent component or tuning curve in the first column of V , such that the response matrix can be approximated as an outer product of the two:

$$M \approx S_{11} U_{:1} V_{:1}^T$$

An advantage of this procedure is that it does not require manual selection of time bins for computing direction tuning, but extracts the direction-tuning curve given the varying temporal dynamics of different neurons.

To measure direction selectivity (DS) and its significance, we projected the tuning curve $V_{:1}$ on a complex exponential $\phi_k = \exp(i\alpha_k)$, where α_k is the direction of the k_{th} condition:

$$K = \phi^T V_{:1}$$

This is mathematically equivalent to computing the vector sum in the 2D plane or computing the power in the first Fourier component. We computed a DS index as the resulting vector length:

$$DSi = |K|$$

correcting for the direction spacing. We additionally assessed the statistical significance of direction tuning using a permutation test (Ecker et al., 2014). To this end, we created surrogate trials (= stimulus repetitions) by shuffling the trial labels to destroy any relationship between condition and response, then computed the tuning curve for each surrogate trial and projected it on the complex exponential ϕ . Carrying out the procedure 1,000 times generated a null distribution for K , assuming no direction tuning. We used the percentile of the true K as the P value for direction tuning (Baden et al., 2016).

Orientation selectivity (OS) was assessed in an analogous way. However, we used the complex exponential $\phi_k = \exp(2i\alpha_k)$, corresponding to the second Fourier component.

3.1.9 Other response measures

Response quality index. To measure how well a cell responded to a stimulus (local and full-field chirp, flashes), we computed the signal-to-noise ratio

$$Qi_{RF} = \frac{Var[\langle C \rangle_r]_t}{\langle Var[C]_t \rangle_r}$$

where C is the T by R response matrix (time samples by stimulus repetitions), while $\langle \cdot \rangle_x$ and $Var[\cdot]_x$ denote the mean and variance across the indicated dimension, respectively (Baden et al., 2016). For further analysis, we used only cells that responded well to the chirp and/or to the moving bar stimulus ($Qi_{chirp} > 0.45$ or $Qi_{DS} > 0.6$; cf. Fig. 7c in Baden et al., 2016). Of the original $n = 581$ ROIs, $n = 251$ ROIs passed this criterion.

Full-field index. The full-field index was measured as

$$FF_i = \frac{QI_{DS} - QI_{chirp}}{QI_{DS} + QI_{chirp}}$$

comparing the response quality to a local stimulus (moving bar) and a global stimulus (chirp).

ON-OFF index. ON-OFF preference was computed as

$$OO_i = \frac{\langle r_{ON} \rangle_t - \langle r_{OFF} \rangle_t}{\langle r_{ON} \rangle_t + \langle r_{OFF} \rangle_t}$$

where r_{ON} and r_{OFF} are defined as the activity during the response to the leading edge of the moving bar (the first 400 ms of the ON response) and the trailing edge of the moving bar (the first 400 ms of the OFF response).

Colour selectivity index. Colour selectivity was measured for the ON response using

$$GB_{ON} = \frac{\max(r_{ON,green}^2) - \max(r_{ON,blue}^2)}{\max(r_{ON,green}^2) + \max(r_{ON,blue}^2)}$$

and for the OFF response using an analogous definition. Here, $r_{ON,green}$ and $r_{ON,blue}$ are the responses in a time window of 1,280 ms after onset of the green and blue stimulus, respectively.

3.1.10 Signal deconvolution

Comparing neural activity measured with different methods (i.e. spikes vs. Ca^{2+} signals; different Ca^{2+} indicators) is a non-trivial task. To assign dLGN-p RGCs to previously characterized RGC types, we needed account for the fact that the different Ca^{2+} indicators used (OGB-1 vs. GCaMP6f) have different kinetics (Chen et al., 2013). We decided to convert both signals to a “common currency”, by deconvolving both signal types using Ca^{2+} kernels calculated for each indicator separately using Ca^{2+} recordings of multiple ROIs ($n_{OGB-1} = 327$; $n_{GCaMP6f} = 19$) to the white noise stimulus, and averaging thresholded Ca^{2+} peak events (>80% of the maximum normalized activity). Since the rise of the fluorescence is fast compared to the decay and similar for OGB-1 and GCaMP6f, we cut the Ca^{2+} kernels to include only the falling phase; its area under the curve (AUC) was normalized to 1. (Fig. 6).

3.1.11 Assigning dLGN-projecting RGCs to previously characterized RGC types

In the functional classification survey, Baden and colleagues (2016) identified 49 functional RGC clusters (RGC-all cluster). All clusters were sorted based on their functional similarity and merged in the absence of evidence to count them as separate cell types, resulting into 32 functionally unique groups. Each group thus represents an RGC type based on functional properties and additional domain knowledge, including morphology, genetic and immunohistochemical labels.

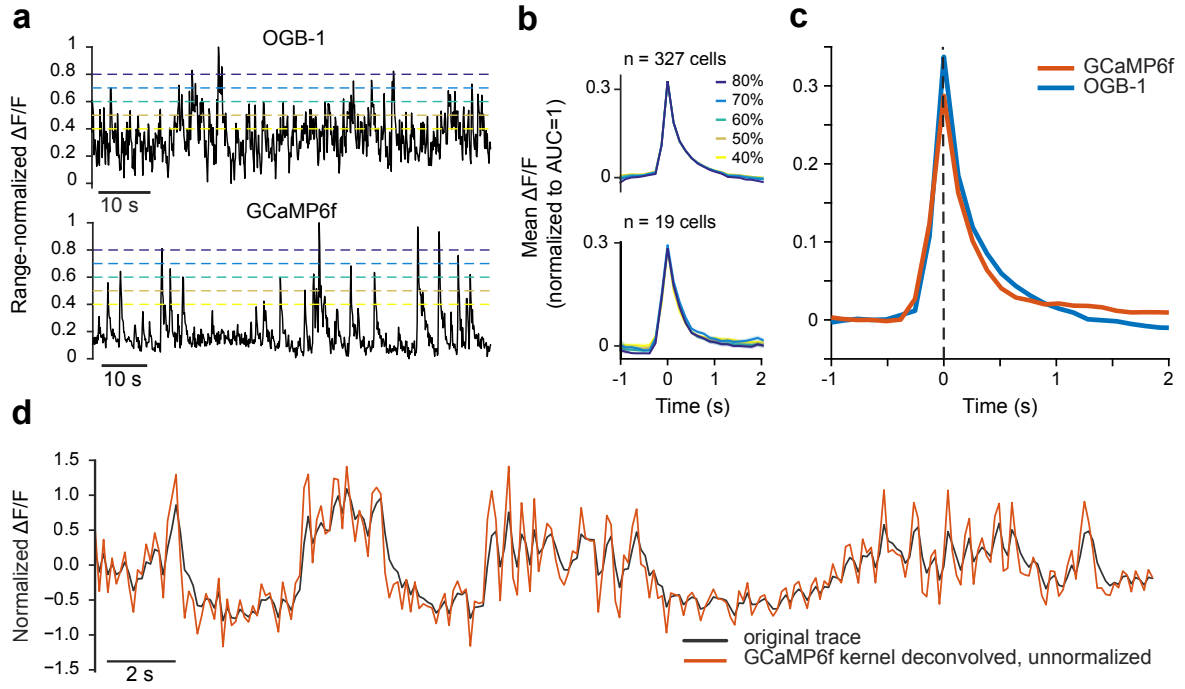


Figure 6 | Deconvolution. **a**, Raw traces to binary white noise stimulus with various Ca^{2+} event thresholds (top: OGB-1; bottom: GCaMP6f). **b**, Extracted mean Ca^{2+} indicator kernels for OGB-1 (top) and GCaMP6f (bottom) for the thresholds shown in **a**. **c**, Superposition of OGB-1 and GCaMP6f kernels. **d**, Example of mean normalized GCaMP6f trace (in black), and deconvolution with the GCaMP6f kernel (in orange).

The pre-processed ROI traces of dLGN-p RGCs ($n = 251$) were assigned to functional RGC population clusters (Baden et al., 2016), by identifying for each dLGN-p cell the cluster with the best matching response properties. After deconvolution with the respective Ca^{2+} kernel (see above), we calculated the Pearson product-moment correlation coefficients between a dLGN-p cell's mean trace (over trials) and all cluster mean traces (over all cells in a RGC-all cluster) for the chirp and the moving bar stimuli. To combine the information about stimulus-specific correlations and stimulus-specific cell response quality, we generated an overall match index (MI) of each dLGN-p cell to all RGC-all clusters:

$$MI = \frac{Q_{i_{chirp}}}{Q_{i_{chirp}} + Q_{i_{bar}}} * \rho_{chirp} + \frac{Q_{i_{bar}}}{Q_{i_{chirp}} + Q_{i_{bar}}} * \rho_{bar}$$

Finally, each dLGN-p cell was assigned to the cluster with which it had the highest MI. In addition, we used soma area and DSI to pre-constrain the cluster assignment of DS cells ($p < 0.05$) and cells with large somata (area > population mean + 1 SD) to the subset of DS cell and alpha RGC clusters.

3.1.12 Statistical significance of RGC clusters

We used a permutation test to assess the statistical significance of deviations of relative cluster proportions in the dLGN-p RGCs subpopulation compared to the total RGC population. To this end, we created an artificial distribution of cells-per-cluster percentages that would be expected if the cluster proportions of dLGN-p RGCs were the same as those of the RGC population. To generate the artificial distribution, we allocated surrogate cells to the different clusters, where each cluster was assigned with a probability according to the proportion of cells in the total RGC population. We averaged across 1000 resampling repetitions per cluster, and thus obtained a distribution of cell-per-cluster percentages for every cluster bin in the RGC population. We then compared the distribution to the sample percentages in the dLGN-p RGC subpopulation as the percentile scores in the respective cluster distribution. 0th percentile scores for clusters that contained no cells in the dLGN-p RGC subpopulation were set to percentile score = $1/(\# \text{ resampling repetitions})$, thus obtaining a percentile-value minimum of 0.1. After correcting percentile scores for false discovery rate (FDR, Benjamini-Hochberg), percentile scores were considered significant if the percentile score was $\leq 0.5^{\text{th}}$ or $\geq 99.5^{\text{th}}$ percentile, i.e. a two-tailed test for $\alpha = 0.01$. For the \log_2 -ratio (% dLGN-p RGCs/ % RGC population), we avoided '-inf' values for clusters that did not receive cells in the dLGN-p RGC subpopulation via additive smoothing, i.e. by adding $k=1$ cell to each cluster cell count n per default and normalizing the cluster cell counts by $n+k$.

3.1.13 Linear feed-forward model

For modelling dLGN responses as a linear combination of weighted RGCs (Fig. 18c), we used the RGC cluster means (Baden et al., 2016) of those clusters that were assigned more than one GCaMP6f cell. The dLGN dataset was down-sampled and convolved with an artificial OGB-1 kernel to allow for a direct comparison of the dLGN traces with the dLGN-p RGC Ca^{2+} responses. The weights were computed, using a linear-regression algorithm (*lsqlin*, MATLAB) with a non-negativity constraint, thus allowing only positive combinations of the weights. The model adds the mean response from RGC clusters multiplied by their weights to predict the response of dLGN neurons (Fig. 18c). The model performance was cross-validated using repeated random sub-sampling technique with 1,000 repetitions. The trials were randomly shuffled and divided into a training set (50% trials) and a validation set (50% trials). Both sets contained unique trials with no duplicates. The training set was used to compute the weights and the performance of the model was evaluated on the validation set. The performance of the model represents the mean value across the repeats.

3.2 Functional characterization of dLGN responses

3.2.1 Animals and surgical procedures

For all experiments, we used 8- to 12-week-old wild type mice (C57BL/6J) of either sex. For the initial surgery procedures see section 3.1.1.

After a midline scalp incision and skin removal, a drop of H₂O₂ (3 %) was applied on the surface of the skull for the removal of tissue residues. A custom lightweight aluminium head post was placed on the posterior skull using OptiBond FL primer and adhesive (Kerr dental, Rastatt, DE) and Tetric EvoFlow dental cement (Ivoclar Vivadent, Ellwangen, DE). Miniature ground and reference screws (00-96 X 1/16 stainless steel screws, Bilaney, USA) soldered to custom-made connector pins were placed bilaterally over the cerebellum. A well of dental cement was formed to hold the silicone elastomer sealant Kwik-Cast (WPI Germany, Berlin, DE) covering the skull. Antibiotics (Baytril, 5 mg/kg, sc, Bayer, Leverkusen, DE) and a longer lasting analgesic (Carprofen, 5 mg/kg, sc, Rimadyl, Zoetis, Berlin, DE) continued to be administered for 3 days post-surgery.

After recovery, animals were familiarized with a simulation of the experimental procedures in multiple training sessions until they were deemed comfortable with the conditions. Before experiments, a craniotomy (ca. 1 mm²) was performed over dLGN (2.3 mm lateral to the midline and 2.5 mm posterior to bregma), which was re-sealed with Kwik-Cast (WPI Germany, Berlin, DE). Experiments started one day after craniotomy and were continued on consecutive days as long as electrophysiological signals remained of high quality.

3.2.2 In-vivo multisite extracellular recordings

Our experimental configuration for *in-vivo* recordings was based on Dombeck et al. (2007). The mouse was head-fixed and could run freely on an air-suspended styrofoam ball while stimuli were presented on a gamma-corrected LCD screen (Samsung SyncMaster 2233). Extracellular neural signals were recorded 2.5 mm posterior from bregma and 2.3 mm lateral from midline through a small craniotomy window over dLGN with 32-channel edge silicon probes (Neuronexus, A1x32Edge-5mm-20-177- A32, Ann Arbor, USA). Neurons were verified as belonging to the dLGN based on the characteristic RF progression from top to bottom along the electrode shank (Fig. 13c), the preference for high temporal frequencies, and a high prevalence of F1 responses to drifting gratings (Grubb, 2003; Piscopo et al., 2013). Ball movements were registered at 90 Hz by two optical mice connected to a micro-

controller (Arduino Duemilanove). Eye movements were monitored under infrared light illumination (Guppy AVT camera, frame rate 50 Hz, Allied Vision, Exton, USA).

3.2.3 Visual Stimulation

We used custom software (EXPO, <https://sites.google.com/a/nyu.edu/expo/> home) to present visual stimuli on a gamma-calibrated liquid crystal display (LCD) monitor (Samsung SyncMaster 2233RZ; mean luminance 50 cd/m², 60 Hz) at 25 cm distance to the animal's right eye. Four types of light stimuli were presented:

Contrast stimulus. To measure contrast response function, we presented drifting sinusoidal gratings at a single orientation and 12 different randomly interleaved contrasts were presented for duration of 2 sec with a pause of 0.5 sec between trials.

Full-field chirp stimulus. The stimulus was designed analogously to the one used for the visual stimulation of the RGCs. In brief, the chirp stimulus consists of a bright step and two sinusoidal intensity modulations, one with increasing frequency (0.5-8 Hz) and one with increasing contrast.

Spatial-temporal-frequency-orientation (STFO) stimulus. To capture preferred tuning properties of a large number of neurons simultaneously, we designed a stimulus sequence consisting of drifting sinusoidal gratings with 8 orientations, 6 temporal (TF) (0.5, 1, 2, 4, 8, 16 cycles/sec) and 2 spatial frequencies (SF) (0.5, 0.15 cycles/deg). The trials were randomly interleaved and presented for 1 sec with a 0.1 sec pause between trials. The stimulus was shown at 100% contrast with the background at mean luminance.

Sparse noise stimulus. For receptive field mapping, white or black square stimuli (5 deg square) were presented at various positions on a grey background of mean luminance (50 cd/m²). The squares were presented for 200 ms each at every position on a 12 x 12 square grid of 60 degrees.

Spontaneous activity "stimulus": For measurements of spontaneous activity, we recorded neural responses during the presentation of a mean luminance grey screen.

All light stimuli were presented in a full-field mode and, except of the chirp stimulus, a blank screen condition (mean luminance) was included in all stimuli to estimate the spontaneous firing rate.

3.2.4 Data analysis

Data analysis was performed using Matlab (The Mathworks, Natick, Massachusetts, USA). Data were organized in a custom written schema using the relational database framework "DataJoint" (Yatsenko et al., 2015, Matlab version: <https://github.com/datajoint/datajoint-matlab>).

3.2.5 Unit extraction and spike sorting

Wideband extracellular signals were digitized at 30 kHz (Blackrock microsystems, Blackrock Microsystems Europe GmbH, Hannover DE) and analysed using the NDManager software suite (Hazan et al., 2006). The LFP was computed by down-sampling the signal to 1250 Hz. To isolate individual neurons from linear arrays, we grouped neighbouring channels into 5 equally sized "virtual octrodes" (8 channels per group with 2 channel overlap for 32 channel probes). Using an automatic spike detection threshold (Quiroga et al., 2004) multiplied by a factor of 1.5, spikes were extracted from the high-pass filtered continuous signal for each group separately. The first 3 principal components of each channel were used for semi-automatic isolation of single neurons with KlustaKwik (Henze et al., 2000). Clusters were manually refined with Klusters (Hazan et al., 2006). We assigned each unit to the contact with the largest waveform. Units were given a subjective quality score by the manual sorter, the firing rate, the cleanness of the refractory period, and the stability over time. To avoid duplication of neurons extracted from linear probe recordings, we computed cross-correlation histograms (CCHs, 1 ms bins) between pairs of neurons from neighbouring groups. Pairs for which the CCH's zero-bin was 3 times larger than the mean of non-zero-bins were considered to be in conflict. For each conflicting pair, the cell with the best score was kept. Conflicts across pairs were resolved by collecting all possible sets of cells and by keeping the set with the best total score.

3.2.6 Receptive field mapping

Receptive fields were mapped by reverse correlating unit activity to the sparse noise stimulus and fitting the centre of a two-dimensional ellipse / 2D-Gaussian for both ON- and OFF-fields (Liu et al., 2010):

$$f(x, y) = \frac{A}{2\pi ab} \exp\left(-\frac{x'^2}{2a^2} - \frac{y'^2}{2b^2}\right)$$

where A is the maximum amplitude, a and b are half-axes of the ellipse, and x' and y' are transformations of the stimulus coordinates x and y , taking into account the angle θ and the

coordinates of the centre (x_c , y_c) of the ellipse. For each contact, we computed a single RF centre by averaging coordinates of the best-fit ON and OFF subfield (explained variance > 70%).

3.2.7 Contrast response function

Contrast responses were fitted with a hyperbolic ratio function (Albrecht & Hamilton, 1982):

$$r_c = r_0 \frac{r_{max} * c^n}{(c_{50}^n + c^n)}$$

The function has four parameters: Baseline response r_0 , responsiveness r_{max} , semi-saturation contrast c_{50} , and exponent n .

3.2.8 Tuning

Orientation tuning curves were fitted with a sum of two Gaussians with peaks θ_{pref} and $\theta_{pref} - \pi$ of different amplitudes A_1 and A_2 but equal width σ , with a constant baseline r_0 (Katzner et al., 2011). SF and TF tuning curves were taken at the preferred direction for each neuron and orientation and direction-tuning curves were taken at the optimal SF and TF for each neuron.

Direction selectivity. Direction selectivity index (DSI) was calculated as the ratio of

$$DSI = \frac{r_{pref} - r_{opp}}{r_{pref} + r_{opp}}$$

where r_{pref} was the response at the preferred direction and r_{opp} was the response at the opposite direction. We additionally assessed the statistical significance of direction tuning using a permutation test (section 3.1.8) (Ecker et al., 2014).

Orientation selectivity. Orientation selectivity index (OSI) was computed as:

$$OSI = \frac{r_{pref} - r_{ortho}}{r_{pref} + r_{ortho}}$$

where r_{pref} is the response to the preferred orientation and r_{ortho} is the response to the orthogonal orientation (CM & MP, 2008).

3.2.9 Other response measurements

Response quality index. $Q_{i_{RF}}$ was computed analogous to the description in section 3.1.9.

Chirp quality index. To determine whether a neuron was visually driven by the full-field chirp, we separated the stimulus into two segments (e.g., separated a 32-s stimulus into two 16-s segments), and computed the average between-trial correlations (CCs) (responses binned at the stimulus frame rate) within segment and between segments. Only those cells that had significantly higher within-segment CCs ($Q_{i_{chirp}}$, $P < 0.01$, Wilcoxon rank sum test) and firing rate > 1 spike/s were considered to be visually responsive.

STFO correlation value. To assure neuronal response stability and to determine, whether there are neurons, which did not respond to the full-field chirp stimulus, we played the STFO stimulus directly before and after the chirp stimulus, and performed linear regression analysis (Fig. 14). To determine how well the model predicts the data, we computed a correlation value R :

$$R = \sqrt{1 - \frac{\sum_{i=1}^n (y_i - \hat{y}_i)^2}{\sum_{i=1}^n (y_i - \bar{y}_i)^2}}$$

where y represents *observed* values, \hat{y} represents the *predicted* values of y and \bar{y} is the mean of y .

For further analysis, we used only cells that responded well to the chirp stimulus ($Q_{i_{RF}} \geq 0.05$ and $Q_{i_{chirp}} \leq 0.001$) or had a high STFO correlation value ($R > 0.65$, Fig. 15b).

3.2.10 Non-negative matrix factorization

NNMF is a matrix decomposition approach, which decomposes a non-negative matrix into two low-rank non-negative matrices, representing, for example, visual components and their weights (Nikolaus & Paper, 2007). We applied sparse non-negative matrix factorization with the non-negative least square optimization (Kim & Park, 2007), as implemented in the *NMF MATLAB Toolbox* by (Li & Ngom, 2013; <https://sites.google.com/site/nmftool/>), to extract visual response components from the dLGN responses to the chirp stimulus. Given a positive matrix A of size $N \times M$ and a desired number of features (K), the NMF algorithm

iteratively computes an approximation $A \sim WH$, where W and H are non-negative matrices with respective sizes $N \times K$ and $K \times M$. The optimal number of components for the NNMF algorithm was selected based on the method proposed by (Frigyesi & Höglund, 2008). We performed NNMF for increasing K and computed residual error (RE) of A for each K and compared it to RE of A_{perm} . A_{perm} denotes the matrix A with rows permuted or every column. Because of the random initialization of the NNMF algorithm, the factorization was repeated 50 times for each K .

$$RE = |A - W * H|$$

$$RE = |A_{perm} - W_{perm} - H_{perm}|$$

When comparing RE in function of K , the RE decreases exponentially with increasing K for the original dataset, but only linearly for the randomized dataset. The slope represents a measure of how much information is lost as K decreases. Therefore, the slope of the RE of A , which is larger than A_{perm} , allows us to determine the smallest K , where the information is still above noise level. To ensure robustness of the NNMF algorithm, the factorizations were repeated 100 times using the previously determined K and evaluated according to their RE. The W/H -pair with the smallest RE was selected for further analysis.

3.2.11 Correlating dLGN response components with RGC clusters

The dLGN response components were down-sampled to match the RGC cluster sampling rate used for recording the responses in the RGC clusters (Baden et al., 2016) and convolved with an artificial OGB-1 kernel. The convolved dLGN response components were then correlated with dLGN-p RGC clusters. The best matching cluster corresponded to the cluster with highest correlation value.

3.2.12 Dendrogram

The components were organized into a hierarchical cluster tree by a single linkage algorithm using Euclidean distances and the Ward's minimum variance method (Ward Jr., 1963). The results were plotted using the dendrogram function and the leaf order was optimized using the Matlab function *optimalleaforder*.

3.2.13 Locomotion and speed Tuning

The ball movements were recorded by two optical mice, which were placed at the sides of the spherical treadmill. We computed locomotion as the Euclidean norm of three perpendicular components of the ball velocity (Dombeck et al., 2007). To determine

modulations of tuning properties by locomotion, we recorded spontaneous activity during grey screen presentation. For further analysis, we included only neurons that passed our chirp quality criteria, had an average firing rate > 0.3 spike/s for the spontaneous condition and a STFO correlation values > 0.65 . Neuronal speed tunings were determined as previously described in (Saleem et al., 2013). In brief, speed traces were smoothed with a Gaussian filter ($\sigma = 150$ ms), re-sampled at 60 Hz, and binned such that each bin contained equal amounts of time (> 30 s). Unsmoothed neural responses were binned at 60 Hz. Neurons were considered speed modulated if the variance of mean responses across bins was greater than 99.9% of the variance of shuffled responses ($p < 0.001$). To characterize the run speed responses, we fitted the mean responses to speed s ($s > 1$ cm/s) by the following function:

$$y(s) = y_{max} \exp\left(-\frac{(s - s_{max})^2}{\sigma(s)}\right)$$

where s is speed ($s > 1$ cm/s), and σ is σ_- for $s < s_{max}$ and σ_+ for $s > s_{max}$. Responses were classified as monotonically increasing, monotonically decreasing or band-pass tuned, depending on the best fit that resulted due to different constraints on s_{max} (Saleem et al., 2013).

3.2.14 Histological reconstruction of recording sites

To verify recording sites from dLGN, we used histological reconstructions. Before recording from the dLGN, electrodes were coated with a red-shifted fluorescent lipophilic tracer (DiD; Thermo Fisher Scientific, Waltham, Massachusetts, USA). After the last recording session, mice were transcardially perfused and the brain fixed in a 4% paraformaldehyde phosphate buffered saline (PBS) solution for 24 hours and then stored in PBS. Brains were sliced for coronal sections (50 μ m) using a vibratome (Microm HM 650 V, Thermo Fisher Scientific, Waltham, Massachusetts, USA) and mounted on glass slides with Vectashield DAPI (Vectashield DAPI, Vector Laboratories Ltd, Peterborough, UK), and coverslipped. Slices were inspected for DAPI and DiD presence using a Zeiss Imager.Z1m fluorescent microscope (Zeiss, Oberkochen, DE).

4 Results

4.1 Functional characterization of dLGN-projecting RGCs via retrograde viral tracing

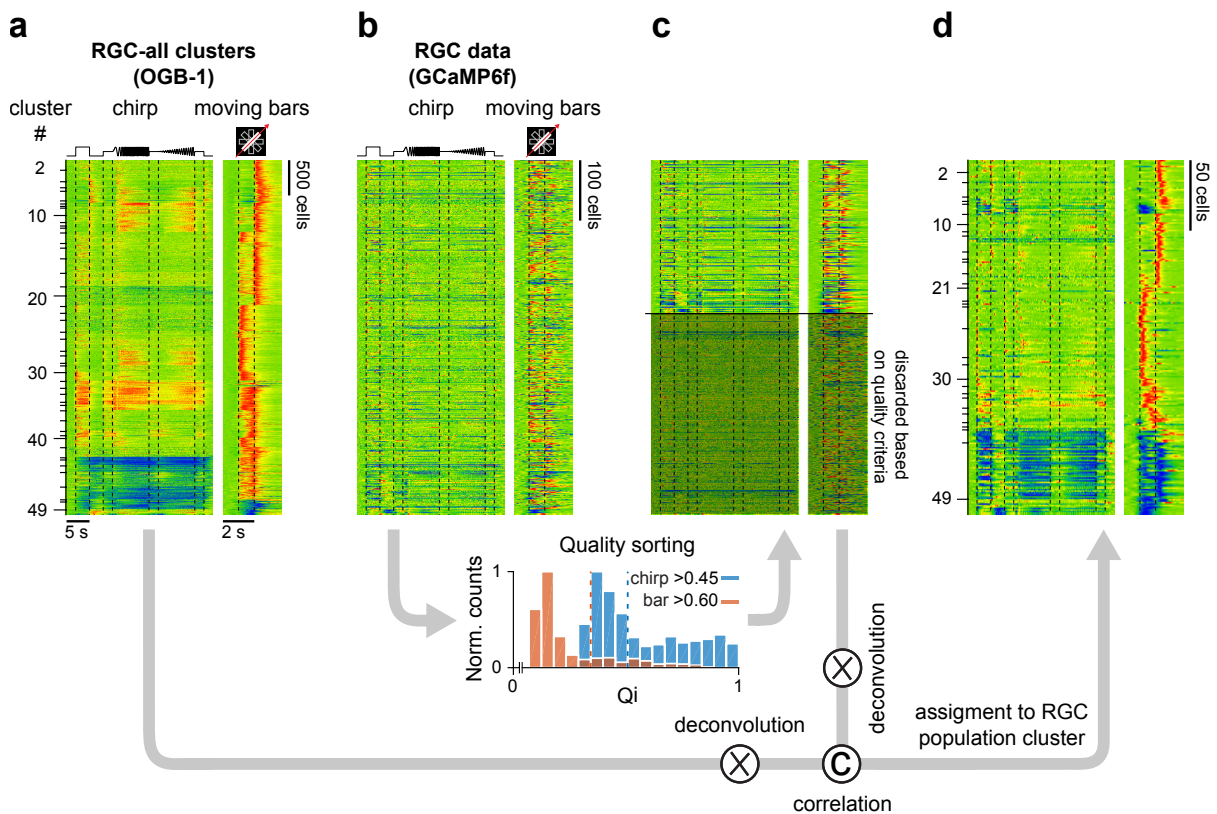


Figure 7 | Overview of analysis steps for the functional characterization of dLGN-projecting RGCs.

a. Heat maps of Ca^{2+} RGC-all cluster responses to the chirp and the bar stimulus ($n = 49$ RGC clusters, Baden et al., 2016). Each line represents responses of a single cell with activity colour-coded such that warmer colours represent increased activity, and the cluster height indicates the number of included cells.

b. Top: Heat maps of GCaMP6f dLGN-p RGC responses to the chirp and the bar stimulus. Bottom: Distribution of Q_i values; only cells with $Q_i > 0.45$ for the chirp and with $Q_i > 0.6$ for the bar stimulus were considered for further processing.

c. Heat maps of sorted GCaMP6f dLGN-p RGC responses ($n = 251$) and discarded cells that did not pass the quality criteria ($n = 330$).

d. Heat maps of GCaMP6f dLGN-p RGCs, assigned to RGC population cluster.

To identify dLGN-projecting (dLGN-p) RGCs, we injected a Cre-encoding retrograde Herpes-Simplex-Virus 1 (LT HSV-hEF1a-cre; Neve, 2012) into the dLGN of a transgenic reporter mouse line with a floxed genetically encoded Ca^{2+} indicator (GCaMP6f) (Chen et al., 2013; Madisen et al., 2015). After transducing the axon terminals in the dLGN (Antinone & Smith, 2010; McGavern & Kang, 2011), the virus is retrogradely transported to the cell nuclei, where it triggers the expression of Cre-recombinase and, subsequently, the Cre-dependent expression of GCaMP6f. Since the virus does not spread trans-synaptically, it only labels cells with afferents in the dLGN. This enabled us to label only the subset of dLGN-p RGCs in the retina (Fig. 8a).

We histologically confirmed the target location of the virus injection and that it did not diffuse beyond the dLGN. As expected from earlier studies, we found retrogradely labelled neurons in other dLGN-p structures besides the retina, including the superior colliculus (Fig. 8b, centre), the thalamic reticular nucleus and the deep layers of primary visual cortex (Fig. 8b, bottom) (Guillery & Sherman, 2002; Harting et al., 1991).

We then used two-photon Ca^{2+} imaging to measure the light-evoked responses of the dLGN-p RGCs (Fig. 7b). On average, the virus labelled nine RGCs per $110 \times 110 \mu\text{m}$ recording field ($n = 68$) (Fig. 8c, top). We probed the response properties of the LGN-p RGCs across the whole retina with a standardized stimulus set used in the previous RGC classification study (Baden et al., 2016). The Ca^{2+} -responses (Fig. 8c, bottom) of the labelled RGCs were analysed using manually drawn regions of interest (ROIs) ($n = 581$) in the recording fields. In addition to the classical ON/OFF-response types and the direction selective RGCs (Ellis et al., 2016; Rivlin-Etzion et al., 2011), we found cells among the dLGN-p RGCs that, for example, responded differently to local and full-field stimuli, showed preference to higher or lower frequency stimulation or were suppressed by frequency and contrast (Fig. 8d).

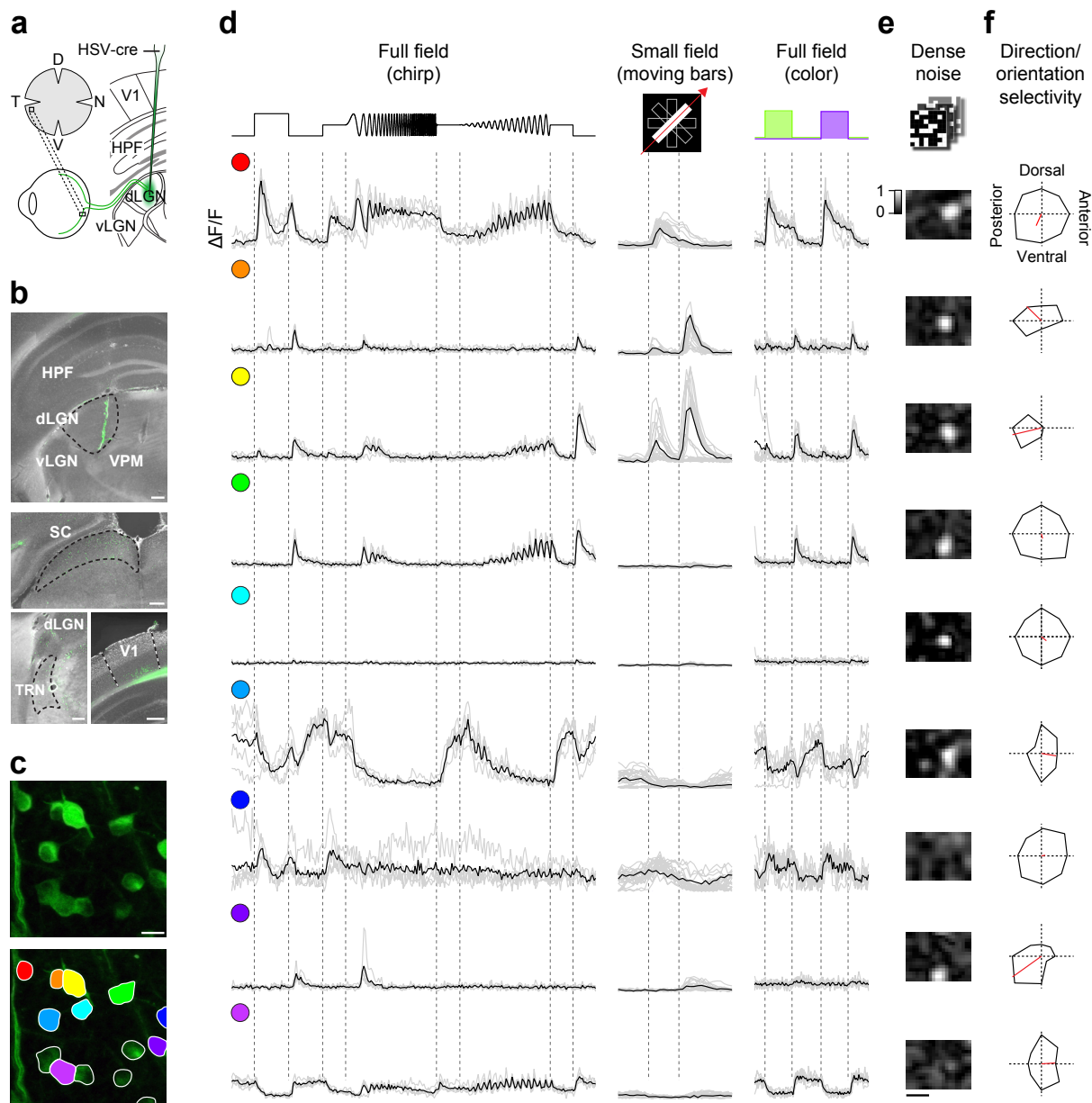


Figure 8 | Functional characterization of dLGN-projecting RGCs. **a**, Schematic of the experimental approach and recording position for field in (c). **b**, Injection of a Cre-encoding retrograde Herpes-Simplex-Virus-1 (LT HSV-hEFlα-cre, Neve & Lim, 2001) into the dLGN (green, GCaMP6f; grey DAPI). Injection site (top) and areas with retrogradely labelled cell bodies (below), and outlines of the dorsolateral geniculate complex (dLGN), superior colliculus (SC), reticular nucleus of the thalamus (TRN) and primary visual cortex (V1) outlined. **c**, Whole-mounted retina of a floxed GCaMP6f mouse transfected with LT HSV-hEFlα-cre and recorded with a two-photon microscope in the ganglion cell layer. Top: Scan field ($110 \times 110 \mu\text{m}$). Bottom: Regions of interest (ROIs) marking cells. **d**, Ca^{2+} responses ($\Delta F/F$) from 9 exemplary ROIs colour-coded in (c) and evoked by three visual stimuli: Full-field chirp, bright bars moving in eight directions, and full-field alternating green/blue. Single trials in grey, averages of $n = 5$ (chirp), 7 (green/blue) or 24 (moving bars) trials in black. Traces are scaled to the maximal value of $\Delta F/F$ for each stimulus separately. **e**, **f**, spatial RFs (e) and polar plots indicating direction and orientation selectivity (f; vector sum in red) for the

same 9 cells as in (d). dLGN, dorsal part of the lateral geniculate nucleus; SC, superior colliculus; TRN, reticular nucleus of the thalamus; V1 primary visual cortex; HPF, hippocampus; vLGN, ventral part of the lateral geniculate complex; VPM, ventral posteromedial nucleus of the thalamus. Scale bars: b, 200 μm ; c, 15 μm ; d, 2 s; e, 200 μm .

4.2 dLGN-p RGCs represent the majority of functional RGC groups

We next asked, which of the previously characterized functional mouse RGC types (Baden et al., 2016) projected to the dLGN. To this end, we used the functional RGC-all clusters obtained from the mouse retina (Baden et al., 2016), and sought to identify, for each retrogradely labelled dLGN-p RGC, the RGC-all cluster with the best matching response properties (Fig. 7a). To account for differences in the Ca^{2+} indicator OGB-1 used by Baden et al. (2016) and GCaMP6f used in the current study, we first de-convolved the Ca^{2+} signals, using the respective Ca^{2+} kernels for the two indicators (Fig. 6). We then correlated, for both the “chirp stimulus” and a moving bar stimulus, the trial-averaged responses of each dLGN-p RGC to the mean response of each RGC-all cluster, and combined the correlation coefficients weighted by a stimulus-specific response quality index (QI) into a “match index”. Intuitively, this match index reflected mainly the correlation for the moving bar stimulus, if the cell responded poorly to the chirp stimulus, and the average correlation, if the cell responded well to both stimuli.

Next, we assigned each dLGN-p RGC to the RGC-all cluster with the highest match index (Fig. 7d). For both individual example cells (Fig. 9a) and across the population of dLGN-p RGCs, the assignment yielded good correlation values (median MI = 0.62 for all individual dLGN-p RGCs). Accordingly, population mean responses of dLGN-p RGCs assigned to the same cluster matched the population mean responses of their respective RGC-all cluster (Fig. 9b; median correlation between cluster means of dLGN-p RGC clusters and their corresponding RGC population clusters of 0.43 (chirp stimulus) and 0.89 (bar stimulus)) (see Fig. 11 and Fig 12 for all dLGN-p RGC clusters and their distribution, respectively).

Next, we determined which RGC types were over- or underrepresented in the dLGN-p RGC population in comparison to the entire RGC population. Following Baden et al. (2016), we grouped the 49 RGC-all clusters into 32 groups, where clusters were merged together, based on functional similarity and available domain knowledge, including morphology, genetic and immunohistochemical labels. Each group thus can be viewed as a unique RGC

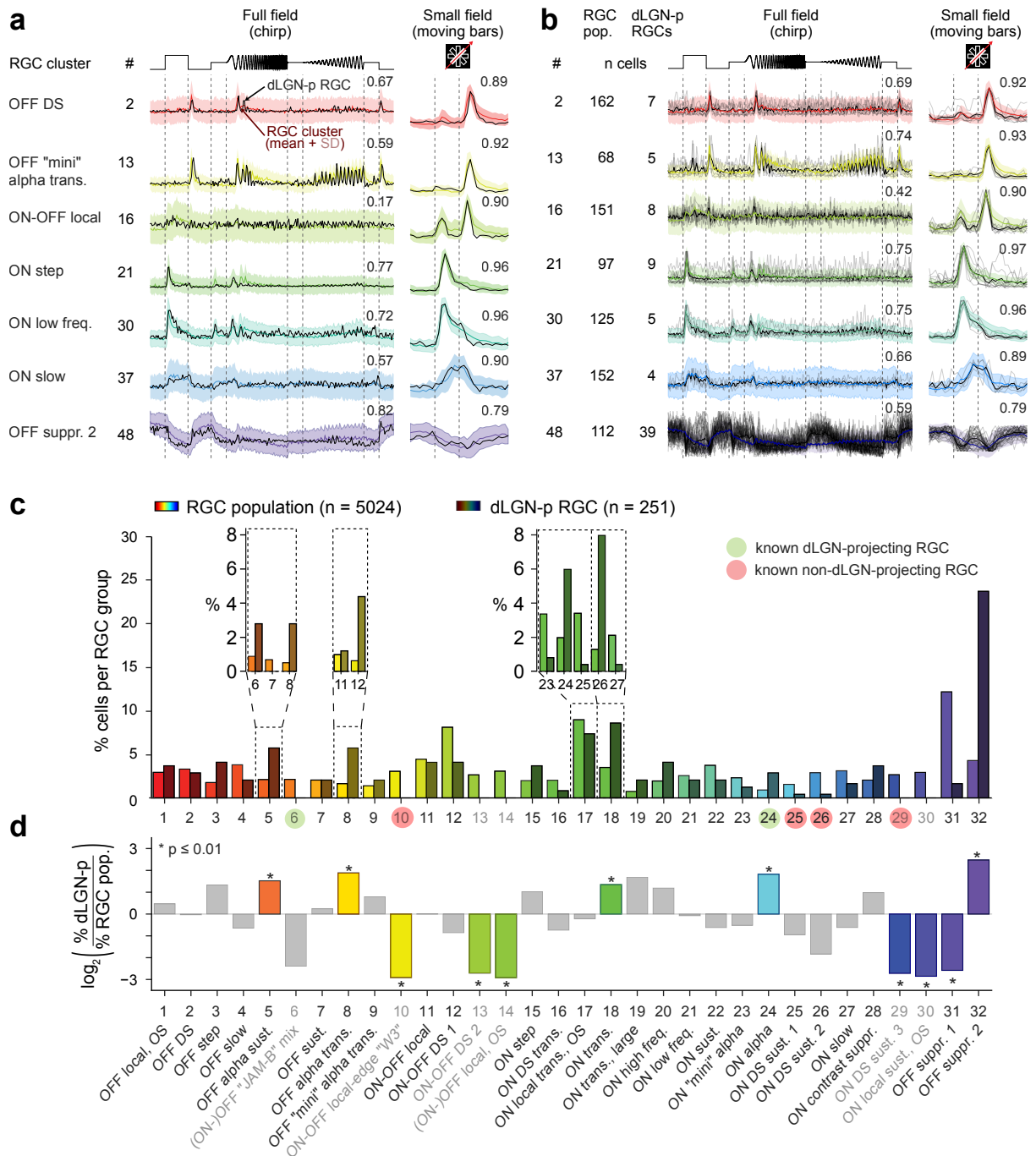


Figure 9 | Cluster assignments. **a**, Responses of selected RGC-all clusters (mean and SD; colour) with mean responses of assigned example dLGN-p RGCs (black) to chirp (left) and bar stimulus (right). Numbers indicate correlation coefficients. **b**, Same, for all assigned dLGN-p RGCs (grey, responses of single dLGN-p RGCs; black, mean). **c**, Left: Distribution of cells per RGC-all group from (Baden et al., 2016) vs. cells per dLGN-p group; insets illustrate subdivision of selected groups into contributing clusters. **d**, Comparison between RGC fractions for dLGN-p RGC groups and RGC-all groups as log₂-ratio (fold change). Significance ($p < 0.01$) is indicated by coloured bars and asterisk.

type (Fig. 9c). We then compared the fraction of cells in each RGC group in the two data sets and found that almost 75% of RGC-all groups had been assigned dLGN-p RGCs (24/32 groups with $n > 1$ cells).

Using a permutation test, we found that specific RGC groups were systematically over- or underrepresented in the dLGN-p population compared to the overall RGC population. The overrepresentation was most striking for the “OFF-suppressed 2” cells (Fig. 9c,d: group 32) and three types of alpha cell (Fig. 9c,d), including OFF alpha sust. (group 5 / clusters 6, 7, 8), OFF alpha trans. (group 8 / clusters 11, 12) and ON alpha (group 24 / cluster 34). Underrepresentation (including absence of some groups), in turn, was strongest for the (ON)-OFF “JAM-B” (group 6 / cluster 9), ON-OFF local-edge “W3” (group 10 / cluster 14), ON-OFF DS 2 (group 13 / cluster 19) and (ON)-OFF local OS (group 14 / cluster 20).

These results seem to be in agreement with the current literature (for more details, see Table 1); in particular, the ON-alpha cells project to dLGN (Ecker et al., 2010; Schmidt et al., 2014), whereas W3 RGCs (Kim et al., 2010) and especially the sustained ON DS RGCs (Dhande et al., 2013; Yonehara et al., 2008, 2009) avoid the dLGN. Surprisingly, among the dLGN-p RGCs, we did not find any JAM-B cells (OFF DS RGCs; Kim et al., 2008), although they have been described as projecting to the dLGN.

Our sample of dLGN-p RGCs contained cells beyond the dataset obtained by Baden et al., (2016). We found cells, which were neither modulated by the chirp nor the bar stimulus, but featured a small and clear RF (Fig. 12). The cell’s small soma size and functional signature shows similarities to an RGC mentioned by Baden et al. (2016). This cell is Pv-positive, lacks responses to both full-field chirp and moving bar stimuli; the latter is the reason why it was excluded from Baden and coworker’s unsupervised clustering analysis.

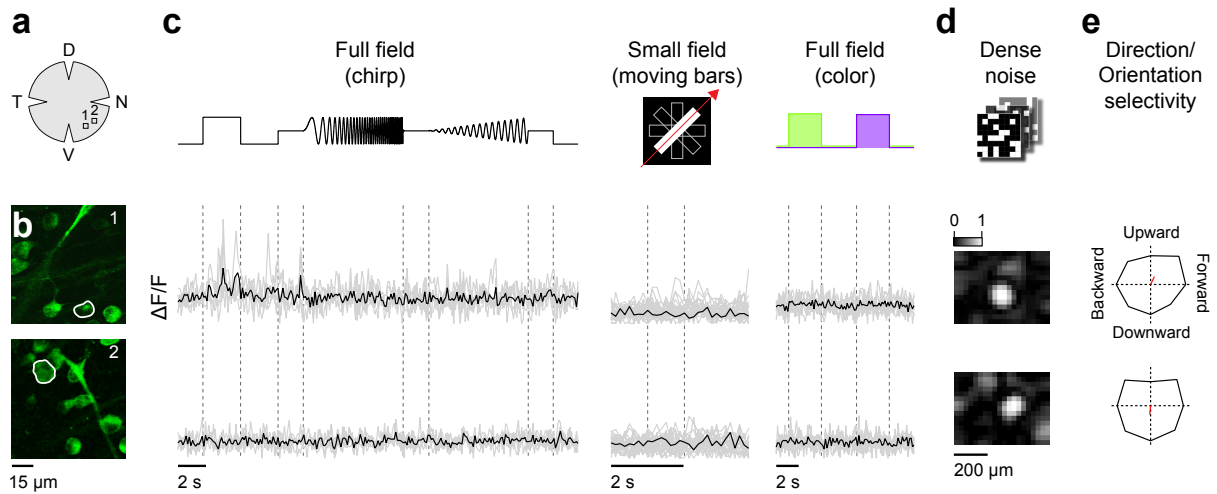


Figure 10 | Some RGCs excluded from further analysis in Baden et al. (2016) form a type of dLGN-projecting cell. **a.** Position of the recording fields with the two example cells. **b.** Outlined are two example cells in a whole-mounted retina of a floxed GCaMP6f mouse, which was transfected with LT HSV-hEFla-cre, and recorded with a two-photon microscope in the ganglion cell layer. The numbers correspond to the respective recording field, shown in a. **c.** Ca^{2+} responses ($\Delta F/F$) of the cells in (b) to three visual stimuli: Full-field chirp, bright bars moving in eight angular directions, and full-field alternating green/blue stimulus. Single trials in grey, averages of $n = 5$ (chirp), 7 (green/blue) or 24 (moving bars) trials in black. Traces are scaled to the maximal value of $\Delta F/F$ for each stimulus separately. **d, e.** spatial RFs (d) and polar plots indicating direction and orientation selectivity (e; vector sum in red) for the cells in (b).

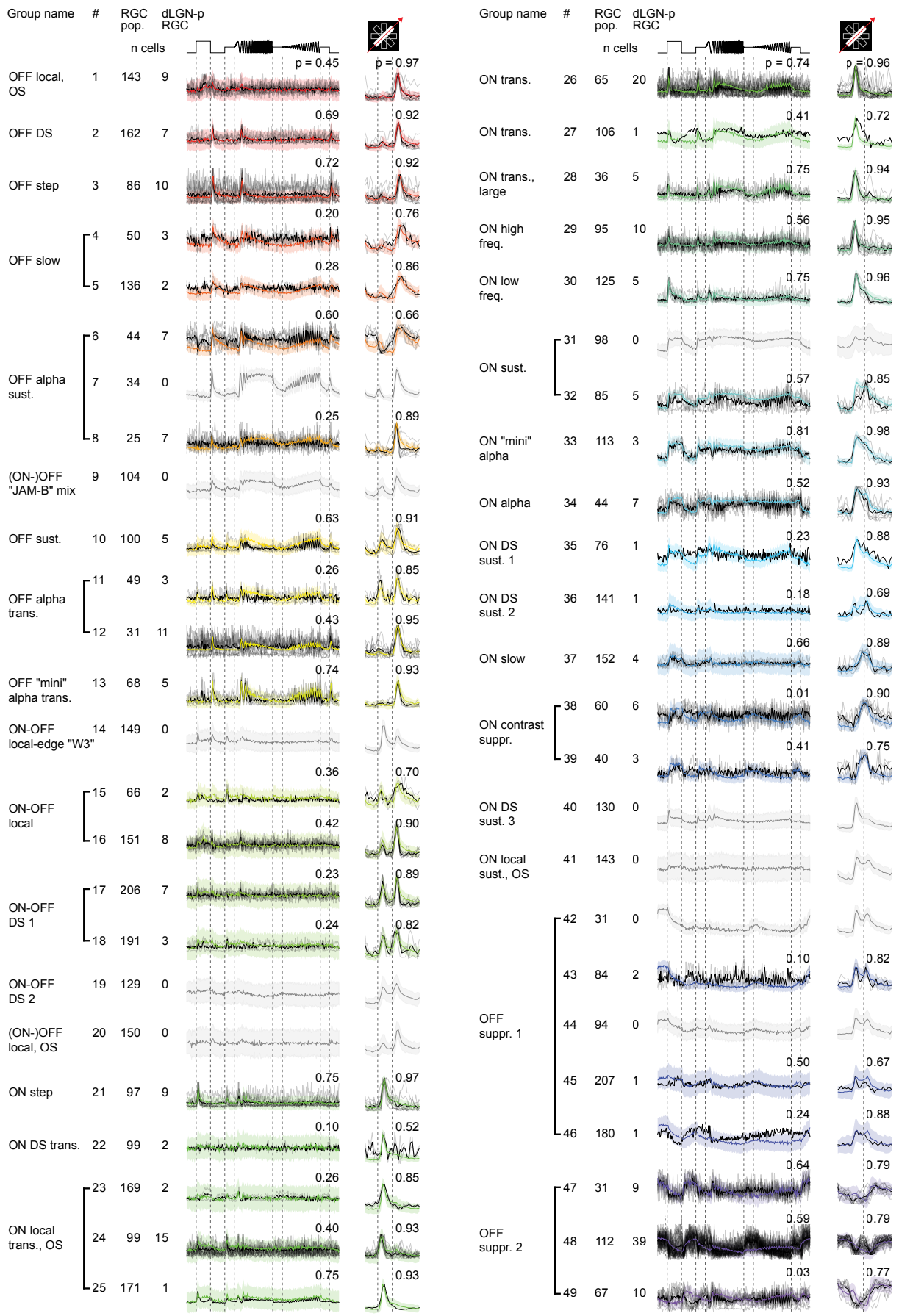


Figure 11 | dLGN-p RGC cluster assignments. All dLGN-p RGC cluster responses (grey: individual RGCs; black: cluster mean), along with assigned RGC-all cluster response mean (colour) and SD (coloured area). RGC-all clusters that were not assigned any dLGN-p RGCs are greyed out.

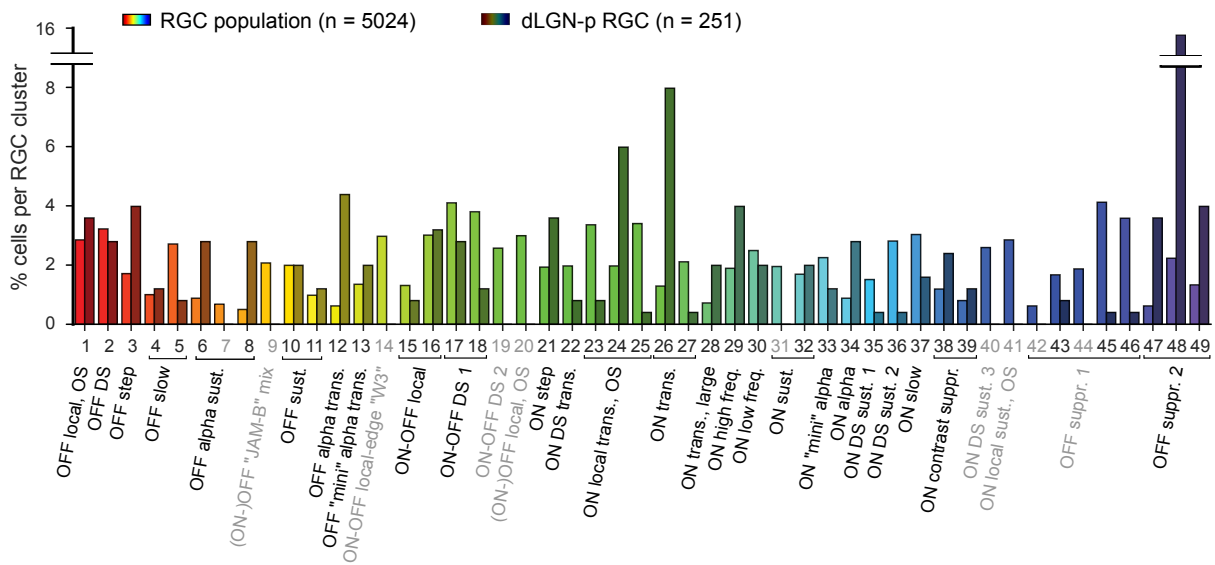


Figure 12 | Distribution of dLGN-p RGC cluster. Percentage of cells per RGC cluster for dLGN-p RGCs (dark colours) and all RGCs obtained from Baden et al., (2016) (saturated colours).

name	dLGN projections	transgenic line or marker	group*	cluster*	function	reference
JAM-B, OFF DS	yes	JAM-B-CreER	6	9	DS, upward	(Kim et al., 2008, 2010)
ON-OFF DS 1, 2	yes	FSTL4-CreER	12, 13	17, 18, 19	DS, down-, upward	(Kay et al., 2011; Kim et al., 2010)
ON-OFF DS 1, 2	yes	Drd4-GFP	12, 13	17, 18, 19	DS, backward	(Huberman et al., 2009; Kay et al., 2011)
ON-OFF DS 1, 2	yes	TRHR-GFP	12, 13	17, 18, 19	DS, backward	(Rivlin-Etzion et al., 2011)
OFF-alpha	yes	CB2-GFP	5, 8	6, 7, 8, 11, 12	centre-surround	(Huberman et al., 2008)
ON-alpha	yes	Opn4-Cre	24	34	centre-surround, ipRGC	(Ecker et al., 2010; Estevez et al., 2012; Schmidt et al., 2014)
F-RGC	yes	Foxp2				(Rousso et al., 2016)
W3	no	TYW3	10	14	feature detector	(Kim et al., 2010; Zhang et al., 2012)
OFF Alpha sust.	no	TYW7	5	6, 7, 8	centre-surround	(Kim et al., 2010)
ON DS sust. 1	no	Hoxd10-GFP	25	35	DS, forward	(Dhande et al., 2013)
ON DS sust. 2	no	Hoxd10-GFP, Spig1-GFP	26, 29	36, 40	DS, down-, upward	(Dhande et al., 2013; Yonehara et al., 2008, 2009)
ON DS sust. 3	no	Hoxd10-GFP, Spig1-GFP	26, 29	36, 40	DS, down-, upward	(Dhande et al., 2013; Yonehara et al., 2008, 2009)
ON-OFF DS 1, 2	no	Hoxd10-GFP	12, 13	17, 18, 19	DS, forward	(Dhande et al., 2013)

Table 1. Table showing putative correspondences between dLGN-p RGCs and previously characterized RGC types from recent surveys of mouse retinal ganglion cells. *cluster and group indices refer the functional classification by Baden et al. (2016)

4.3 dLGN neurons encode diverse visual features

Having found most functional RGC groups providing input to mouse dLGN, we next wondered how this diversity is reflected in the dLGN population response. We performed extracellular single-unit recordings of geniculate neurons in head-fixed mice (Fig. 13a, 15a). We verified the recording sites to be in the dLGN by histological reconstruction of the electrode tract (Fig. 13b) and the characteristic progression of retinotopy along the electrode channels (Fig. 13c) (Piscopo et al., 2013). We presented the same chirp stimulus as in the retina experiments. To assess the stability of the dLGN recordings and the consistency of our spike sorting, we flanked the chirp stimulus by presentations of drifting gratings with varying orientation, temporal and spatial frequency in a subset of the experiments (for 443 of 815 units, Fig. 14).

Responses of dLGN neurons to the chirp stimulus were surprisingly diverse: The cells not only displayed the “standard” transient and sustained ON/OFF responses, or were suppressed by contrast, but also differed in their temporal frequency or contrast preferences (Fig. 13d) as well as their response kinetics. Some of the cells even displayed slow ramping responses (Fig. 13d₄, d₅). To ensure that this response diversity did not result from poor unit isolation during spike sorting, we considered only units with a firing rate > 1 spike/s that, in addition, were stable across time, had a clean refractory period, and a distinct extracellular spike waveform (Fig. 13e, f).

Besides this rich representation of luminance steps, temporal frequency chirps and changes in contrast in the overall dLGN population, 82/443 (18.5%) dLGN neurons only displayed weakly modulated responses to the chirp stimulus (Fig. 14b₂, b₃) despite having robust and consistent responses to the drifting gratings presented before and afterwards (Fig. 14). This combination of response patterns is consistent with these dLGN neurons preferring local variations in luminance instead of full-field uniform patterns, as has been suggested for several RGC groups (Baden et al., 2016). Together, our analysis of dLGN responses indicate that the response diversity observed at the level of dLGN-p RGCs can also be encountered at the level of the visual sensory thalamus.

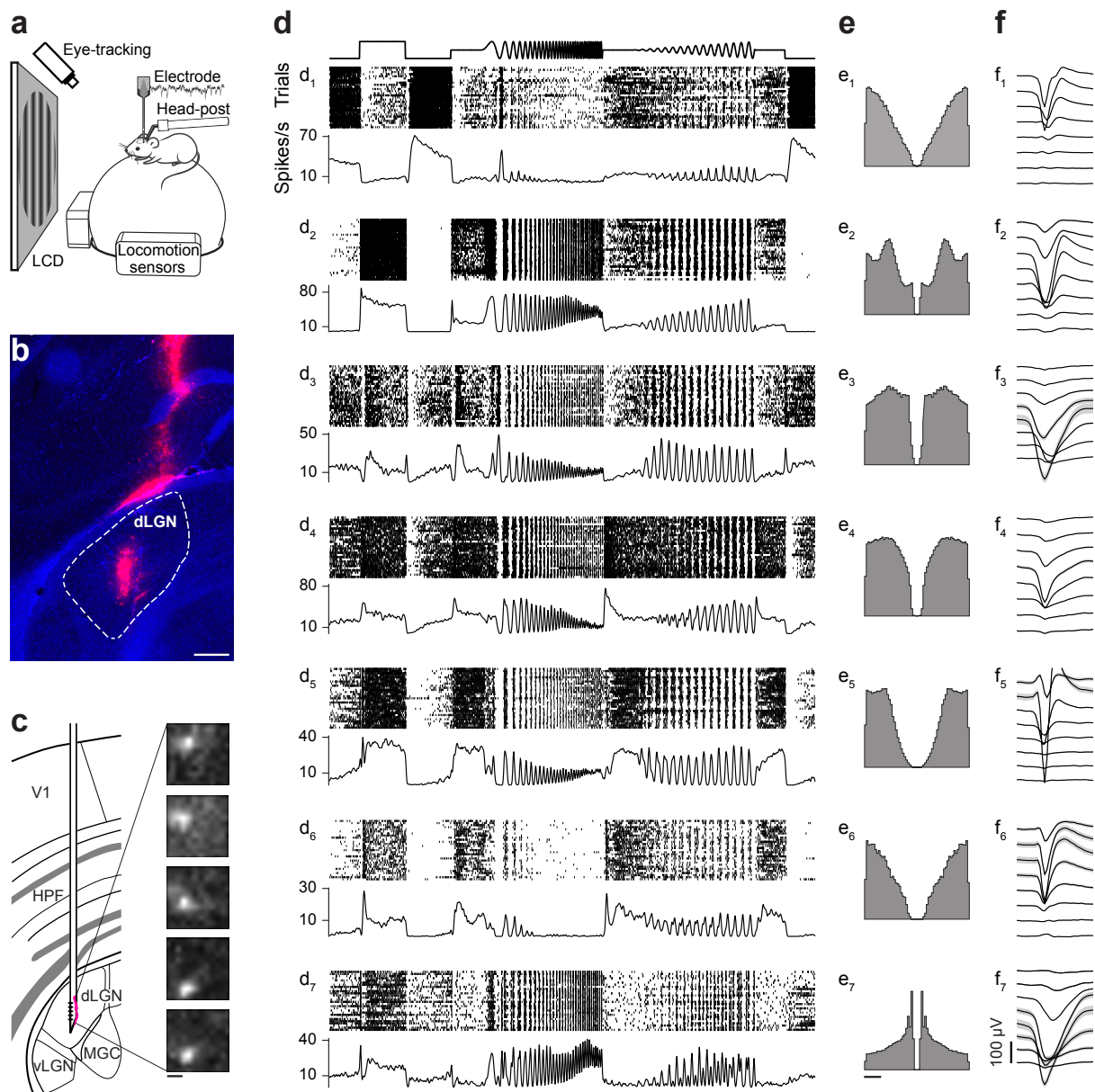


Figure 13 | Functional characterization of dLGN neurons. **a**, Schematic of the recording setup for extracellular dLGN recordings. **b**, Reconstruction of the electrode track in dLGN (coronal section; dLGN is marked by white outline, Blue: DAPI, Red: DiD coating the electrode). **c**, Schematic of recording site with RFs mapped for several electrode channels (dorsal to ventral), showing the retinotopic progression in elevation typical of mouse dLGN. **d-f**, Spike raster plots (top) and spike density function (bottom) of 7 example dLGN neurons in response to the chirp stimulus (d), their autocorrelograms (f), and spike waveforms in selected 5 channels of the 32-channel probe (f). V1, primary visual cortex; HPF, hippocampus; dLGN, dorsal part of the lateral geniculate nucleus; vLGN, ventral part of the lateral geniculate nucleus; MGC, medial geniculate complex. Scale bars: b, 200 μm ; c, 10 deg; d, 5 s; e, 10 ms; f, 0.5 s.

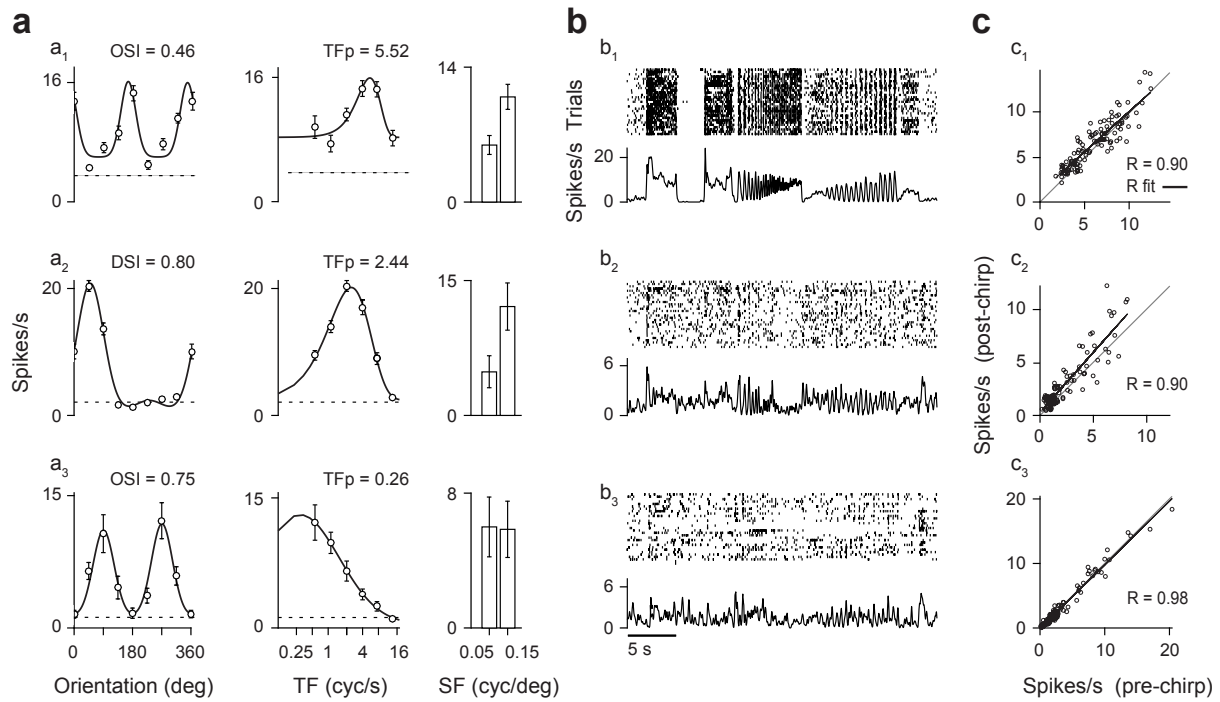


Figure 14 | dLGN responses to drifting gratings. (a-c). Responses of three example dLGN cells to drifting gratings. **a.** Mean firing rates and fitted tuning curves (red) for orientation, spatial frequency, and temporal frequency. **b.** Responses to the chirp stimulus. **c.** Scatter plot of average firing rates across all conditions of the drifting grating stimuli presented before and after the chirp stimulus, used to determine the stability of the recorded cells. $R > 0.65$ indicates that a dLGN responded well to both STFO stimuli, thus stayed stable over time. Abbreviations: OSI, orientation selectivity index; DSI, direction selectivity index; TF, temporal frequency; SF, spatial frequency; TFP, preferred temporal frequency

4.4 Decomposing dLGN responses into diverse functional components

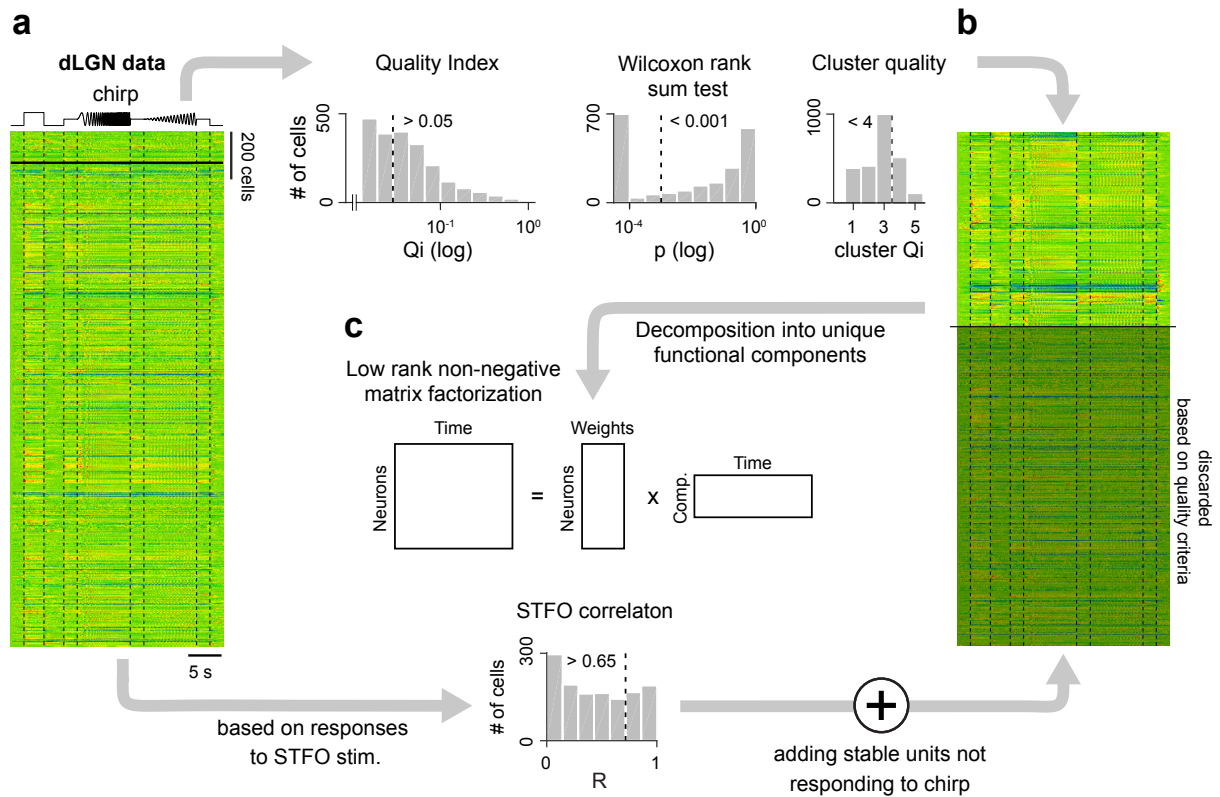


Figure 15 | Overview of analysis steps for the decomposition of dLGN responses into unique functional components. **a.** Heat maps of dLGN responses to the chirp stimulus. Each line represents a single cell response with activity colour-coded such that warmer colours illustrate increased activity. **b.** Heat maps of sorted dLGN responses ($n = 815$) and discarded "units" that did not pass the quality criteria (top, bottom; see methods) ($n = 2191$). **c.** Schematics of the low-rank non-negative matrix factorization, which was applied on data from (b).

To more quantitatively assess the degree of diversity present in dLGN neurons, we used sparse non-negative matrix factorization (NNMF) to decompose the population response to the chirp stimulus into “response components”, which, weighted appropriately and summed, can be used to represent the responses of individual neurons (Fig. 15c, Fig. 16a) (Nikolaus & Paper, 2007). Comparing the residual error of the NNMF of the actual data to that of randomly permuted data (Frigyesi & Höglund, 2008), we found that 25 components optimally reconstructed the population responses (Fig. 16b). Consistent with the ability of the NNMF to extract visual response components resembling true parts-based representations, some of the NNMF components resembled the responses of individual RGC groups (Fig. 17). Generally, the NNMF components contained a rich set of sustained or transient ON and OFF representations with diverse preferences for different temporal frequencies and contrasts (Fig. 16c). Zooming into the components during the frequency part of the chirp stimulus illustrates that NNMF components, like dLGN neurons, differ not only overall temporal frequency preference but also in the phase of their responses (Fig. 16d)

We next investigated how many components were needed to reconstruct the responses of single dLGN neurons. We found that the number of components with weights > 0 varied widely across dLGN neurons between 2 and 24 (Fig. 16e). In general, a single dLGN neuron could be reconstructed using an average of 16 elementary response components with weights > 0 . We illustrate the results of our decomposition approach with NNMF in three example dLGN neurons. Reconstructions of dLGN neurons with a smaller number of components were composed of a few dominant and several auxiliary components (Fig. 16f, top), whereas more complex reconstructions contained a combination of components with high and low weights (Fig. 16f, middle, bottom).

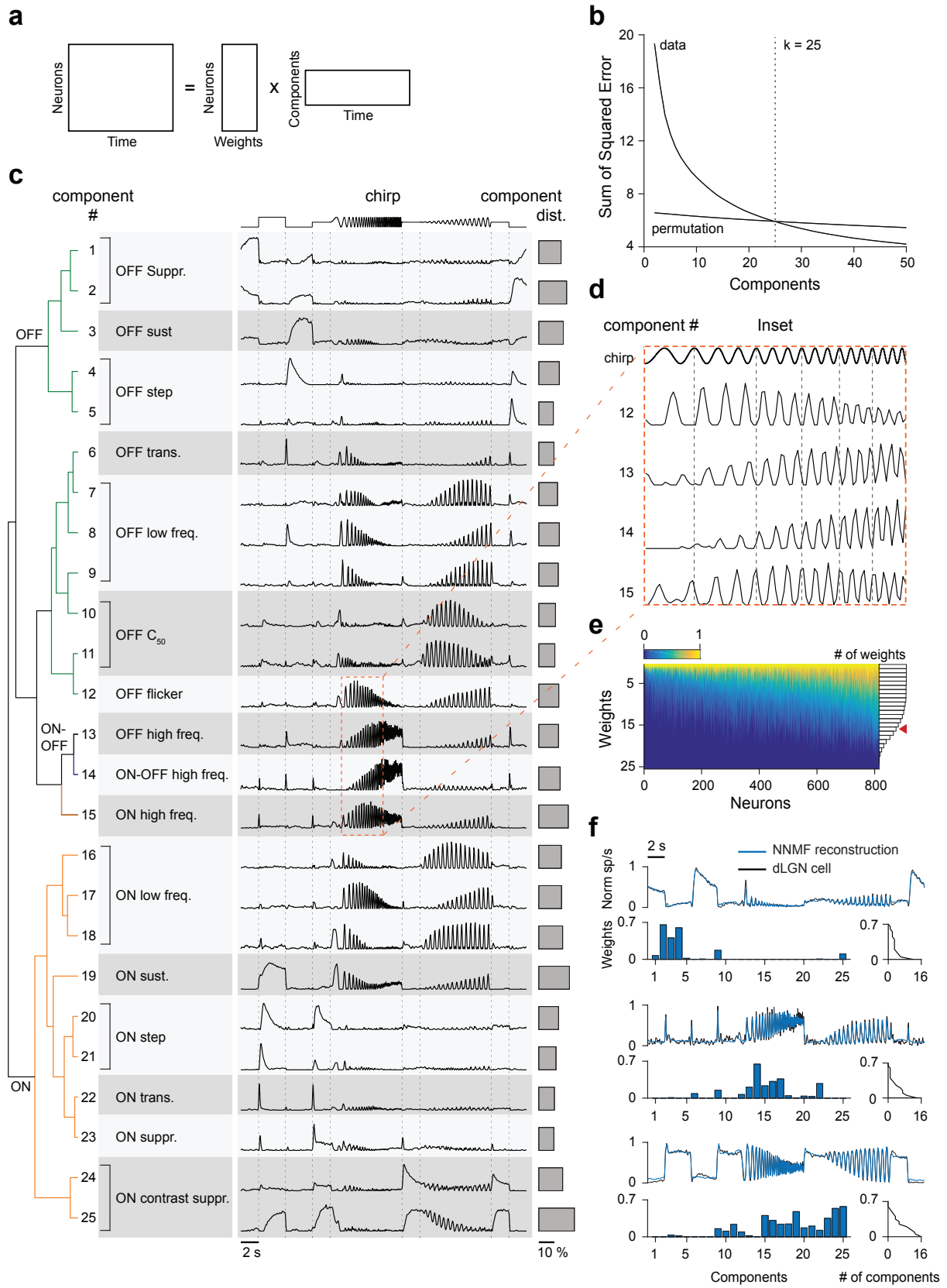


Figure 16 | Decomposition of the dLGN population response. **a**, Schematic of the low-rank non-negative matrix factorization. **b**, Estimating the number of components based on an optimal ratio between noise reduction and information preservation. **c**, dLGN response components as computed by the NMF algorithm (centre) and organized according to a hierarchical cluster tree with an optimized leaf order (left). Right: Percentage of neurons containing the respective response component. **d**, Four example components during the frequency part of the chirp stimulus at an expanded temporal scale. **e**, Left: Normalized component weights, sorted for each neuron in decreasing order. Right: Distribution of the number of weights. The mean is indicated by the red triangle. **f**, Top: Examples of dLGN cell responses (black) and their NNMF reconstruction (blue). Bottom: Weights used for reconstruction as a function of component id (left) and sorted in descending order (right).

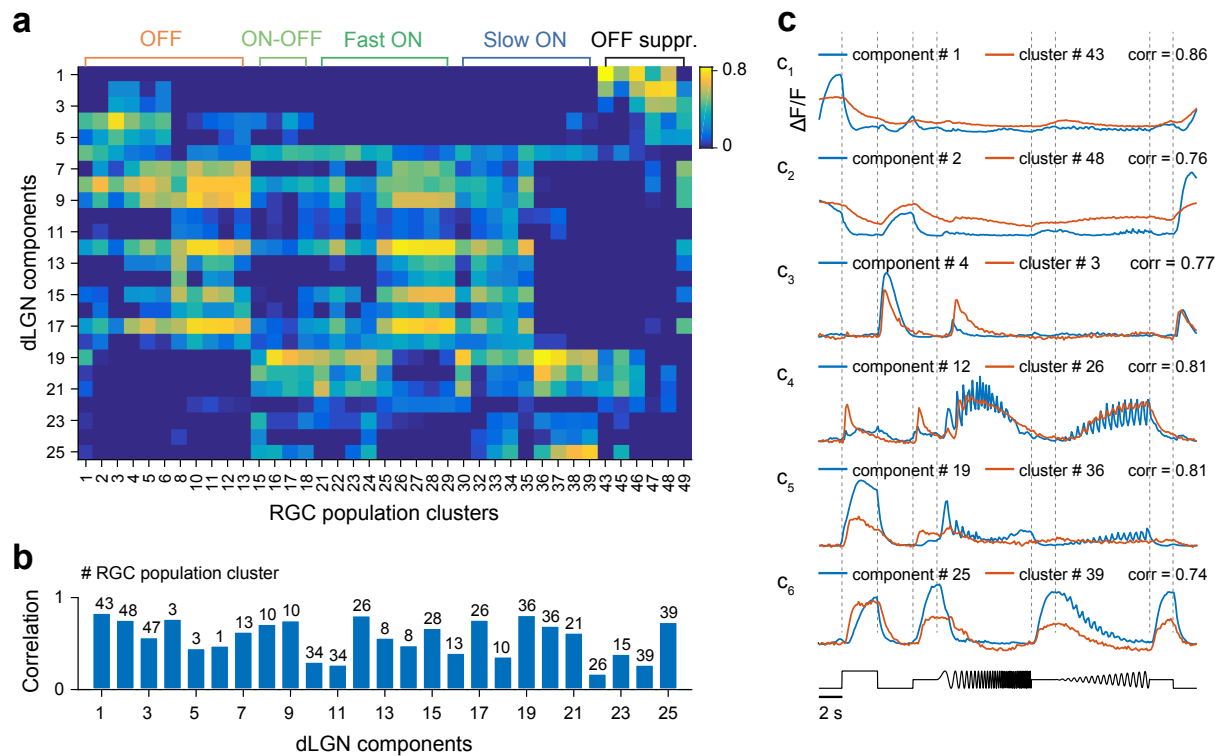


Figure 17 | Correlating dLGN response components with RGC population clusters. **a**, Correlation matrix was computed by correlating dLGN response components, which were convolved with an artificial calcium kernel, with RGC population clusters. **b**, dLGN components with their best correlated RGC population cluster. The number above the bar indicates the respective RGC population cluster. **c**, Example dLGN response components with their best matching RGC population cluster response.

4.5 dLGN responses can be modelled as a sparse linear combination of inputs from RGC types

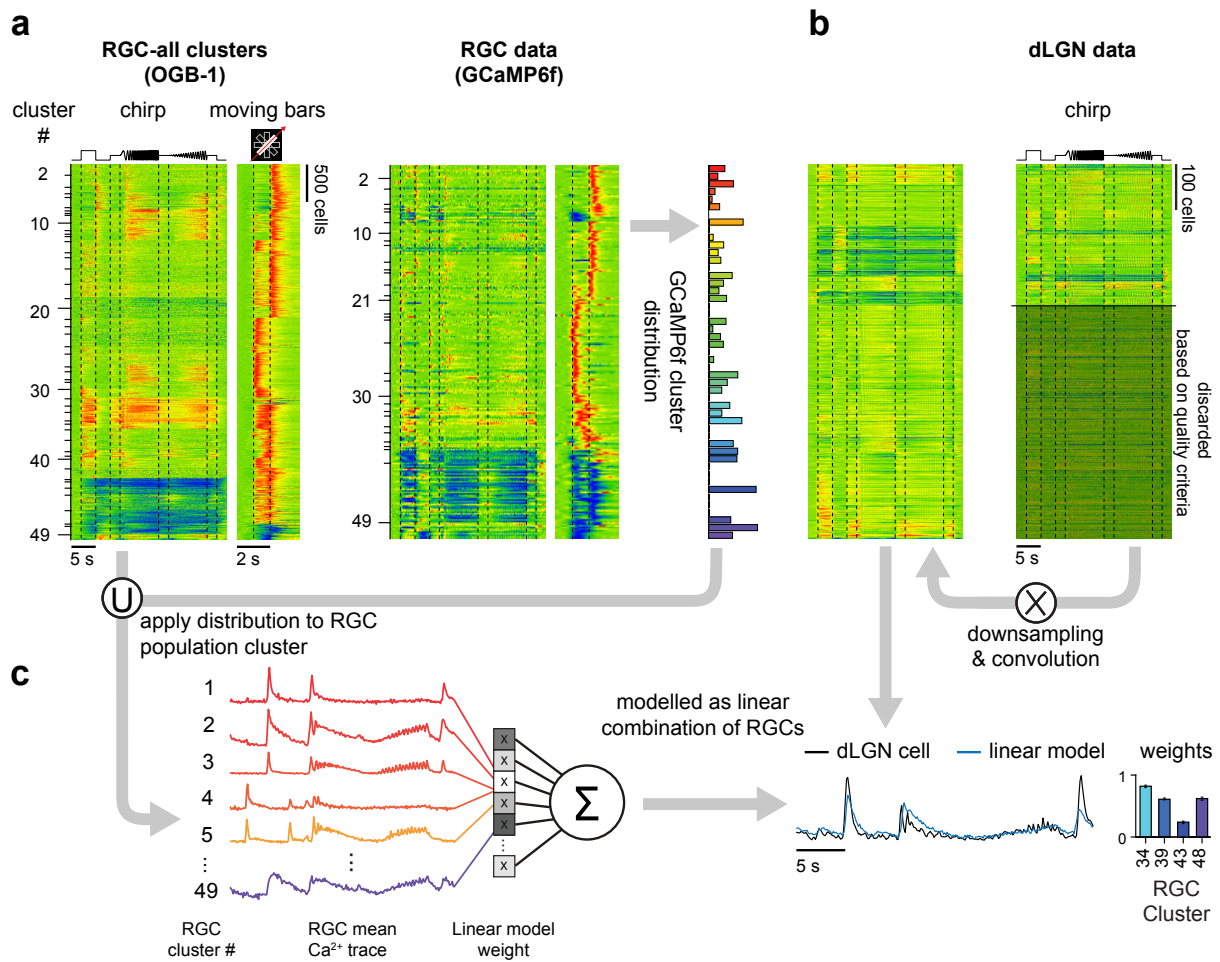


Figure 18 | Overview of analysis steps for the modelling of dLGN responses as a sparse linear combination of RGC inputs. **a.** Left: Heat maps of Ca^{2+} RGC-all cluster responses to the chimp and the bar stimulus ($n = 49$ RGC cluster, Baden et al., 2016). Each line represents responses of a single cell with activity colour-coded such that warmer colours represent increased activity, and the cluster height indicates the number of included cells. Middle: Heat maps of GCaMP6f dLGN-p RGCs, assigned to RGC-all cluster. Right: Distribution of dLGN-p RGCs, based on the GCaMP6f cell assignment to RGC-all clusters. RGC-all groups are color-coded. **b.** Right: Heat maps of sorted dLGN responses ($n = 815$) and discarded cells that did not pass quality criteria ($n = 2191$). Left: Heat map of dLGN responses, which were down-sampled and convolved with a mean OGB-1 indicator kernel to match the RGC properties. **c.** Left: Illustration of the linear model. The model uses a linear combination of weighted mean RGC-all cluster responses, based on the GCaMP6f distribution, to predict the response of a dLGN neuron. Right: Exemplary dLGN response and its linear prediction. Model weights are color-coded by RGC-all clusters.

Next, we combined the dLGN-p RGC dataset and the dLGN dataset to study how the dLGN responses are computed from the retinal output channels (Fig. 18). We first accounted for the differences in recording method (Ca^{2+} imaging vs. extracellularly recorded spikes) by convolving the dLGN spiking responses with a Ca^{2+} indicator kernel. We then used a linear model constraint to have non-negative weights to predict dLGN responses as a sum of weighted RGC inputs (Fig. 5a, supp. Fig. 1j). For prediction, we used RGC-all cluster means (Baden et al., 2016), which were assigned at least one dLGN-p cell. Prediction quality was determined on 50% of trials not used for fitting the weights, using repeated random sub-sampling validation with 1000 repetitions. The reported weights represent mean values across the repeats.

This simple linear excitatory feed-forward model successfully reconstructed different response types of dLGN neurons, including transient ON, sustained ON and OFF, and suppressed cells (Fig. 19b,c; median correlation: 0.64, median RMSE: 0.17). We illustrate the results of our modelling in five example dLGN neurons. In three dLGN neurons, the responses were predicted using only a few non-zero weights, containing either a combination of one dominant and few weak weights (Fig. 19d₁) or a combination of several dominant and few weak weights (Fig. 19d_{2,3}), reminiscent of anatomical findings (Rompani et al., 2017). Two out of five neurons could be modelled by a higher (>10) variety of possible RGC-all cluster combinations (Fig. 19d_{4,5}), however, with only a few dominant and many weak weights. Across the population the responses of dLGN neurons ($n = 814$) could be predicted by the weighted input of 3-7 RGCs (Fig. 19b₃), with an average input of ~5 RGC types (mean = 5.35, median = 5.19). Together, these results indicate that the responses of many dLGN neurons, at least on a temporal scale of calcium transients, can be explained by excitatory feed-forward processing.

Finally, we explored in the model which dLGN-p RGC clusters were used for prediction. We found that the majority (33/49) of previously identified dLGN-p RGC cluster were used in the functional modelling of dLGN responses (Fig. 5g). While some clusters contributed to the functional response of dLGN neurons more frequently than others, six of these clusters contributed to the response of more than 50% of dLGN cells, and showed in addition the highest mean weight across modelled dLGN cells. Interestingly, three out of these six dLGN-p RGC clusters were the cell types that were significantly overrepresented in the dLGN-p RGCs (see Fig. 9), although information about the relative frequency of the projections was not used for inference in the model. Our modelling approach thus suggests that these cell types have a significant functional role in the processing of visual information along the retinogeniculate pathway.

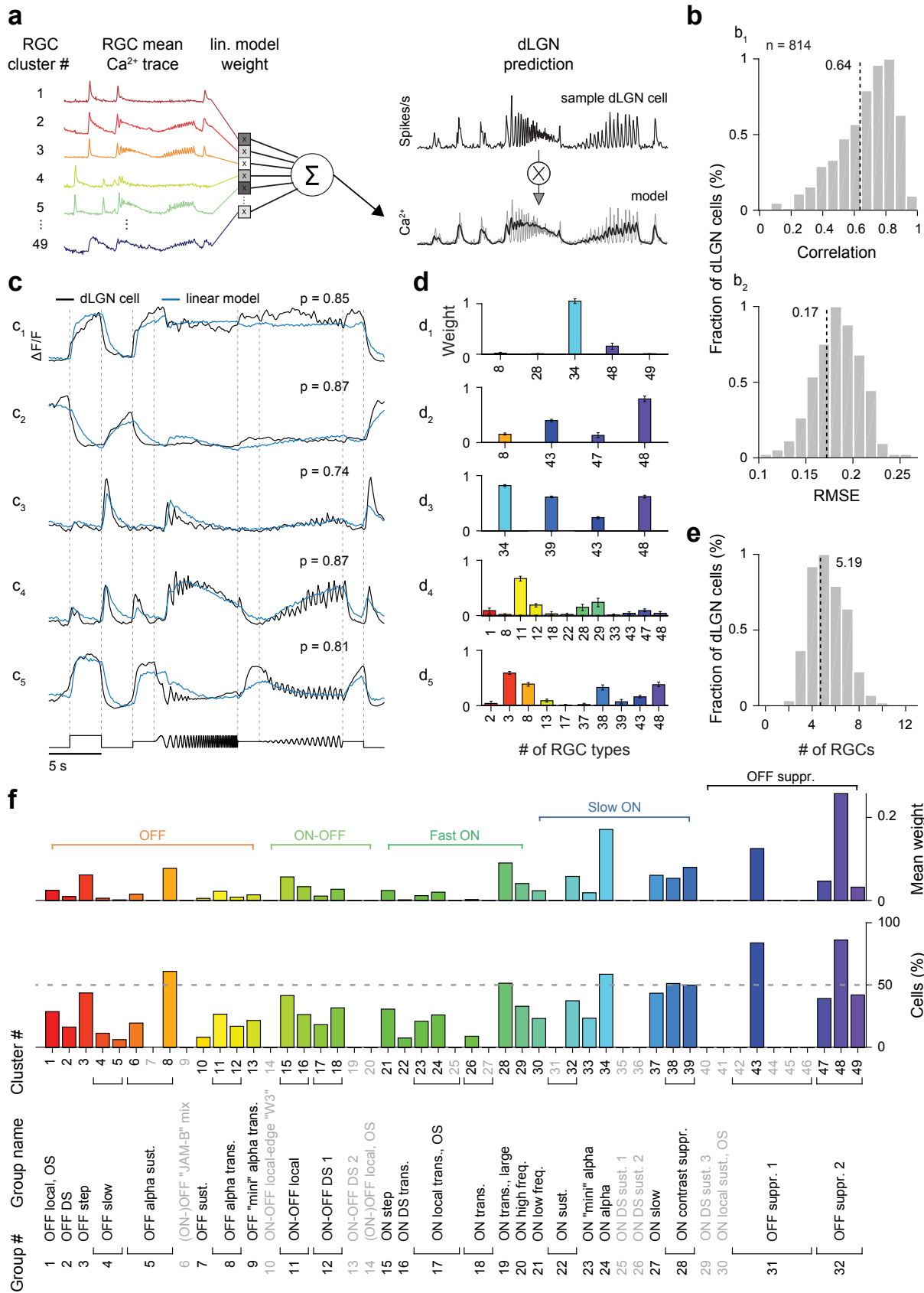


Figure 19 | Functional modelling of retinogeniculate convergence. **a.** Illustration of the linear model. The model predicts a Ca^{2+} -kernel convolved response of a dLGN neuron as a linear combination of weighted RGC-all cluster inputs. **b.** Correlation (b_1) and root mean square error (b_2) (RMSE) between the convolved responses of dLGN neurons and their linear predictions. **c.** Left: Example responses of convolved dLGN neurons (black) and predictions by the linear model (blue). **d.** Fitted weights as a function of RGC-all cluster number. **e.** Number of RGC-all cluster inputs converging onto one dLGN neuron, as predicted by the linear model. **f.** Top: Mean weight distribution of RGC-all cluster across dLGN neurons. Bottom: Percentage of cells, for which the RGC-all cluster were used to model the prediction, e.g. cluster 48 was applied in the modelling of approx. 85% of all dLGN neurons. RGC-all clusters not projecting to dLGN are greyed-out.

5 Discussion

We functionally characterized the population of dLGN-projecting RGCs and geniculate neurons, and provide a quantitative account of the functional connectivity between RGC types and dLGN neurons. We present three main findings. First, combining a retrograde viral transfection approach and two-photon Ca^{2+} imaging of RGC responses to obtain functional properties of RGCs, we show that dLGN-p RGCs include the majority of previously functionally identified RGC types. Second, decomposing dLGN responses into their elementary response components revealed a rich functional diversity of geniculate visual representations, reminiscent to that of RGCs. Third, we demonstrate that the responses of individual dLGN cells can be modelled as weighted linear combinations of responses of mostly 3-7 RGC types. Assuming that each type can mediate its input via several individual RGCs (Rompani et al., 2017), these estimates of functional connectivity are greater than most previous findings in mice, cats, and monkey (Chen & Regehr, 2000; Litvina & Chen, 2017b; Sincich et al., 2007; Usrey et al., 1999), and resonate well with recent anatomical estimates based mono-transsynaptic rabies virus tracing (Rompani et al., 2017).

5.1 Functional classification of dLGN-projecting RGCs

Retrograde viral tracing with HSV-cre, combined with two-photon Ca^{2+} imaging, provides an ideal method for measuring functional properties of dLGN-p RGCs. The advantage of HSV is the strictly synaptic uptake mechanism of the HSV (Antinone & Smith, 2010; McGavern & Kang, 2011), preventing infection of axons passing nearby and not synapsing within the dLGN, as it is known to occur for commonly used retrograde tracers, such as DiO/Dil, horseradish peroxidase, fluorophore-conjugated latex microspheres or cholera toxin (Ellis et al., 2016). In addition, our observation that GCaMP6f expression in the retina was limited to spatially confined regions is consistent with the interpretation that HSV infected neurons were restricted to the retinotopically corresponding region in dLGN instead of labelling RGC axons of passage, which would likely result in a large spread of RGC receptive field locations.

Earlier studies reported various numbers of dLGN-p RGCs across different species: In primates ~90% of RGCs project to the dLGN (Perry & Cowey, 1984), whereas in cats ~75% of RGCs (Illing & Wässle, 1981) and in the rat less than 50% of RGCs form retinogeniculate connections (Dreher et al., 1985; Linden & Perry, 1983; Martin, 1986). Matching our functional RGC responses to the previously defined functional RGC types (RGC-all groups)

allowed us to assess the total fraction of dLGN-p RGCs in a mouse. We estimated that ~60% of all RGCs project to the dLGN, which is in a very close proximity to the results obtained from rat tracing studies. Unsurprisingly, our results suggest a similar distribution of dLGN-p RGCs in a rat and a mouse.

Baden and colleagues (2016) provided in their study putative correspondences between some of their functional RGC groups and RGC types from recent surveys of mouse RGCs (Dhande et al., 2013; Huberman et al., 2009; Rivlin-Etzion et al., 2011; Sümbül et al., 2014; Völgyi et al., 2009), based on functional properties and additional domain knowledge, including morphology, genetic and immunohistochemical labels. Based on these correspondences, we were able to link some of our functionally identified dLGN-p RGC types to previous data on dLGN projections of different RGC types (for details, see supp. Table 1). Our results are consistent with earlier studies showing that the ON-alpha cells form synaptic connections with neurons in the dLGN (Ecker et al., 2010; Schmidt et al., 2014), while W3 RGCs (Kim et al., 2010) and the sustained ON DS RGCs (Dhande et al., 2013; Yonehara et al., 2008, 2009) avoid the dLGN. Surprisingly, among our sample of dLGN-p RGCs, we did not find any JAM-B cells (OFF DS RGC; Kim et al., 2008), although they are known to project to dLGN. This may either be due to our relatively small dLGN-p RGC dataset, or, more likely, a misidentification of JAM-B cells in Baden et al. 2016, which were included in a putative “mixed” cluster, because the JAM-B (G6) was predicted to stratify mainly below the ChAT band, while the cell is known to stratify above it (Kim et al., 2008).

In comparison to the overall RGC distribution in the mouse retina, several of the dLGN-p RGC types showed a profound overrepresentation, in particular, three of the alpha RGC types (Krieger et al., 2017; Van Wyk et al., 2009) and the OFF suppressed cells (Tien et al., 2015). Alpha RGCs have been described in all mammalian species studied so far (reviewed in Berson, 2008; Krieger et al., 2017). They share certain physiological properties, such as a high sensitivity to changes in their RF, short response latency and fast conducting axons and are thereby among the first retinal output channels, signalling “new stimuli” to the dLGN (Krieger et al., 2017; Pang et al., 2003; Van Wyk et al., 2009). Hence, alpha RGCs may encode fast changes in the visual signal such as the high frequency component of the chirp stimulus and feed this information to dLGN. We indeed observed three such response components in the dLGN, based on our NNMF approach, which suggests that alpha RGCs best suitable candidates to encode this type of information and provide it to dLGN. OFF suppressed RGCs, also referred to as Suppressed-by-Contrast (SbC-) RGCs, exhibit a high baseline firing rate which is suppressed by light stimulation and are also thought to be conserved across mammals (e.g. de Monasterio, 1978; Rodieck, 1967; Sivyer, Taylor, &

Vaney, 2010; Tien, Pearson, Heller, Demas, & Kerschensteiner, 2015). SbC-like responses have also been recorded along all stations of the mouse retino-geniculo-cortical pathway (Niell & Stryker, 2010; Piscopo et al., 2013; Tien et al., 2015), suggesting a dedicated early visual pathway. It has been proposed that SbC-RGCs signal uniformity of the visual field (Levick, 1967; Masland & Martin, 2007; Sivyer et al., 2010), control contrast gain (Troy et al., 1989), or signal self-generated visual stimuli, contributing to central processing of blinks and saccades (Tien et al., 2015). The higher abundance of these cell types could be explained by unequal labelling of different RGC types by the HSV. However, we know of no evidence that could either confirm or dispute the idea that HSV has higher affinity for certain cell types.

During the classification of dLGN-p RGCs, we discovered cells (Fig. 10), which were not included in the Baden et al. (2016) dataset. With a soma size of $< 15 \mu\text{m}$, small and crisp RF but otherwise no functional signature, they seem strikingly similar to the Pv-positive RGCs that lacked responses to both full-field chirp and moving bar stimuli, and therefore, was not used in their unsupervised clustering analysis. Recently, four “new” dLGN-p RGC types have been described; these RGCs can be selectively identified by their expression of transcription factor *Foxp2* (Rousso et al., 2016). One of these types, the so-called F-mini cells, have small somata and small RFs, reminiscent of the aforementioned small cells in our dLGN-p RGC sample. In contrast to the functional properties of these cells under our stimulus conditions, Rousso et al. (2016) described F-mini cells as direction-selective; this apparent mismatch, however, may be due to differences in stimulus size and velocity used in the two studies. Taken together, it is well possible that the F-mini RGCs correspond to the small cells in our dataset. To establish this connection, however, would require further recordings with stimuli similar to those used by Rousso et al. (2016).

Our results represent a conservative minimum of unique functional dLGN-p RGC types found in the mouse retina, because some of the RGC types can probably not be resolved with our standardized but with only 4 stimuli rather limited stimulus set. This stimulus set was used in the functional classification survey of RGCs in Baden et al. (2016). Therefore, cell types that were not modulated or could not be resolved by the stimuli in , were also not included in our survey of dLGN-p RGCs. For instance, ipRGCs were largely discarded from the clustering analysis used by Baden and colleagues (2016), because they either did not respond well to the stimulus set and thus failed the quality criterion, or were sorted into different RGC groups and thus did not comprise a dedicated ipRGC channel (Baden et al., 2016). Furthermore, at least one PV-positive small-field RGC type was not included, because of its unresponsiveness to the chirp and the bar stimulus (for details, see paragraph above).

5.2 Components of the dLGN population response

Consistent with its rich retinal input, we found that the dLGN population response can be captured by 25 different components. The high number of components is in contrast to the classical notion of three parallel retino-geniculate pathways (reviewed in Kerschensteiner & Guido, 2017), and points towards a larger diversity of visual features encoded by dLGN neurons than commonly appreciated. This interpretation is supported by recent studies reporting “non-classical” responses in rodent dLGN (Cruz-Martín et al., 2014; Howarth et al., 2014; Marshel et al., 2012; Piscopo et al., 2013; Scholl et al., 2012; Zhao et al., 2013a), rabbit dLGN (Hei et al., 2014) and the koniocellular layers of primate dLGN (SK et al., 2013; White et al., 2001; Zeater et al., 2015), such as direction and orientation selectivity, and binocularity. While our factorization approach reveals an elaborate visual representation at the level of dLGN, whether and how many distinct functional types of dLGN neurons exist is an open question. A previous clustering study of dLGN responses to a large stimulus set estimated the number of functional clusters to be six (Piscopo et al., 2013). While the identified clusters undoubtedly have correlated response profiles, it is unclear to which degree their borders are strictly demarcated or instead the clusters rather form a continuum.

5.3 Functional connectivity of dLGN projections

In previous work, the question of retinogeniculate connectivity has been addressed from two different angles: while most studies have focused on the absolute number and weight of functional RGC inputs impinging on single dLGN neurons, some studies also assessed convergence of retinogeniculate inputs in terms of response type.

Focusing on RGC counts, there seems to be a prominent discrepancy of estimates between earlier mostly physiological work and recent anatomical studies. Indeed, a huge body of both *in-vitro* and *in-vivo* literature has concluded that dLGN neurons typically receive 1-3 dominant RGC inputs, with the possibility of additional, weaker ones (Chen & Regehr, 2000; Cleland et al., 1971; Jaubert-Miazza et al., 2005; Litvina & Chen, 2017b; Mastronarde, 1992; Reid & Usrey, 2004; Usrey et al., 1999; Weyand, 2016; Ziburkus & Guido, 2006). However, in some of the *in-vivo* studies the total number of RGC inputs might have been underestimated due to technical limitations (Sincich et al., 2007). In more details: In studies using single electrode to simultaneously record functional S-potentials and dLGN spikes, it has been difficult to determine the number of RGCs driving a dLGN cell (Bishop et al., 1962; Kaplan & Shapley, 1984; Mastronarde, 1987), because, the EPSP often merged with the dLGN spike, making it appear that many dLGN spikes had no associated EPSP. In the case of dual-electrode recordings where monosynaptically connected RGCs and dLGN cells were recorded simultaneously, it has been shown that dLGN neurons are usually driven by more than one RGC (Cleland et al., 1971; Mastronarde, 1987; Usrey et al., 1999). However, it is an open question whether these studies were able to differentiate between the input of a single RGC type and the input of a highly synchronous signal of many RGCs of the same type. Based on this assumption, it is indeed possible that number of converging RGCs is higher than previously reported.

Our number of modelled RGC input types is in line with estimates by a recent study using mono-transsynaptic rabies virus tracing (Rompani et al., 2017). This elegant tracing study provides evidence that at least a subset of dLGN neurons receive converging inputs from up to 91 different RGCs distributed across up to 9 types. The large discrepancy between anatomical estimates of convergence and functional connectivity might be related to the fact that, first, anatomical studies (Hammer et al., 2015; Morgan et al., 2016) usually provide RGC counts converging onto one dLGN relay cell, without specifying how the inputs are distributed among different RGC types. It is indeed possible, as showed by Rompani et al. (2017), that only few RGC types provide multiple inputs onto a single dLGN neuron. The

notion that each dLGN cell receives a weighted input from only a few RGC types is in agreement with results from functional studies investigating retinogeniculate connectivity. Second, the number of RGC counts in the anatomical studies (Hammer et al., 2015; Morgan et al., 2016; Rompani et al., 2017) might represent an overestimate. These studies were performed in young animals from postnatal day P21 to P42¹, where experience-dependent synapse remodelling and late axon pruning still take place (Hong et al., 2014). Many of the structurally identified connections can thus be the remnants of the RGC axon arbours.

Recently, it has been suggested that the underlying mechanism for the functional remodelling at the retinogeniculate synapse is more dynamic than previously appreciated. Hong et al. (2014) visualized axon arbours of a single dLGN-p RGC type (BD-RGC; Kim, Zhang, Meister, & Sanes, 2010) during different stages in development, and showed that not axon pruning but bouton clustering underlies the development of functional specificity at the retinogeniculate synapse during experience-dependent plasticity. During this period the RGC axon arbours may allow rapid reestablishment of previously eliminated connections. Plasticity dependent changes have also been demonstrated in the adult dLGN in a study, where silencing the ON-centre RGC inputs caused rapid emergence of OFF-centre responses from ON-centre neurons (Moore et al., 2011). This form of plasticity was previously associated with cortex, whereas subcortical structures were believed to lose their capacity for change after a critical period was reached during the development (Calford et al., 2000; Fox et al., 2002; Gilbert et al., 2009). In the study by Moore and colleagues (2011), the authors hypothesized that dLGN cells form functionally weak or silent synapses (Atwood & Wojtowicz, 1999) with multiple axons from different RGC types and that rapid strengthening of these synapses could serve as a substrate for adult plasticity in the retinogeniculate pathway. Evidence for this mechanism comes also from other studies, mentioning weakly connected RGCs and dLGN neurons with mismatched ON/OFF or X/Y signatures (Hamos et al., 1987; Mastronarde, 1992; Usrey et al., 1999). Taken together, these findings suggest an intriguing mechanism, which could indeed account for the multitude of RGCs converging onto a dLGN neuron in all aforementioned anatomical studies (Hammer et al., 2015; Morgan et al., 2016; Rompani et al., 2017)

While our results are in line with previous estimates of functional connectivity, our computational modelling approach has several limitations. First, due to the difference in

¹ The youngest animals used in our study were at least 8 weeks old (> P56), and thereby at the end of the experience-dependent phase (till P60).

recording methods, we can only predict low pass-filtered dLGN signals. This might result into a loss of fast transient components from the electrophysiological signal, and our data are thus bound to the kinetics of the calcium indicator (Chen et al., 2013). Second, our simple linear feed-forward model does not consider the potential effects caused by local inhibitory interneurons and cortico-thalamic feedback. Thereby our model might ignore important spatio-temporal transformations between RGC input and dLGN, which are modulated by cortico-geniculate feedback from V1 (reviewed in Briggs & Usrey, 2008). Despite the lack of this component and considering the simple modelling approach, we can explain the dLGN responses – at least to the given stimulus set – surprisingly well. Our results show that weighted linear combination of 3-7 different RGC types is sufficient to predict most dLGN responses.

5.4 Towards the development of a functional model of visual processing

However, to fully understand how the retinal code is interpreted and transformed along the retino-geniculo-cortical pathway, we would have to integrate the effects of cortico-geniculate feedback as a component into our model. Cortico-geniculate feedback provides the predominant synaptic input to dLGN, comprising approximately 30% of all synapses (Erişir et al., 1997). It is mediated by reciprocal projections from pyramidal cells in cortical layer 6 of V1 (Briggs & Usrey, 2011), whose axons form excitatory synaptic connections with dLGN neurons, as well as with inhibitory neurons of the thalamic reticular nucleus (TRN) and inhibitory interneurons residing in the dLGN (Jurgens et al., 2012; Sillito et al., 2006). By exciting GABAergic neurons in the TRN, feedback can also indirectly inhibit neurons as well as inhibitory interneurons in the dLGN (Sillito et al., 2006). Thus, the balance between this disynaptic inhibition and monosynaptic excitation determines the sign of the cortico-geniculate modulation. How and to what degree the representation of visual information is transformed by feedback in the dLGN is still a matter of current investigations, as studies of feedback-related effects have produced inconsistent results. It has been suggested that feedback can enhance contrast gain (Przybylski et al., 2000), influence the responsiveness to high-velocity stimuli (Gulyás et al., 1990), or even modify spatial summation properties of dLGN cells (Andolina et al., 2013). In mice, the effects of cortico-geniculate feedback have been studied using transgenic animals, where the genetically specified population of neurons in L6 of V1 has been optogenetically manipulated. Olsen et al. (2012) showed that dLGN neurons increased their firing rates upon silencing of feedback connections, whereas Denman and Contreras (2015) reported a mix of inhibitory and excitatory effects with no evidence for sharpening of tuning properties or improved temporal fidelity.

Here, our study provides the ideal basis for investigating how cortico-geniculate feedback contributes to the transformation of visual information between RGCs and dLGN neurons. Our approach could easily be combined with the expression of light-gated neuronal silencers in L6 of V1 for specific and reversible inactivation of cortico-geniculate feedback (similar to Olsen et al., 2012). An example of such silencers could be the novel light-gated chloride channels (e.g. SwiChR⁺⁺), which showed improved efficiency for optical inhibition of neurons (Berndt et al., 2016). To provide a quantitative assessment of the effects of cortico-geniculate feedback on dLGN neurons, we could present the same stimuli used in this study in conditions with and without cortico-geniculate feedback, and compare the responses of

individual neurons. With the data we could extend our simple feed-forward model and thus provide the first important step towards the development of a functional model of visual processing in the mammalian brain.

6 References

- Albrecht, D. G., & Hamilton, D. B. (1982). Striate cortex of monkey and cat: contrast response function. *Journal of Neurophysiology*, 48(1), 217–237. [https://doi.org/0022-3077/82/0000-0000\\$01.25](https://doi.org/0022-3077/82/0000-0000$01.25)
- Amthor, F. R., & Oyster, C. W. (1995). Spatial organization of retinal information about the direction of image motion. *Proceedings of the National Academy of Sciences of the United States of America*, 92(9), 4002–4005. <https://doi.org/10.1073/pnas.92.9.4002>
- Andolina, I. M., Jones, H. E., & Sillito, A. M. (2013). Effects of cortical feedback on the spatial properties of relay cells in the lateral geniculate nucleus. *Journal of Neurophysiology*, 109(3), 889–899. <https://doi.org/10.1152/jn.00194.2012>
- Antinone, S. E., & Smith, G. A. (2010). Retrograde Axon Transport of Herpes Simplex Virus and Pseudorabies Virus: a Live-Cell Comparative Analysis. *Journal of Virology*, 84(3), 1504–1512. <https://doi.org/10.1128/JVI.02029-09>
- Atwood, H. L., & Wojtowicz, J. M. (1999). Silent Synapses in Neural Plasticity: Current Evidence Silent Synapses in Neural Plasticity: Current Evidence. *Learn. Mem.*, 6(6), 542–571.
- Awatramani, G. B. and M. M. S. (2000). Origin of Transient and Sustained Responses in Ganglion Cells of the Retina. *Journal of Neuroscience*, 20(18), 7087–7095. <https://doi.org/20/18/7087> [pii]
- Azeredo da Silveira, R., & Roska, B. (2011). Cell Types, Circuits, Computation. *Current Opinion in Neurobiology*. <https://doi.org/10.1016/j.conb.2011.05.007>
- Baden, T., Berens, P., Franke, K., Román Rosón, M., Bethge, M., & Euler, T. (2016). The functional diversity of retinal ganglion cells in the mouse. *Nature*, 529(7586), 345–350. <https://doi.org/10.1038/nature16468>
- Baden, T., Schubert, T., Chang, L., Wei, T., Zaichuk, M., Wissinger, B., & Euler, T. (2013). A tale of two retinal domains: Near-Optimal sampling of achromatic contrasts in natural scenes through asymmetric photoreceptor distribution. *Neuron*, 80(5), 1206–1217. <https://doi.org/10.1016/j.neuron.2013.09.030>
- Barlow, H. B., Hill, R. M., & Levick, W. R. (1964). Retinal ganglion cells responding selectively to direction and speed of image motion in the rabbit. *The Journal of Physiology*, 173(3), 377–407. <https://doi.org/10.1113/jphysiol.1964.sp007463>
- Behrens, C., Schubert, T., Haverkamp, S., Euler, T., & Berens, P. (2016). Connectivity map of bipolar cells and photoreceptors in the mouse retina. *eLife*, 5(NOVEMBER2016). <https://doi.org/10.7554/eLife.20041>
- Berens, P., Freeman, J., Deneux, T., Chenkov, N., Mccolgan, T., Speiser, A., ... Reimer, J. (2017). Community-based benchmarking improves spike inference from two-photon calcium imaging data. *Emmanoulis Froudarakis Andreas S. Tolia*, 1718181920(16). <https://doi.org/10.1101/177956>

- Berndt, A., Lee, S. Y., Wietek, J., Ramakrishnan, C., Steinberg, E. E., Rashid, A. J., ... Deisseroth, K. (2016). Structural foundations of optogenetics: Determinants of channelrhodopsin ion selectivity. *Proceedings of the National Academy of Sciences*, *113*(4), 822–829. <https://doi.org/10.1073/pnas.1523341113>
- Berson, D. M. (2008). Retinal ganglion cell types and their central projections. In *The Senses: a Comprehensive Reference* (pp. 491–520). <https://doi.org/10.1016/B978-012370880-9.00280-2>
- Bickford, M. E., Zhou, N., Krahe, T. E., Govindaiah, G., & Guido, W. (2015). Retinal and Tectal “Driver-Like” Inputs Converge in the Shell of the Mouse Dorsal Lateral Geniculate Nucleus. *Journal of Neuroscience*, *35*(29), 10523–10534. <https://doi.org/10.1523/JNEUROSCI.3375-14.2015>
- Bishop, P., Burke, W., & Davis, R. (1962). The interpretation of the extracellular response of single lateral geniculate cells. *The Journal of Physiology*, 451–472. <https://doi.org/10.1113/jphysiol.1962.sp006944>
- Bouabe, H., & Okkenhaug, K. (2013). Gene targeting in mice: A review. *Methods in Molecular Biology*. https://doi.org/10.1007/978-1-62703-601-6_23
- Breuninger, T., Puller, C., Haverkamp, S., & Euler, T. (2011). Chromatic Bipolar Cell Pathways in the Mouse Retina. *Journal of Neuroscience*, *31*(17), 6504–6517. <https://doi.org/10.1523/JNEUROSCI.0616-11.2011>
- Briggman, K. L., & Euler, T. (2011). Bulk electroporation and population calcium imaging in the adult mammalian retina. *Journal of Neurophysiology*, *105*(5), 2601–2609. <https://doi.org/10.1152/jn.00722.2010>
- Briggs, F., & Usrey, W. M. (2008). Emerging views of corticothalamic function. *Current Opinion in Neurobiology*. <https://doi.org/10.1016/j.conb.2008.09.002>
- Briggs, F., & Usrey, W. M. (2011). Corticogeniculate feedback and visual processing in the primate. *The Journal of Physiology*, *589*(1), 33–40. <https://doi.org/10.1113/jphysiol.2010.193599>
- Brown, T. M., Gias, C., Hatori, M., Keding, S. R., Semo, M., Coffey, P. J., ... Lucas, R. J. (2010). Melanopsin contributions to irradiance coding in the thalamo-cortical visual system. *PLoS Biology*, *8*(12), e1000558. <https://doi.org/10.1371/journal.pbio.1000558>
- Buhl, E. H., & Peichl, L. (1986). Morphology of rabbit retinal ganglion cells projecting to the medial terminal nucleus of the accessory optic system. *Journal of Comparative Neurology*, *253*(2), 163–174. <https://doi.org/10.1002/cne.902530204>
- Calford, M. B., Wang, C., Taglianetti, V., Waleszczyk, W. J., Burke, W., & Dreher, B. (2000). Plasticity in adult cat visual cortex (area 17) following circumscribed monocular lesions of all retinal layers. *Journal of Physiology*, *524*(2), 587–602. <https://doi.org/10.1111/j.1469-7793.2000.t01-1-00587.x>
- Chen, C., Bickford, M. E., & Hirsch, J. A. (2016). Untangling the Web between Eye and Brain. *Cell*. <https://doi.org/10.1016/j.cell.2016.03.010>
- Chen, C., & Regehr, W. G. (2000). Developmental remodeling of the retinogeniculate synapse. *Neuron*, *28*(3), 955–966. [https://doi.org/10.1016/S0896-6273\(00\)00166-5](https://doi.org/10.1016/S0896-6273(00)00166-5)

- Chen, T.-W., Wardill, T. J., Sun, Y., Pulver, S. R., Renninger, S. L., Baohan, A., ... Kim, D. S. (2013). Ultrasensitive fluorescent proteins for imaging neuronal activity. *Nature*, *499*(7458), 295–300. <https://doi.org/10.1038/nature12354>
- Cleland, B. G., Dubin, M. W., & Levick, W. R. (1971). Simultaneous recording of input and output of lateral geniculate neurons. *Nat New Biology*, *231*(23), 191–2.
- CM, N., & MP, S. (2008). Highly selective receptive fields in mouse visual cortex. *J. Neurosci.*, *28*(30), 7520–7536.
- Cruz-Martín, A., El-Danaf, R. N., Osakada, F., Sriram, B., Dhande, O. S., Nguyen, P. L., ... Huberman, A. D. (2014). A dedicated circuit links direction-selective retinal ganglion cells to the primary visual cortex. *Nature*, *507*(7492), 358–361. <https://doi.org/10.1038/nature12989>
- Dacey, D. M., Peterson, B. B., Robinson, F. R., & Gamlin, P. D. (2003). Fireworks in the Primate Retina: Neurotechnique LGN-Projecting Ganglion Cell Types. *Neuron*, *37*(1), 15–27. <https://doi.org/S0896627302011431> [pii]
- de Monasterio, F. M. (1978). Properties of ganglion cells with atypical receptive-field organization in retina of macaques. *Journal of Neurophysiology*, *41*(6), 1435–49. <https://doi.org/10.1152/jn.01171.2003>
- De Monasterio, F. M., & Gouras, P. (1975). Functional properties of ganglion cells of the rhesus monkey retina. *The Journal of Physiology*, *251*(1), 167–195. <https://doi.org/10.1113/jphysiol.1975.sp011086>
- Demb, J. B., & Singer, J. H. (2015). Functional Circuitry of the Retina. *Annual Review of Vision Science*, *1*(1), 263–289. <https://doi.org/10.1146/annurev-vision-082114-035334>
- Denman, D. J., & Contreras, D. (2015). Complex Effects on In Vivo Visual Responses by Specific Projections from Mouse Cortical Layer 6 to Dorsal Lateral Geniculate Nucleus. *Journal of Neuroscience*, *35*(25), 9265–9280. <https://doi.org/10.1523/JNEUROSCI.0027-15.2015>
- Denman, D. J., & Contreras, D. (2016). On Parallel Streams through the Mouse Dorsal Lateral Geniculate Nucleus. *Frontiers in Neural Circuits*, *10*, 20. <https://doi.org/10.3389/fncir.2016.00020>
- Dhande, O. S., Estevez, M. E., Quattrochi, L. E., El-Danaf, R. N., Nguyen, P. L., Berson, D. M., & Huberman, A. D. (2013). Genetic Dissection of Retinal Inputs to Brainstem Nuclei Controlling Image Stabilization. *Journal of Neuroscience*, *33*(45), 17797–17813. <https://doi.org/10.1523/JNEUROSCI.2778-13.2013>
- Dhande, O. S., Stafford, B. K., Lim, J.-H. A., & Huberman, A. D. (2015). Contributions of Retinal Ganglion Cells to Subcortical Visual Processing and Behaviors. *Annual Review of Vision Science*, *1*(1), 291–328. <https://doi.org/10.1146/annurev-vision-082114-035502>
- Dombeck, D. A., Khabbaz, A. N., Collman, F., Adelman, T. L., & Tank, D. W. (2007). Imaging Large-Scale Neural Activity with Cellular Resolution in Awake, Mobile Mice. *Neuron*, *56*(1), 43–57. <https://doi.org/10.1016/j.neuron.2007.08.003>
- Dorostkar, M. M., Dreosti, E., Odermatt, B., & Lagnado, L. (2010). Computational processing of optical measurements of neuronal and synaptic activity in networks. *Journal of Neuroscience Methods*, *188*(1), 141–150.

- <https://doi.org/10.1016/j.jneumeth.2010.01.033>
- Dowling, J. E., & Werblin, F. S. (1969). Organization of retina of the mudpuppy, *Necturus maculosus*. I. Synaptic structure. *Journal of Neurophysiology*, 32(3), 315–38. Retrieved from <http://jn.physiology.org/highwire/citation/296372/mendeley%5Cnhttp://www.ncbi.nlm.nih.gov/pubmed/5787842>
- Dreher, B., Sefton, A. J., Ni, S. Y. K., & Nisbett, G. (1985). The morphology, number, distribution and central projection of class I retinal ganglion cells in albino and hooded rats. *Brain Behav.Evol.*, 26(1), 10–48.
- Ecker, A. S., Berens, P., Cotton, R. J., Subramaniyan, M., Denfield, G. H., Cadwell, C. R., ... Tolia, A. S. (2014). State Dependence of Noise Correlations in Macaque Primary Visual Cortex. *Neuron*, 82(1), 235–248. <https://doi.org/10.1016/j.neuron.2014.02.006>
- Ecker, J. L., Dumitrescu, O. N., Wong, K. Y., Alam, N. M., Chen, S. K., LeGates, T., ... Hattar, S. (2010). Melanopsin-expressing retinal ganglion-cell photoreceptors: Cellular diversity and role in pattern vision. *Neuron*, 67(1), 49–60. <https://doi.org/10.1016/j.neuron.2010.05.023>
- Eggers, E. D., & Lukasiewicz, P. D. (2010). Interneuron circuits tune inhibition in retinal bipolar cells. *Journal of Neurophysiology*, 103(1), 25–37. <https://doi.org/10.1152/jn.00458.2009>
- EGGERS, E. D., & LUKASIEWICZ, P. D. (2011). Multiple pathways of inhibition shape bipolar cell responses in the retina. *Visual Neuroscience*, 28(1), 95–108. <https://doi.org/10.1017/S0952523810000209>
- Ellis, E. M., Gauvain, G., Sivy, B., & Murphy, G. J. (2016). Shared and distinct retinal input to the mouse superior colliculus and dorsal lateral geniculate nucleus. *Journal of Neurophysiology*, 116(2), 602–610. <https://doi.org/10.1152/jn.00227.2016>
- Enroth-Cugell, C., & Robson, J. G. (1966). The contrast sensitivity of retinal ganglion cells of the cat. *The Journal of Physiology*, 187(3), 517–552. <https://doi.org/10.1113/jphysiol.1966.sp008107>
- Erişir, A., Van Horn, S. C., & Sherman, S. M. (1997). Relative numbers of cortical and brainstem inputs to the lateral geniculate nucleus. *Proceedings of the National Academy of Sciences of the United States of America*, 94(4), 1517–20. <https://doi.org/10.1073/pnas.94.4.1517>
- Erisken, S., Vaiceliunaite, A., Jurjut, O., Fiorini, M., Katzner, S., & Busse, L. (2014). Effects of locomotion extend throughout the mouse early visual system. *Current Biology*, 24(24), 2899–2907. <https://doi.org/10.1016/j.cub.2014.10.045>
- Estevez, M. E., Fogerson, P. M., Ilardi, M. C., Borghuis, B. G., Chan, E., Weng, S., ... Berson, D. M. (2012). Form and Function of the M4 Cell, an Intrinsically Photosensitive Retinal Ganglion Cell Type Contributing to Geniculocortical Vision. *Journal of Neuroscience*, 32(39), 13608–13620. <https://doi.org/10.1523/JNEUROSCI.1422-12.2012>

- Euler, T., Hausselt, S. E., Margolis, D. J., Breuninger, T., Castell, X., Detwiler, P. B., & Denk, W. (2009). Eyecup scope-optical recordings of light stimulus-evoked fluorescence signals in the retina. *Pflugers Archiv European Journal of Physiology*, *457*(6), 1393–1414. <https://doi.org/10.1007/s00424-008-0603-5>
- Euler, T., Haverkamp, S., Schubert, T., & Baden, T. (2014). Retinal bipolar cells: Elementary building blocks of vision. *Nature Reviews Neuroscience*. <https://doi.org/10.1038/nrn3783>
- Euler, T., Schneider, H., & Wässle, H. (1996). Glutamate responses of bipolar cells in a slice preparation of the rat retina. *Investigative Ophthalmology and Visual Science*, *37*(3).
- Farrow, K., & Masland, R. H. (2011). Physiological clustering of visual channels in the mouse retina. *Journal of Neurophysiology*, *105*(4), 1516–30. <https://doi.org/10.1152/jn.00331.2010>
- Fox, K., Wallace, H., & Glazewski, S. (2002). Is there a thalamic component to experience-dependent cortical plasticity? *Philosophical Transactions of the Royal Society B: Biological Sciences*, *357*(1428), 1709–1715. <https://doi.org/10.1098/rstb.2002.1169>
- Franke, K., Berens, P., Schubert, T., Bethge, M., Euler, T., & Baden, T. (2017). Inhibition decorrelates visual feature representations in the inner retina. *Nature*, *542*(7642), 439–444. <https://doi.org/10.1038/nature21394>
- Frigyesi, A., & Höglund, M. (2008). Non-negative matrix factorization for the analysis of complex gene expression data: Identification of clinically relevant tumor subtypes. *Cancer Informatics*, *6*, 275–292.
- Fyk-Kolodziej, B., Qin, P., & Pourcho, R. G. (2003). Identification of a cone bipolar cell in cat retina which has input from both rod and cone photoreceptors. *Journal of Comparative Neurology*, *464*(1), 104–113. <https://doi.org/10.1002/cne.10784>
- Gao, E., DeAngelis, G. C., & Burkhalter, A. (2010). Parallel Input Channels to Mouse Primary Visual Cortex. *Journal of Neuroscience*, *30*(17), 5912–5926. <https://doi.org/10.1523/JNEUROSCI.6456-09.2010>
- Gasser, H. S., & Erlanger, J. (1929). The role of fiber size in the establishment of a nerve block by pressure or cocaine. *American Journal of Physiology*, *88*(4), 581–591. Retrieved from <http://ajplegacy.physiology.org/content/88/4/581.full.pdf+html>
- Gilbert, C. D., Li, W., & Piech, V. (2009). Perceptual learning and adult cortical plasticity. *The Journal of Physiology*, *587*(12), 2743–2751. <https://doi.org/10.1113/jphysiol.2009.171488>
- Gollisch, T., & Meister, M. (2010). Eye Smarter than Scientists Believed: Neural Computations in Circuits of the Retina. *Neuron*. <https://doi.org/10.1016/j.neuron.2009.12.009>
- Greene, M. J., Kim, J. S., & Seung, H. S. (2016). Analogous Convergence of Sustained and Transient Inputs in Parallel On and Off Pathways for Retinal Motion Computation. *Cell Reports*, *14*(8), 1892–1900. <https://doi.org/10.1016/j.celrep.2016.02.001>
- Grubb, M. S. (2003). Quantitative Characterization of Visual Response Properties in the Mouse Dorsal Lateral Geniculate Nucleus. *Journal of Neurophysiology*, *90*(6), 3594–3607. <https://doi.org/10.1152/jn.00699.2003>

- Guido, W. (2008). Refinement of the retinogeniculate pathway. *The Journal of Physiology*, 586(18), 4357–4362. <https://doi.org/10.1113/jphysiol.2008.157115>
- Guillery, R. W., & Sherman, S. M. (2002). Thalamic relay functions and their role in corticocortical communication: Generalizations from the visual system. *Neuron*, 33(2), 163–175. [https://doi.org/10.1016/S0896-6273\(01\)00582-7](https://doi.org/10.1016/S0896-6273(01)00582-7)
- Gulyás, B., Lagae, L., Eysel, U., & Orban, G. A. (1990). Corticofugal feedback influences the responses of geniculate neurons to moving stimuli. *Experimental Brain Research*, 79(2), 441–446. <https://doi.org/10.1007/BF00608257>
- Hack, I., Peichl, L., & Brandstätter, J. H. (1999). An alternative pathway for rod signals in the rodent retina: rod photoreceptors, cone bipolar cells, and the localization of glutamate receptors. *Proceedings of the National Academy of Sciences of the United States of America*, 96(24), 14130–14135. <https://doi.org/10.1073/pnas.96.24.14130>
- Hammer, S., Monavarfeshani, A., Lemon, T., Su, J., & Fox, M. A. (2015). Multiple Retinal Axons Converge onto Relay Cells in the Adult Mouse Thalamus. *Cell Reports*, 12(10), 1575–1583. <https://doi.org/10.1016/j.celrep.2015.08.003>
- Hamos, J. E., Van Horn, S. C., Raczkowski, D., & Sherman, S. M. (1987). Synaptic circuits involving an individual retinogeniculate axon in the cat. *Journal of Comparative Neurology*, 259(2), 165–192. <https://doi.org/10.1002/cne.902590202>
- Harting, J. K., Huerta, M. F., Hashikawa, T., & Van Lieshout, D. P. (1991). Projection of the mammalian superior colliculus upon the dorsal lateral geniculate-nucleus: organization of tectogeniculate pathways in 19 species. *J Comp Neurol*, 304(2), 275–306.
- Haverkamp, S. (2005). The Primordial, Blue-Cone Color System of the Mouse Retina. *Journal of Neuroscience*, 25(22), 5438–5445. <https://doi.org/10.1523/JNEUROSCI.1117-05.2005>
- Hazan, L., Zugaro, M., & Buzsáki, G. (2006). Klusters, NeuroScope, NDManager: A free software suite for neurophysiological data processing and visualization. *Journal of Neuroscience Methods*, 155(2), 207–216. <https://doi.org/10.1016/j.jneumeth.2006.01.017>
- Hei, X., Stoelzel, C. R., Zhuang, J., Bereshpolova, Y., Huff, J. M., Alonso, J.-M., & Swadlow, H. A. (2014). Directional selective neurons in the awake LGN: response properties and modulation by brain state. *Journal of Neurophysiology*, 112(2), 362–373. <https://doi.org/10.1152/jn.00121.2014>
- Helmstaedter, M., Briggman, K. L., Turaga, S. C., Jain, V., Seung, H. S., & Denk, W. (2013). Connectomic reconstruction of the inner plexiform layer in the mouse retina. *Nature*, 500(7461), 168–174. <https://doi.org/10.1038/nature12346>
- Henze, D. a, Borhegyi, Z., Csicsvari, J., Mamiya, a, Harris, K. D., & Buzsáki, G. (2000). Intracellular features predicted by extracellular recordings in the hippocampus in vivo. *Journal of Neurophysiology*, 84(1), 390–400. <https://doi.org/10.1152/jn.2000.84.1.390>
- Hong, Y. K., Park, S. H., Litvina, E. Y., Morales, J., Sanes, J. R., & Chen, C. (2014). Refinement of the Retinogeniculate Synapse by Bouton Clustering. *Neuron*, 84(2), 332–339. <https://doi.org/10.1016/j.neuron.2014.08.059>

- Howarth, M., Walmsley, L., & Brown, T. M. (2014). Binocular integration in the mouse lateral geniculate nuclei. *Current Biology*, 24(11), 1241–1247. <https://doi.org/10.1016/j.cub.2014.04.014>
- Hubel, D. H., & Wiesel, T. N. (1961). Integrative Action in the Cat's Lateral Geniculate Body. *The Journal of Physiology*, 155(2), 385–398. <https://doi.org/10.1113/jphysiol.1961.sp006635>
- Huberman, A. D., & Dhande, O. S. (2014). Retinal ganglion cell maps in the brain: implications for visual processing. *Current Opinion in Neurobiology*, 24(1), 133–142. Retrieved from <http://dx.doi.org/10.1016/j.conb.2013.08.006%5Cnfile:///Files/03/03B94234-3E1B-4176-B4D5-E4A439F2A142.pdf%5Cnpapers3://publication/doi/10.1016/j.conb.2013.08.006>
- Huberman, A. D., Manu, M., Koch, S. M., Susman, M. W., Lutz, A. B., Ullian, E. M., ... Barres, B. A. (2008). Architecture and Activity-Mediated Re nement of Axonal Projections from a Mosaic of Genetically Identi ed Retinal Ganglion Cells. *Neuron*, 59(1), 425–438. <https://doi.org/10.1016/j.neuron.2008.07.018>
- Huberman, A. D., & Niell, C. M. (2011). What can mice tell us about how vision works? *Trends in Neurosciences*, 34(9), 464–473. <https://doi.org/10.1016/j.tins.2011.07.002>
- Huberman, A. D., Wei, W., Elstrott, J., Stafford, B. K., Feller, M. B., & Barres, B. A. (2009). Genetic identification of an On-Off direction-selective retinal ganglion cell subtype reveals a layer-specific subcortical map of posterior motion. *Neuron*, 62(3), 327–334. <https://doi.org/10.1016/j.neuron.2009.04.014>
- Illing, R. ???B, & W???sle, H. (1981). The retinal projection to the thalamus in the cat: A quantitative investigation and a comparison with the retinotectal pathway. *Journal of Comparative Neurology*, 202(2), 265–285. <https://doi.org/10.1002/cne.902020211>
- Jaubert-Miazza, L., Erick, G., Lo, F.-S., Bui, K., Mills, J., & Guido, W. (2005). Structural and functional composition of the developing retinogeniculate pathway in the mouse. *Visual Neuroscience*, 22(5), 661–676. <https://doi.org/10.1017/S0952523805225154>
- Jurgens, C. W. D., Bell, K. A., McQuiston, A. R., & Guido, W. (2012). Optogenetic Stimulation of the Corticothalamic Pathway Affects Relay Cells and GABAergic Neurons Differently in the Mouse Visual Thalamus. *PLoS ONE*, 7(9). <https://doi.org/10.1371/journal.pone.0045717>
- Kaplan, E., Purpura, K., & Shapley, R. M. (1987). Contrast affects the transmission of visual information through the mammalian lateral geniculate nucleus. *The Journal of Physiology*, 391, 267–88. <https://doi.org/10.1113/jphysiol.1987.sp016737>
- Kaplan, E., & Shapley, R. (1984). The origin of the S (slow) potential in the mammalian Lateral Geniculate Nucleus. *Experimental Brain Research*, 55(1), 111–116. <https://doi.org/10.1007/BF00240504>
- Katzner, S., Busse, L., & Carandini, M. (2011). GABAA Inhibition Controls Response Gain in Visual Cortex. *Journal of Neuroscience*, 31(16), 5931–5941. <https://doi.org/10.1523/JNEUROSCI.5753-10.2011>

- Kay, J. N., De la Huerta, I., Kim, I.-J., Zhang, Y., Yamagata, M., Chu, M. W., ... Sanes, J. R. (2011). Retinal Ganglion Cells with Distinct Directional Preferences Differ in Molecular Identity, Structure, and Central Projections. *Journal of Neuroscience*, *31*(21), 7753–7762. <https://doi.org/10.1523/JNEUROSCI.0907-11.2011>
- Kerschensteiner, D., & Guido, W. (2017). Organization of the dorsal lateral geniculate nucleus in the mouse. *Visual Neuroscience*, *34*, E008. <https://doi.org/10.1017/S0952523817000062>
- Kim, H., & Park, H. (2007). Sparse Non-negative matrix factorization via alternating non-negativity constrained least squares for microarray data analysis. *Bioinformatics*, *23*(12), 1495–1502.
- Kim, I.-J., Zhang, Y., Meister, M., & Sanes, J. R. (2010). Laminal Restriction of Retinal Ganglion Cell Dendrites and Axons: Subtype-Specific Developmental Patterns Revealed with Transgenic Markers. *Journal of Neuroscience*, *30*(4), 1452–1462. <https://doi.org/10.1523/JNEUROSCI.4779-09.2010>
- Kim, I., Zhang, Y., Yamagata, M., Meister, M., Sanes, J. R., & Biology, C. (2008). Molecular Identification of a Novel Retinal Cell Type That Responds To. *Nature*, *452*(7186), 1–8. <https://doi.org/10.1038/nature0>
- Kim, J. S., Greene, M. J., Zlateski, A., Lee, K., Richardson, M., Turaga, S. C., ... Seung, H. S. (2014). Space-time wiring specificity supports direction selectivity in the retina. *Nature*, *509*(7500), 331–336. <https://doi.org/10.1038/nature13240>
- Kolb, H. (1979). The inner plexiform layer in the retina of the cat: electron microscopic observations. *Journal of Neurocytology*, *8*(3), 295–329. <https://doi.org/10.1007/BF01236124>
- Korenbrodt, J. I. (2012). Speed, sensitivity, and stability of the light response in rod and cone photoreceptors: Facts and models. *Progress in Retinal and Eye Research*. <https://doi.org/10.1016/j.preteyeres.2012.05.002>
- Krahe, T. E., El-Danaf, R. N., Dilger, E. K., Henderson, S. C., & Guido, W. (2011). Morphologically Distinct Classes of Relay Cells Exhibit Regional Preferences in the Dorsal Lateral Geniculate Nucleus of the Mouse. *Journal of Neuroscience*, *31*(48), 17437–17448. <https://doi.org/10.1523/JNEUROSCI.4370-11.2011>
- Krieger, B., Qiao, M., Rousso, D. L., Sanes, J. R., & Meister, M. (2017). Four alpha ganglion cell types in mouse retina: Function, structure, and molecular signatures. *PLoS ONE*, *12*(7). <https://doi.org/10.1371/journal.pone.0180091>
- Lettvin, J. Y., Maturana, H. R., Maturana, H. R., McCulloch, W. S., & Pitts, W. H. (1959). What the Frog's Eye Tells the Frog's Brain. *Proceedings of the IRE*, *47*(11), 1940–1951. <https://doi.org/10.1109/JRPROC.1959.287207>
- Levick, W. R. (1967). Receptive fields and trigger features of ganglion cells in the visual streak of the rabbit's retina. *Journal of Physiology*, *188*(3), 285–307. <https://doi.org/10.1113/jphysiol.1967.sp008140>
- Li, Y., & Ngom, A. (2013). The non-negative matrix factorization toolbox for biological data mining. *Source Code for Biology and Medicine*, *8*(1), 10. <https://doi.org/10.1186/1751-0473-8-10>

- Linden, R., & Perry, V. H. (1983). Massive retinotectal projection in rats. *Brain Research*, 272(1), 145–149. [https://doi.org/10.1016/0006-8993\(83\)90371-2](https://doi.org/10.1016/0006-8993(83)90371-2)
- Litvina, E. Y., & Chen, C. (2017a). An evolving view of retinogeniculate transmission. *Visual Neuroscience*, 34, E013. <https://doi.org/10.1017/S0952523817000104>
- Litvina, E. Y., & Chen, C. (2017b). Functional Convergence at the Retinogeniculate Synapse. *Neuron*, 96(2), 330–338. <https://doi.org/10.1016/j.neuron.2017.09.037>
- Liu, B., Li, P., Sun, Y. J., Zhang, L. I., & Tao, H. W. (2010). Intervening Inhibition Specifies Receptive Field Structure in Visual Cortex. *Cell*, 13(1), 89–96.
- MacNeil, M. A., & Masland, R. H. (1998). Extreme diversity among amacrine cells: Implications for function. *Neuron*, 20(5), 971–982. [https://doi.org/10.1016/S0896-6273\(00\)80478-X](https://doi.org/10.1016/S0896-6273(00)80478-X)
- Madisen, L., Garner, A. R., Carandini, M., Zeng, H., Madisen, L., Garner, A. R., ... Cheng, A. (2015). supplementary info Transgenic Mice for Intersectional Targeting of Neural Sensors and Effectors with High Specificity and Performance NeuroResource Transgenic Mice for Intersectional Targeting of Neural Sensors and Effectors with High Specificity and Perf. *Neuron*, 85(5), 942–958. <https://doi.org/10.1016/j.neuron.2015.02.022>
- Marshel, J. H., Kaye, A. P., Nauhaus, I., & Callaway, E. M. (2012). Anterior-Posterior Direction Opponency in the Superficial Mouse Lateral Geniculate Nucleus. *Neuron*, 76(4), 713–720. <https://doi.org/10.1016/j.neuron.2012.09.021>
- Martersteck, E. M., Hirokawa, K. E., Evarts, M., Bernard, A., Duan, X., Li, Y., ... Harris, J. A. (2017). Diverse Central Projection Patterns of Retinal Ganglion Cells. *Cell Reports*, 18(8), 2058–2072. <https://doi.org/10.1016/j.celrep.2017.01.075>
- Martin, P. R. (1986). The Projection of Different Retinal Ganglion-Cell Classes to the Dorsal Lateral Geniculate-Nucleus in the Hooded Rat. *Experimental Brain Research*, 62(1), 77–88.
- Masland, R. H. (2012). The Neuronal Organization of the Retina. *Neuron*, 76(2), 266–280. <https://doi.org/10.1016/j.neuron.2012.10.002>
- Masland, R. H., & Martin, P. R. (2007). The {Unsolved} {Mystery} {Of} {The} {AIDS} {Dentist}. *KnowledgeNuts*, 17(15), 577–582. Retrieved from <http://knowledgenuts.com/2013/10/25/the-unsolved-mystery-of-the-aids-dentist/>
- Mastrorarde, D. N. (1987). Two classes of single-input X-cells in cat lateral geniculate nucleus. II. Retinal inputs and the generation of receptive-field properties. *Journal of Neurophysiology*, 57(2), 381–413. Retrieved from <http://www.ncbi.nlm.nih.gov/pubmed/3559685>
- Mastrorarde, D. N. (1992). Nonlagged relay cells and interneurons in the cat lateral geniculate nucleus: receptive-field properties and retinal inputs. *Visual Neuroscience*, 8(5), 407–41. <https://doi.org/10.1017/S0952523800004934>
- McGavern, D. B., & Kang, S. S. (2011). Illuminating viral infections in the nervous system. *Nature Reviews Immunology*, 11(5), 318–329. <https://doi.org/10.1038/nri2971>

- MONAVARFESHANI, A., SABBAGH, U., & FOX, M. A. (2017). Not a one-trick pony: Diverse connectivity and functions of the rodent lateral geniculate complex. *Visual Neuroscience*, *34*, E012. <https://doi.org/10.1017/S0952523817000098>
- Moore, B. D., Kiley, C. W., Sun, C., & Usrey, W. M. (2011). Rapid Plasticity of Visual Responses in the Adult Lateral Geniculate Nucleus. *Neuron*, *71*(5), 812–819.
- Morgan, J. L., Berger, D. R., Wetzel, A. W., & Lichtman, J. W. (2016). The Fuzzy Logic of Network Connectivity in Mouse Visual Thalamus. *Cell*, *165*(1), 192–206. <https://doi.org/10.1016/j.cell.2016.02.033>
- Muir-Robinson, G., Hwang, B. J., & Feller, M. B. (2002). Retinogeniculate axons undergo eye-specific segregation in the absence of eye-specific layers. *The Journal of Neuroscience: The Official Journal of the Society for Neuroscience*, *22*(13), 5259–5264. <https://doi.org/20026563>
- Münch, T. A., Da Silveira, R. A., Siegert, S., Viney, T. J., Awatramani, G. B., & Roska, B. (2009). Approach sensitivity in the retina processed by a multifunctional neural circuit. *Nature Neuroscience*, *12*(10), 1308–1316. <https://doi.org/10.1038/nn.2389>
- Nassi, J. J., & Callaway, E. M. (2009). Parallel processing strategies of the primate visual system. *Nature Reviews Neuroscience*. <https://doi.org/10.1038/nrn2619>
- Neve, R. L., Neve, & L., R. (2012a). Overview of Gene Delivery into Cells Using HSV-1-Based Vectors. *Current Protocols in Neuroscience*, *Chapter 4*, 4.12.1-4.12.7. <https://doi.org/10.1002/0471142301.ns0412s61>
- Neve, R. L., Neve, & L., R. (2012b). Overview of Gene Delivery into Cells Using HSV-1-Based Vectors. In *Current Protocols in Neuroscience* (p. 4.12.1-4.12.7). <https://doi.org/10.1002/0471142301.ns0412s61>
- Niell, C. M., & Stryker, M. (2010). Modulation of Visual Responses by Behavioral State in Mouse Visual Cortex. *Neuron*, *65*(4), 472–479. <https://doi.org/10.1016/j.neuron.2010.01.033>
- Nikolaus, R., & Paper, T. (2007). Learning the Parts of Objects using Non-negative Matrix Factorization (NMF). *Nature*, *401*(6755), 788–791.
- Olsen, S. R., Bortone, D. S., Adesnik, H., & Scanziani, M. (2012). Gain control by layer six in cortical circuits of vision. *Nature*, *483*(7387), 47–54. <https://doi.org/10.1038/nature10835>
- Pang, J.-J., Gao, F., Lem, J., Bramblett, D. E., Paul, D. L., & Wu, S. M. (2010). Direct rod input to cone BCs and direct cone input to rod BCs challenge the traditional view of mammalian BC circuitry. *Proceedings of the National Academy of Sciences*, *107*(1), 395–400. <https://doi.org/10.1073/pnas.0907178107>
- Pang, J.-J., Gao, F., & Wu, S. M. (2003). Light-evoked excitatory and inhibitory synaptic inputs to ON and OFF alpha ganglion cells in the mouse retina. *The Journal of Neuroscience: The Official Journal of the Society for Neuroscience*, *23*(14), 6063–6073.
- Peichl, L. (2005). Diversity of mammalian photoreceptor properties: Adaptations to habitat and lifestyle? In *Anatomical Record - Part A Discoveries in Molecular, Cellular, and Evolutionary Biology* (Vol. 287, pp. 1001–1012). <https://doi.org/10.1002/ar.a.20262>

- Perry, V. H., & Cowey, A. (1984). Retinal ganglion cells that project to the dorsal lateral geniculate nucleus in the macaque monkey. *Neuroscience*, *12*(4), 1101–1123. [https://doi.org/10.1016/0306-4522\(84\)90006-X](https://doi.org/10.1016/0306-4522(84)90006-X)
- Piscopo, D. M., El-Danaf, R. N., Huberman, A. D., & Niell, C. M. (2013). Diverse Visual Features Encoded in Mouse Lateral Geniculate Nucleus. *Journal of Neuroscience*, *33*(11), 4642–4656. <https://doi.org/10.1523/JNEUROSCI.5187-12.2013>
- Przybylski, A. W., Gaska, J. P., Foote, W., & Pollen, D. A. (2000). Striate cortex increases contrast gain of macaque LGN neurons. *Visual Neuroscience*, *17*(4), 485–494. <https://doi.org/10.1017/S0952523800174012>
- Pu, M., & Amthor, F. R. (1990). Dendritic morphologies of retinal ganglion cells projecting to the lateral geniculate nucleus in the rabbit. *Journal of Comparative Neurology*, *302*(3), 675–693. <https://doi.org/10.1002/cne.903020320>
- Puller, C., & Haverkamp, S. (2011). Bipolar cell pathways for color vision in non-primate dichromats. *Visual Neuroscience*, *28*(1), 51–60. <https://doi.org/10.1017/S0952523810000271>
- Purves, D., Augustine, G., & Fitzpatrick, D. (2001). Functional Specialization of the Rod and Cone Systems. In *Neuroscience* (p. na). Retrieved from <https://www.ncbi.nlm.nih.gov/books/NBK10850/>
- Quiroga, R. Q., Nadasdy, Z., & Ben-Shaul, Y. (2004). Unsupervised Spike Detection and Sorting with Wavelets and Superparamagnetic Clustering. *Neural Computation*, *16*(8), 1661–1687. <https://doi.org/10.1162/089976604774201631>
- Reese, B. E. (1988). “Hidden lamination” in the dorsal lateral geniculate nucleus: the functional organization of this thalamic region in the rat. *Brain Research Reviews*. [https://doi.org/10.1016/0165-0173\(88\)90017-3](https://doi.org/10.1016/0165-0173(88)90017-3)
- Reid, R. C., & Usrey, W. M. (2004). Functional connectivity in the pathway from retina to striate cortex. *The Visual Neurosciences*, *1*, 673–679.
- Riggs, L. A. (1967). *Electrical evidence on the trichromatic theory. The Jonas S. Friedenwald Memorial Lecture. Investigative ophthalmology* (Vol. 6). Retrieved from <http://www.ncbi.nlm.nih.gov/pubmed/6016387>
- Rivlin-Etzion, M., Zhou, K., Wei, W., Elstrott, J., Nguyen, P. L., Barres, B. A., ... Feller, M. B. (2011). Transgenic Mice Reveal Unexpected Diversity of On-Off Direction-Selective Retinal Ganglion Cell Subtypes and Brain Structures Involved in Motion Processing. *Journal of Neuroscience*, *31*(24), 8760–8769. <https://doi.org/10.1523/JNEUROSCI.0564-11.2011>
- Rodieck, R. W. (1967). Receptive fields in the cat retina: a new type. *Science*, *157*(3784), 90–92. <https://doi.org/10.1126/science.157.3784.90>
- Röhlich, P., van Veen, T., & Szél, Á. (1994). Two different visual pigments in one retinal cone cell. *Neuron*, *13*(5), 1159–1166. [https://doi.org/10.1016/0896-6273\(94\)90053-1](https://doi.org/10.1016/0896-6273(94)90053-1)
- Rompani, S. B., Wanner, A., Zhang, C., Roth, C. N., Yonehara, K., Wanner, A., ... Roska, B. (2017). Different Modes of Visual Integration in the Lateral Geniculate Nucleus Revealed by Single-Cell- Initiated Transsynaptic Tracing. *Neuron*, *93*(4), 767–776. <https://doi.org/10.1016/j.neuron.2017.01.028>

- Roska, B., & Werblin, F. (2001). Vertical interactions across ten parallel, stacked representations in the mammalian retina. *Nature*, *410*(6828), 583–587. <https://doi.org/10.1038/35069068>
- Rousso, D. L., Qiao, M., Kagan, R. D., Yamagata, M., Palmiter, R. D., & Sanes, J. R. (2016). Two Pairs of {ON} and {OFF} Retinal Ganglion Cells Are Defined by Intersectional Patterns of Transcription Factor Expression. *Cell Rep.*, *15*(9), 1930–1944.
- Saleem, A. B., Ayaz, A., Jeffery, K. J., Harris, K. D., & Carandini, M. (2013). Integration of visual motion and locomotion in mouse visual cortex. *Nature Neuroscience*, *16*(12), 1864–1869. <https://doi.org/10.1038/nn.3567>
- Salinas, S., Schiavo, G., & Kremer, E. J. (2010). A hitchhiker’s guide to the nervous system: The complex journey of viruses and toxins. *Nature Reviews Microbiology*. <https://doi.org/10.1038/nrmicro2395>
- Sanes, J. R., & Masland, R. H. (2015). The Types of Retinal Ganglion Cells: Current Status and Implications for Neuronal Classification. *Annual Review of Neuroscience*, *38*(1), 221–246. <https://doi.org/10.1146/annurev-neuro-071714-034120>
- Schmidt, T. M., Alam, N. M., Chen, S., Kofuji, P., Li, W., Prusky, G. T., & Hattar, S. (2014). A Role for Melanopsin in Alpha Retinal Ganglion Cells and Contrast Detection. *Neuron*, *82*(4), 781–788. <https://doi.org/10.1016/j.neuron.2014.03.022>
- Scholl, B., Latimer, K. W., & Priebe, N. J. (2012). A Retinal Source of Spatial Contrast Gain Control. *Journal of Neuroscience*, *32*(29), 9824–9830. <https://doi.org/10.1523/JNEUROSCI.0207-12.2012>
- Seabrook, T. a, Krahe, T. E., Govindaiah, G., & Guido, W. (2013). Interneurons in the mouse visual thalamus maintain a high degree of retinal convergence throughout postnatal development. *Neural Development*, *8*, 24. <https://doi.org/10.1186/1749-8104-8-24>
- Sherman, S. M. (1985). Functional organization of the W-,X-, and Y-cell pathways in the cat: a review and hypothesis. *Progr.Psychobiol.Physiol.Psychol.*, *11*, 233–314.
- Sillito, A. M., Cudeiro, J., & Jones, H. E. (2006). Always returning: feedback and sensory processing in visual cortex and thalamus. *Trends in Neurosciences*. <https://doi.org/10.1016/j.tins.2006.05.001>
- Sincich, L. C., Adams, D. L., Economides, J. R., & Horton, J. C. (2007). Transmission of Spike Trains at the Retinogeniculate Synapse. *Journal of Neuroscience*, *27*(10), 2683–2692. <https://doi.org/10.1523/JNEUROSCI.5077-06.2007>
- Sivyer, B., Taylor, W. R., & Vaney, D. I. (2010). Uniformity detector retinal ganglion cells fire complex spikes and receive only light-evoked inhibition. *Proceedings of the National Academy of Sciences*, *107*(12), 5628–5633. <https://doi.org/10.1073/pnas.0909621107>
- SK, C., C, T., SG, S., PR, M., Cheong, S. K., Tailby, C., ... Martin, P. R. (2013). Cortical-Like Receptive Fields in the Lateral Geniculate Nucleus of Marmoset Monkeys. *The Journal of Neuroscience: The Official Journal of the Society for Neuroscience*, *33*(16), 6864–6876. <https://doi.org/10.1523/JNEUROSCI.5208-12.2013>
- Stone, J. (1984). *Parallel Processing In the Visual System. The Quarterly Review of Biology* (Vol. 59). Boston, MA: Springer US. <https://doi.org/10.1086/414143>

- Strettoi, E., & Masland, R. H. (1996). The number of unidentified amacrine cells in the mammalian retina. *Proceedings of the National Academy of Sciences of the United States of America*, 93(25), 14906–11. Retrieved from <http://www.pubmedcentral.nih.gov/articlerender.fcgi?artid=26235&tool=pmcentrez&rendertype=abstract>
- Sümbül, U., Song, S., McCulloch, K., Becker, M., Lin, B., Sanes, J. R., ... Seung, H. S. (2014). A genetic and computational approach to structurally classify neuronal types. *Nature Communications*, 5. <https://doi.org/10.1038/ncomms4512>
- Sur, M., Esguerra, M., Garraghty, P. E., Kritzer, M. F., & Sherman, S. M. (1987). Morphology of physiologically identified retinogeniculate X- and Y-axons in the cat. *Journal of Neurophysiology*, 58(1), 1–32. Retrieved from <http://www.ncbi.nlm.nih.gov/pubmed/3612221>
- Szél, Röhlich, P., Gaffé, A. R., Juliusson, B., Aguirre, G., & Van Veen, T. (1992). Unique topographic separation of two spectral classes of cones in the mouse retina. *Journal of Comparative Neurology*, 325(3), 327–342. <https://doi.org/10.1002/cne.903250302>
- Theis, L., Berens, P., Froudarakis, E., Reimer, J., Román Rosón, M., Baden, T., ... Bethge, M. (2016). Benchmarking Spike Rate Inference in Population Calcium Imaging. *Neuron*, 90(3), 471–482. <https://doi.org/10.1016/j.neuron.2016.04.014>
- Tien, N.-W., Pearson, J. T., Heller, C. R., Demas, J., & Kerschensteiner, D. (2015). Genetically Identified Suppressed-by-Contrast Retinal Ganglion Cells Reliably Signal Self-Generated Visual Stimuli. *Journal of Neuroscience*, 35(30), 10815–10820. <https://doi.org/10.1523/JNEUROSCI.1521-15.2015>
- Troy, J. B., Einstein, G., Schuurmans, R. P., Robson, J. G., & Enroth-Cugell, C. (1989). Responses to sinusoidal gratings of two types of very nonlinear retinal ganglion cells of cat. *Visual Neuroscience*, 3(3), 213–23. <https://doi.org/10.1017/S0952523800009974>
- Usrey, W. M., Reppas, J. B., & Reid, R. C. (1999). Specificity and strength of retinogeniculate connections. *Journal of Neurophysiology*, 82(6), 3527–3540.
- Vaiceliunaite, A., Eriskien, S., Franzen, F., Katzner, S., & Busse, L. (2013). Spatial integration in mouse primary visual cortex. *Journal of Neurophysiology*, 110(4), 964–972. <https://doi.org/10.1152/jn.00138.2013>
- Van Wyk, M., Wässle, H., & Taylor, W. R. (2009). Receptive field properties of ON- and OFF-ganglion cells in the mouse retina. *Visual Neuroscience*, 26(3), 297–308. <https://doi.org/10.1017/S0952523809990137>
- Völgyi, B., Chheda, S., & Bloomfield, S. A. (2009). Tracer coupling patterns of the ganglion cell subtypes in the mouse retina. *Journal of Comparative Neurology*, 512(5), 664–687. <https://doi.org/10.1002/cne.21912>
- Ward Jr., J. H. (1963). Hierarchical grouping to optimize an objective function. *Journal of the American Statistical Association*, 58(301), 236–244.
- Wässle, H. (2004). Parallel Processing in the Mammalian Retina. *Nat. Rev. Neurosci.*, 5(October), 1–11. <https://doi.org/10.1038/nrn1497>
- Weyand, T. G. (2016). The multifunctional lateral geniculate nucleus. *Reviews in the Neurosciences*, 27(2), 135–157. <https://doi.org/10.1515/revneuro-2015-0018>

- White, a J., Solomon, S. G., & Martin, P. R. (2001). Spatial properties of koniocellular cells in the lateral geniculate nucleus of the marmoset *Callithrix jacchus*. *The Journal of Physiology*, 533(Pt 2), 519–535. https://doi.org/PHY_11799 [pii]
- Xin, D., & Bloomfield, S. A. (1999). Dark- and light-induced changes in coupling between horizontal cells in mammalian retina. *Journal of Comparative Neurology*, 405(1), 75–87. [https://doi.org/10.1002/\(SICI\)1096-9861\(19990301\)405:1<75::AID-CNE6>3.0.CO;2-D](https://doi.org/10.1002/(SICI)1096-9861(19990301)405:1<75::AID-CNE6>3.0.CO;2-D)
- Yatsenko, D., Reimer, J., Ecker, A. S., Walker, E. Y., Sinz, F., Berens, P., ... Tolias, A. S. (2015). DataJoint: managing big scientific data using MATLAB or Python. *bioRxiv*. <https://doi.org/10.1101/031658>
- Yonehara, K., Ishikane, H., Sakuta, H., Shintani, T., Nakamura-Yonehara, K., Kamiji, N. L., ... Noda, M. (2009). Identification of retinal ganglion cells and their projections involved in central transmission of information about upward and downward image motion. *PLoS ONE*, 4(1), e4320. <https://doi.org/10.1371/journal.pone.0004320>
- Yonehara, K., Shintani, T., Suzuki, R., Sakuta, H., Takeuchi, Y., Nakamura-Yonehara, K., & Noda, M. (2008). Expression of SPIG1 reveals development of a retinal ganglion cell subtype projecting to the medial terminal nucleus in the mouse. *PLoS ONE*, 3(2). <https://doi.org/10.1371/journal.pone.0001533>
- Zeater, N., Cheong, S. K., Solomon, S. G., Dreher, B., & Martin, P. R. (2015). Binocular Visual Responses in the Primate Lateral Geniculate Nucleus. *Current Biology*, 25(24), 3190–3195. <https://doi.org/10.1016/j.cub.2015.10.033>
- Zhang, J., Jung, C. S., & Slaughter, M. M. (1997). Serial inhibitory synapses in retina. *Visual Neuroscience*, 14(3), 553–563. <https://doi.org/10.1017/S0952523800012219>
- Zhang, Y., Kim, I.-J., Sanes, J. R., & Meister, M. (2012). The most numerous ganglion cell type of the mouse retina is a selective feature detector. *Proceedings of the National Academy of Sciences*, 109(36), E2391–E2398. <https://doi.org/10.1073/pnas.1211547109>
- Zhao, X., Chen, H., Liu, X., & Cang, J. (2013a). Orientation-selective Responses in the Mouse Lateral Geniculate Nucleus. *Journal of Neuroscience*, 33(31), 12751–12763. <https://doi.org/10.1523/JNEUROSCI.0095-13.2013>
- Zhao, X., Liu, M., & Cang, J. (2013b). Sublinear binocular integration preserves orientation selectivity in mouse visual cortex. *Nature Communications*, 4. <https://doi.org/10.1038/ncomms3088>
- Ziburkus, J., & Guido, W. (2006). Loss of binocular responses and reduced retinal convergence during the period of retinogeniculate axon segregation. *Journal of Neurophysiology*, 96(5), 2775–2784. <https://doi.org/10.1152/jn.01321.2004>

7 Acknowledgements

This work would not have been possible without the help and support from a large number of people. I would especially like to thank:

- My supervisors Prof. Dr. Thomas Euler and Prof. Dr. Laura Busse for their constant and strong support throughout my doctoral studies.
- PD. Dr. Philipp Berens for his close and excellent collaboration and for being a member of my thesis advisory committee.
- Dr. Ziad Hafed for joining my thesis advisory committee and for his helpful feedback.
- Dr. Tom Baden for his help with Igor Pro programming and his enthusiasm.
- Gordon Eske for his excellent technical support and his help with many problems.
- Yannik Bauer and all current and former lab members for their thoughtful discussions and insights.
- My family, my friends, and especially my wife Elena for being always by my side.

This research project/publication was supported by the DFG (EXC 307, CIN), the Bernstein Centre for Computational Neuroscience Tübingen (BMBF FKZ 01GQ1002), SFB 1233 TP 13 awarded to PB, LB, and TE, and by LMU Munich's Institutional Strategy LMUexcellent within the framework of the German Excellence Initiative.

8 Appendix

Appendix 1

The functional diversity of retinal ganglion cells in the mouse

Appendix 2

Subcortical source and modulation of the narrowband gamma oscillation in mouse visual cortex

Appendix 3

Benchmarking spike rate inference in population calcium imaging

Appendix 4

Community-based benchmarking improves spike inference from two-photon calcium imaging data

Appendix 5

Sparse linear recombination using most retinal output channels yields highly diverse visual representations in mouse dLGN

8.1.1 Appendix 1

The functional diversity of retinal ganglion cells in the mouse

Tom Baden*, Philipp Berens*, Katrin Franke*, Miroslav Román Rosón, Matthias Bethge and Thomas Euler (2016), Nature 529: 353-350, DOI <https://doi.org/10.1038/nature16468>

*equal contributions

Abstract

In the vertebrate visual system, all output of the retina is carried by retinal ganglion cells. Each type encodes distinct visual features in parallel for transmission to the brain. How many such “output channels” exist and what each encodes is an area of intense debate. In mouse, anatomical estimates range between 15-20 channels, and only a handful are functionally understood. Combining two-photon calcium imaging to obtain dense retinal recordings and unsupervised clustering of the resulting sample of >11,000 cells, we here show that the mouse retina harbours substantially more than 30 functional output channels. These include all known and several new ganglion cell types, as verified by genetic and anatomical criteria. Therefore, information channels from the mouse’s eye to the mouse’s brain are considerably more diverse than shown thus far by anatomical studies, suggesting an encoding strategy resembling that used in state-of-the-art artificial vision systems.

Contributions

TB, PB, MB and TE designed the study; KF performed imaging experiments with help by TB; KF and MRR performed electrophysiological experiments with help by TB; TB, PB, KF and MRR performed pre-processing; PB developed the clustering framework with help of MB; TB and PB analysed the data with input from TE; TB, PB and TE wrote the manuscript.

8.1.2 Appendix 2

Subcortical Source and Modulation of the Narrowband Gamma Oscillation in Mouse Visual Cortex

Aman B. Saleem, Anthony D. Lien, Michael Krumin, Bilal Haider, Miroslav Román Rosón, Asli Ayaz, Kimberly Reinhold, Laura Busse, Matteo Carandini and Kenneth D. Harris (2017), *Neuron* 93: 315-322, DOI <https://doi.org/10.1016/j.neuron.2016.12.028>

Abstract

Primary visual cortex exhibits two types of gamma rhythm: broadband activity in the 30–90 Hz range and a narrowband oscillation seen in mice at frequencies close to 60 Hz. We investigated the sources of the narrowband gamma oscillation, the factors modulating its strength, and its relationship to broadband gamma activity. Narrowband and broadband gamma power were uncorrelated. Increasing visual contrast had opposite effects on the two rhythms: it increased broadband activity, but suppressed the narrowband oscillation. The narrowband oscillation was strongest in layer 4 and was mediated primarily by excitatory currents entrained by the synchronous, rhythmic firing of neurons in the lateral geniculate nucleus (LGN). The power and peak frequency of the narrowband gamma oscillation increased with light intensity. Silencing the cortex optogenetically did not abolish the narrowband oscillation in either LGN firing or cortical excitatory currents, suggesting that this oscillation reflects unidirectional flow of signals from thalamus to cortex.

Contributions

Conceptualization, ABS., MK, MC, and KDH; Methodology, ABS, ADL, BH, MRR, AA, KR, and LB (specific experimental contributions are listed in Table S1); Formal Analysis, ABS; Writing - Original Draft, ABS, MC, and KDH; Writing - Review & Editing, all authors. MC and KDH are co-senior authors.

8.1.3 Appendix 3

Benchmarking Spike Rate Inference in Population Calcium Imaging

Lucas Theis*, Philipp Berens*, Emmanouil Froudarakis, Jacob Reimer, Miroslav Román Rosón, Tom Baden, Thomas Euler, Andreas S. Tolias and Matthias Bethge (2016). *Neuron* 90: 471–482, DOI <https://doi.org/10.1016/j.neuron.2016.04.014>

*equal contributions

Abstract

A fundamental challenge in calcium imaging has been to infer spike rates of neurons from the measured noisy fluorescence traces. We systematically evaluate different spike inference algorithms on a large benchmark dataset (>100,000 spikes) recorded from varying neural tissue (V1 and retina) using different calcium indicators (OGB-1 and GCaMP6). In addition, we introduce a new algorithm based on supervised learning in flexible probabilistic models and find that it performs better than other published techniques. Importantly, it outperforms other algorithms even when applied to entirely new datasets for which no simultaneously recorded data is available. Future data acquired in new experimental conditions can be used to further improve the spike prediction accuracy and generalization performance of the model. Finally, we show that comparing algorithms on artificial data is not informative about performance on real data, suggesting that benchmarking different methods with real-world datasets may greatly facilitate future algorithmic developments in neuroscience.

Contributions

PB, MB, and LT designed the project. LT analysed the data with input from PB; EF, JR, and AST acquired V1 data. MRR, TB, and TE acquired retinal data. PB wrote the paper with input from all authors. PB and MB supervised the project.

8.1.4 Appendix 4

Community-based benchmarking of spike inference from two-photon imaging data

Philipp Berens, Jeremy Freeman, Thomas Deneux, Nicolay Chenkov, Thomas McColgan, Artur Speiser, Jakob H. Macke, Srinivas C. Turaga, Patrick Mineault, Peter Rupprecht, Stephan Gerhard, Rainer W. Friedrich, Johannes Friedrich, Liam Paninski, Marius Pachitariu, Kenneth D. Harris, Ben Bolte, Timothy A. Machado, Dario Ringach, Jacob Reimer, Emmanouilis Froudarakis, Thomas Euler, Miroslav Román Rosón, Andreas S. Tolias, & Matthias Bethge.

Under revision at PLoS Biology, preprint available under DOI <https://doi.org/10.1101/177956>

Abstract

In recent years, two-photon calcium imaging has become a standard tool to probe the function of neural circuits and to study computations in neuronal populations. However, the acquired signal is only an indirect measurement of neural activity due to the comparatively slow dynamics of fluorescent calcium indicators. Different algorithms for estimating spike trains from noisy calcium measurements have been proposed in the past, but it is an open question how far performance can be improved. Here, we report the results of the *spikefinder* challenge, launched to catalyse the development of new spike inference algorithms through crowd-sourcing. We present ten of the submitted algorithms which show improved performance compared to previously evaluated methods. Interestingly, the top-performing algorithms are based on a wide range of principles from deep neural networks to generative models, yet provide highly correlated estimates of the neural activity. The competition shows that benchmark challenges can drive algorithmic developments in neuroscience.

Contributions

PB, AST and MB designed the challenge; JF provided web framework; PB and JF ran the challenge; TD, NC, TM, AS, JHM, ST, PM, PR, SG, RF, JF, LP, MP, KDH, TM, DR submitted algorithms; JR, EF, TE, MRR, AST provided data; PB analysed the results with input from MB; LT pre-processed data; PB wrote the paper with input from all authors.

8.1.5 Appendix 5

Sparse linear recombination using most retinal output channels yields highly diverse visual representations in mouse dLGN

Miroslav Román Rosón, Yannik Bauer, Philipp Berens #, Thomas Euler #, Laura Busse #
shared corresponding authors

This manuscript is in preparation; it covers most of the content of this thesis.

Abstract

In the mouse, the parallel output of more than 30 functional types of retinal ganglion cells (RGCs) serves as the basis for all further visual processing. Little is known about how the representation of visual information changes between the retina and the dorsolateral geniculate nucleus (dLGN) of the thalamus. Here, we functionally characterized responses of retrogradely labelled dLGN-projecting RGCs and dLGN neurons to a common set of visual stimuli, and used a linear model to assess functional connectivity between RGC types and dLGN neurons. We found that the majority of previously identified functional RGC types innervate the dLGN. Receiving such rich retinal input, the dLGN population response maintained a high degree of the functional diversity. Computational modelling revealed that the responses of dLGN neurons can be predicted as a linear combination of inputs from 1-7 RGC types. We conclude that a sparse recombination using most retinal output channels yields highly diverse visual representations in mouse dLGN.

Contributions

TE, LB and MRR designed the study; MRR and YB carried out imaging experiments with help by TE; MRR carried out electrophysiological experiments with help by LB; MRR performed pre-processing and analysed electrophysiological data with input from LB. YB analysed imaging data with input from PB; MRR established the model with input from YB, PB; MRR wrote the original manuscript; Review & Editing, all authors